Novel Approaches to the Bottom-up Fabrication of Ordered Organic Nanostructures on Metal Surfaces

---

Dissertation

zur

Erlangung der naturwissenschaftlichen Doktorwürde
(Dr. sc. nat.)

vorgelegt der

Mathematisch-naturwissenschaftlichen Fakultät

der

Universität Zürich

von

Matthias Treier

von

Wölflinswil AG

Promotionskomitee
Prof. Dr. Jürg Osterwalder (Vorsitz)
Prof. Dr. Thomas Greber
Prof. Dr. Neville V. Richardson
Prof. Dr. Roman Fasel (Leitung der Dissertation)

Zürich, 2009

Die vorliegende Arbeit wurde von der Mathematisch-naturwissenschaftlichen Fakultät der Universität Zürich auf Antrag von Prof. Dr. Jürg Osterwalder als Dissertation angenommen.

Abstract

The efficient production of ordered, tailored and functional nanostructures is the ultimate goal of nanotechnology. Production techniques that create nanostructures in a top-down fashion – i.e. by breaking a bulk starting material into smaller pieces until the spatial extent of the pieces falls within the nanoscale region – are limited with respect to the ultimate size that can be achieved. Techniques relying on self-assembly, where nanostructures are created from individual building blocks as small as single atoms or molecules in a bottom up way are therefore promising concepts for future technological applications.

In this thesis, five novel approaches that allow to steer the self-assembly of molecular adsorbates on single crystal metal surfaces are presented. To this end, the adsorption behaviour of large organic adsorbates on single crystal coin metal surfaces has been studied by scanning tunneling microscopy (STM) and X-ray photoelectron diffraction (XPD) and complemented by theoretical calculations.

A first approach to steer the self-assembly of adsorbates is demonstrated at the example of the site-selective adsorption of the nanographene molecule hexa-*peri*-hexabenzocoronene on the naturally templated Au(11 12 12) crystal. The molecule is found to selectively adsorb across kinks at low coverage with an unusual tilted adsorption geometry determined by a combined STM and XPD study.

The use of aromatic interactions as design units in 2D-supramolecular architectures is shown for the first time by analyzing the self-assembly of the nonplanar polycyclic aromatic hydrocarbon hexa-*cata*-hexabenzocoronene on Cu(111). Supramolecular structures are found to be stabilized by lateral aromatic interactions due to interdigitating helical units. The possible usefulness – due to partial overlap of π-orbitals – of such structures in molecular electronics applications is outlined.

The application of two-dimensional supramolecular architectures as templates is hampered by their limited thermal and chemical stability. To overcome this limitation, the formation of covalently bound polymeric supramolecular structures has been investigated at the example of a surface-confined imidization reaction between di- and tri-amines and the prototypical organic semiconductor PTCDA on Au(111). Imidization is shown to proceed also if the reactants are confined to two dimensions but the amic acid reaction intermediate is shown to be formed only at temperatures higher than in the corresponding reaction in thin films and solution.

When deposited at room temperature, amine- and anhydride-functionalized molecules form a rich variety of supramolecular structures which are governed by the subtle energy balance between hetero- and homomolecular hydrogen bonds. It is shown that this behaviour can be rationalized and that such a subtle energy balance can be exploited for the creation of ordered nano-units of PTCDA such as an array of potential quantum dots.

The inter- and intramolecular ordering of the trimetallic nitride endofullerene $Dy_3N@C_{80}$ is probed by a combined STM and XPD study. The results are complemented by resonant XPD which is shown to be useful for systems where no clearly distinguishable diffraction patterns can be measured by standard XPD due to limited statistics resulting from low peak-to-background ratios. As for the study of the adsorption behaviour of HBC on vicinal gold, the complementarity of STM and XPD is illustrated for this adsorbate system.

Zusammenfassung

Die effiziente Produktion von geordneten, massgeschneiderten und funktionellen Nanostrukturen ist eines der Hauptziele der Nanotechnologie. Produktionsmethoden, bei denen Nanostrukturen in einem „*top-down*“ Ansatz hergestellt werden, d.h. indem ein Ausgangsmaterial in immer kleinere Teile zerlegt wird bis die räumliche Ausdehnung im Bereich des Nanometers liegt, sind in ihrer Auflösung begrenzt. Der gegensätzliche „*bottom-up*“ Ansatz, bei dem sich einzelne Komponenten von der Grösse einzelner Atome oder Moleküle durch Selbstorganisation spontan zu Nanostrukturen anordnen eröffnet hingegen erfolgsversprechende Möglichkeiten für die Herstellung von nanostrukturierten Bauteilen für zukünftige technologische Anwendungen.

In dieser Dissertation werden fünf neue Arten der kontrollierten Selbstorganisation von molekularen Adsorbaten auf einkristallinen Metalloberflächen präsentiert. Diese werden anhand von Adsorptionssystemen grosser organischer Adsorbate auf metallischen Einkristallen demonstriert. Hierzu werden die experimentellen Methoden der Rastertunnelmikroskopie (STM) und Photoelektronenbeugung (XPD) mit theoretischen Simulationen kombiniert.

Am Beispiel des Nanographen-Moleküls Hexa-*peri*-hexabenzocoronen auf der intrinsisch strukturierten Oberfläche eines Au(11 12 12) Kristalls wird gezeigt dass die Selbstorganisation über die selektive Adsorption an spezifischen Orten auf einem Templat beeinflusst werden kann. Aus einer kombinierten STM- und XPD-Studie folgt dass das Nanographen-Molekül bei geringer Bedeckung selektiv über Stufenkanten und Kinken adsorbiert.

Die Anwendung aromatischer Wechselwirkungen zur Bildung zweidimensionaler supramolekularer Netzwerke wird am Beispiel der Selbstorganisation des nicht-planaren polyzyklischen Aromaten Hexa-*cata*-hexabenzocoronen auf Cu(111) demonstriert. Supramolekulare Bienenwabenstrukturen werden durch laterale aromatische Wechselwirkungen zwischen ineinander verschränkten spiralförmigen aromatischen Einheiten stabilisiert. Die Auswirkungen der überlappenden π-Orbitale auf die Ladungstransfereigenschaften werden diskutiert.

Um als Template in technologischen Anwendungen benutzt werden zu können, müssen supramolekulare Netzwerke eine hohe thermische und chemische Stabilität aufweisen, was bei auf nicht-kovalenten Bindungen (z.B. Wasserstoffbrücken) basierenden Netzwerken im Allgemeinen nicht der Fall ist. Um die Stabilität supramolekularer Netzwerke zu erhöhen, sollten diese also kovalent gebunden sein. Die Möglichkeiten zur Herstellung solcher Netzwerke durch Imidisierung auf einer Au(111) Oberfläche werden am Beispiel der Oberflächen-unterstützten Kondensierung des organischen Halbleiters PTCDA und Di- und Triaminen erläutert. Es wird gezeigt, dass die Imidisierungs-Kondensierung auch in zwei Dimensionen thermisch induziert werden kann.

Aufbringen von Amino- und Anhydrid-funktionalisierten Molekülen auf Au(111) führt zur Ausbildung einer Reihe von supramolekularen Strukturen, die auf dem Zusammenspiel von hetero- und homomolekularen Wasserstoffbrücken beruhen. Es wird gezeigt, dass diese Art der Selbstanordnung – basierend auf der leichten energetischen Favorisierung einer der beiden Wechselwirkungen –zur Ausbildung geordneter supramolekularer Strukturen genutzt werden kann, so auch eines potentiellen Gitters von Quantenpunkten.

Die inter- und intramolekulare Ordnung des endhohedralen Fullerens $Dy_3N@C_{80}$ auf Cu(111) wurde mit STM und XPD untersucht. Zusätzliche resonante XPD Messungen geben Aufschluss über die Ordnung der endohedralen Dysprosium-Atome. Die Komplementarität der beiden Methoden STM und XPD wird, wie schon für die Analyse des Adsorptionsverhalten von HBC auf vizinalem Gold, exemplarisch aufgezeigt.

Contents

List of abbreviations

Experimental techniques and related abbreviations

UHV	Ultra high vacuum
STM	Scanning tunneling microscopy / microscope
XPS	X-ray photoelectron spectroscopy
XPD	X-ray photoelectron diffraction
rXPD	Resonant X-ray photoelectron diffraction
LEED	Low energy electron diffraction
MBE	Molecular beam epitaxy

Theoretical methods

SSC	Single scattering cluster simulations
MSC	Multiple scattering cluster simulations
AM1	Austin model 1
CHARMM	Chemistry at HARvard Macromolecular Mechanics (Force-field)
DFT	Density functional theory

Organic substances

HBC	Hexa-*peri*-hexabenzocoronene
cHBC	contorted HBC; hexa-*cata*-hexabenzocoronene
pHBC	permethoxylated HBC; 1,2,3,4,5,6,7,8,9,10,11,12,13,14,15,16,17,18-Octadecamethoxy-hexa-*peri*-hexabenzocoronene
ddmHBC	Dodecamethyl HBC; 1,3,4,6,7,9,10,12,13,15,16,18-*dodecamethyl*-hexa-peri-hexabenzocoronene
HBTP	Hexabenzotriphenylene
CHP	Cyclohexaphenylene
tnHBC	Benzo[o]bistriphenyleno[2,1,12,11-efghi:2’,1’,12’,11’-uvabc]ovalene
TPBPB	1,3,5-tris(2’-(4’’-phenyl)biphenyl)benzene
OBC	Octobenzocircumbiphenylene
DATP	4,4’-diamino-p-terphenyl
PTCDA	3,4,9,10-perylenetetracarboxylic-dianhydride
TAPT	2,4,6-tris(4-aminophenyl)-1,3,5-triazine
PI	Polyimide

Various

LUMO	Lowest unoccupied molecular orbital
HOMO	Highest occupied molecular orbital
PAH	Polycyclic aromatic hydrocarbon
fcc	face-centred cubic
hcp	hexagonal close packing
LDOS	Local density of states
R-factor	Reliability factor
RT	Room temperature
ML	Monolayer

List of substances

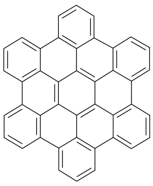

HBC

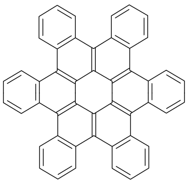

cHBC

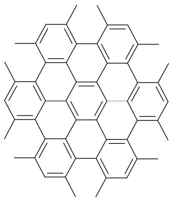

ddmHBC

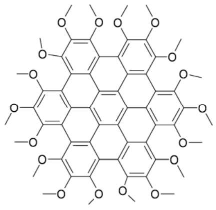

pHBC

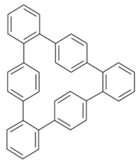

CHP

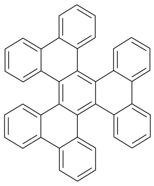

HBTP

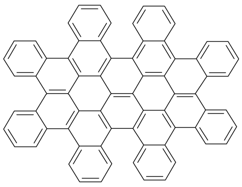

OBC

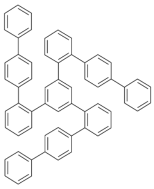

TPBPB

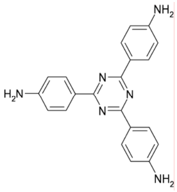

TAPT

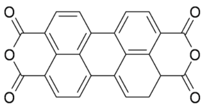

PTCDA

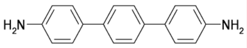

DATP

1 Introduction

Interest in nanoscale science arises from the general observation that physical properties of a material depend on its spatial dimensions and shape when one is going from macroscale to nanoscale dimensions (Figure 1a). In the transition region between bulk matter (>10^6 atoms) and single atoms, small changes in the number of constituents respectively their geometrical arrangement can give rise to pronounced changes in properties such as melting point [*1*, *2*], adsorption spectra [*3*] or magnetic moments [*4*] – to name but very few examples – which can differ markedly from those of the corresponding bulk matter. While the *nano* prefix seems to be inherently linked to the present decade, the use of nanoscale effects dates back much further. Among the most famous examples of an early 'nanotechnological' application is certainly the use of colloidal particles for glass staining in church windows (Figure 1b). Long before the discovery of atoms and the development of quantum mechanics, the effect that properties of materials depend on their spatial extent had already been exploited. However, only the advent of quantum mechanics has led to a quantitative understanding of why physical properties depend strongly on the number of atoms and their spatial arrangement if at least one of the dimensions is within the nanoscale (<100 nm). Nanoscience hence is not just a miniaturization from microscale to nanoscale motivated by a denser packing of individual units but represents an independent area of science.

The ultimate goal of nanoscale technology is to acquire the knowledge necessary to easily and reliably create and tune properties of a vast range of nanostructures, which would go along with an unproceeded leap in advancing technology. At the present stage, one is however far from such an universal understanding of nanoscale properties, and research efforts are focussed on understanding – and to a certain extent tuning – the properties of well-defined model systems rather than deriving generalized concepts.

Figure 1: (a) Melting temperature of gold clusters as a function of their radius. The graph is taken from reference [*1*]. (b) Element of the rose window (created around 1250) of the cathedral of Lausanne Switzerland, showing the use of stained glass in ancient times. (c) Bendable OLED display developed by Samsung, exemplifying the potential of organic electronics devices.

There are two fundamentally different approaches towards the creation of nanostructures. The family of so-called *top-down* techniques encompasses all techniques where nanostructures are created by reducing the dimensions of a starting bulk material, which is mostly achieved by lithography-based techniques, until the final products spatial extent lies within nanoscale dimensions. These techniques are hence simply an extension of well-known techniques used for the fabrication of microstructures. The problem of such top-down approaches is that they generally are intrinsically limited in resolution. While this limit has not yet been reached for all such techniques, it will at some stage set a lower size limit that can be achieved. On the other hand, in *bottom-up* approaches – which had first been suggested by Richard Feynman in his famous lecture at CalTech in 1959 [*5*] – structures are 'built', starting from single atoms or molecules, by adding – at least in principle – single building units in a step-by-step fashion until the wanted size and structure is reached. Commercial electronic products exploiting 'nanosccale effects' are – at the present stage – mainly created by top-down approaches. Bottom-up created nanoparticles have however found commercial applications in other market areas such as pharmaceutical products, functional textiles or surface coatings. To further reduce the size of individual components, production processes involving bottom-up processes will however need to be implemented in the production of nanostructures in the future. Among the most prominent driving forces behind the quest for miniaturization is the increasing demand for faster, cheaper and smaller electronic devices. To meet the last requirement – at the present stage – the *45 nm process* is used for the production of integrated devices on silicon chips. While, according to the international semiconductor road map [*6*], it might be possible to further refine the lithographic process down to 11 nm, an intrinsic limitation is set for this top-down approach. Alternative routes involving bottom-up production might allow reaching even smaller lengthscales in miniaturization. However, a parallel production of nanostructures in a true bottom-up fashion, i.e. by assembling the structures by moving individual atoms/molecules through external stimuli step-by-step, would be extremely slow and consequently expensive and inefficient. To circumvent this problem, future bottom-up fabrication processes are expected to rely on the self-assembly [*7, 8*], i.e. the autonomous organization of tailored components into designed patterns and structures without the need for human intervention. Self-assembly processes are ubiquitous in biological systems, for example in the folding of proteins or formation of lipid bilayer membranes [*8*]. Identifying and gaining the knowledge to be able to tune self-assembly processes which produce functional nanostructures is hence a key challenge of nanotechnology. The ultimate benchmark is nature which essentially derives its richness from self-assembly processes, which have been refined during evolution.

To be able to influence the self-assembly of individual building-blocks into larger structures one can tune the properties of these building blocks. While this may not be possible for individual atoms, the properties of larger building blocks such as molecules can be tuned more directly by chemical functionalization. This versatility of molecular building blocks, combined with their promising use in organic electronics devices and their comparably low cost [*9*] has motivated research on the self-assembly of organic semiconductors on surfaces. Although applications based on organic thin films have already matured into commercially available products [*9*] (Figure 1c)[1], the use of organic nanostructures or even single molecules [*10-12*] in electronic devices remains a challenge for the future. As an intermediate step, systems based on supramolecular aggregates might make their way into commercial electronics products. This area of research has been referred to as supramolecular electronics [*13*]. Probably the most successful application in the field of organic electronics are organic light emitting devices [*14*], followed by low cost organic thin film transistors [*15*], solar cells and photosensors [*16*]. Molecular nanostructures in two dimensions have been created using organic molecular beam deposition [*17*], self-assembled monolayers [*18*], langmuir(-blodgett) films, drop casting, spin coating, zone casting [*19*], electrochemical deposition, ink-jet printing [*20*], stamping [*21*] or various lithographic techniques. Each of these techniques is however limited with respect to the minimum lateral resolution that can be achieved. Therefore, the use of self-assembly processes represents a promising way towards the potential use of single molecules or small molecular clusters in future devices.

At present, intense research efforts are focussed on understanding and tuning the self-assembly of (sub-)monolayer thick organic films on simple single crystal surfaces [*22*] with many studies employing high resolution techniques such as scanning tunnelling microscopy [*23*] or atomic force microscopy [*24*]. While earlier studies focussed purely on the description of self-assembled mono- and multimolecular phases, the field has matured in the sense that rationally designed structures are achieved nowadays [*25*]. In these studies, self-assembly has been steered using non-covalent interactions like hydrogen bonds [*26, 27*] and metal-coordination [*28, 29*], hence transferring the knowledge from supramolecular chemistry [*30*] and crystal engineering [*31*] in three dimensions to two-dimensional structures. The interaction of adsorbates with the substrate and the reduced conformational/orientational degrees of freedom in two-dimensions are responsible for differences between these two fields of supramolecular chemistry, preventing a one-to-one application of all building concepts from three to two dimensions, making the field of two-dimensional supramolecular architectures an independent area of research. Two examples of two-dimensional supramolecular architectures are given in Figure 2.

---

[1] An extensive overview on the recent state of organic electronics can be found in the focus issue on “Organic Electronics and Optoelectronics” of *Chemical Reviews* (Volume 107, Issue 4, 2007)

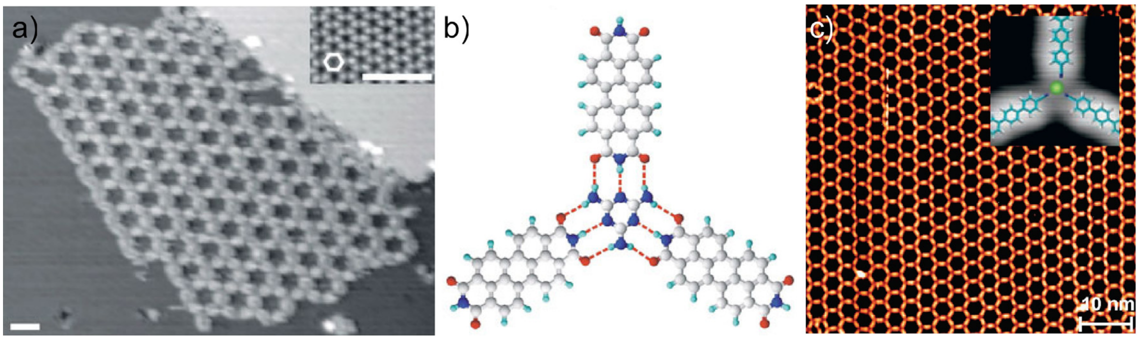

Figure 2: Examples of supramolecular architectures in two dimensions. (a) Bi-molecular network stabilized by triple hydrogen bonds as shown in (b). (c) Honeycomb network based on metal coordination between Co-atoms and carbonitrile groups (see inset). Figures (a)&(b) are taken from reference [*26*], Figure (c) and its inset have been taken from references [*22, 28*].

Surface-supported organic nanostructures of well-defined size and shape can alternatively also be created by moving individual atoms/molecules with an STM/AFM tip [*32-34*]. While this is an adequate approach for the study of size-dependant effects of organic nanostructures, the extremely low throughput and intrinsically complicated nature of these techniques prevent their use in large-scale bottom-up production systems, even if arrays of parallel tips were used [*35*].

STM also allows to study dynamics [*36*, *37*], chirality [*38*, *39*], electronic and magnetic properties, vibrational spectra [*40*], adsorbate-induced substrate reconstructions [*41*], conformational switching [*42*, *43*], adsorption on semiconductors [*44*, *45*] and thin insulating films [*46*, *47*] of molecules on surfaces. Such issues are however not addressed in this thesis which focuses on the preparation and subsequent characterization – using STM and X-ray photoelectron diffraction – of ordered organic structures on metal surfaces by influencing the self-assembly of adsorbates in different manners.

In this thesis, only surface-supported organic nanostructures are considered, which is motivated by their potential use in future electronic devices. However, it is the clear goal of the author that the bottom-up approaches outlined in this thesis should be regarded as general concepts – demonstrated in the particular case of surface-supported self-assembly – rather than being only applicable to two-dimensional systems.

This thesis is organized as follows: Chapter 2 contains a short summary of the experimental and theoretical methods used for this work. The following Chapters 3 to 7 each contain a brief introduction to an original manuscript, which has already been published/submitted[2], followed by an outlook on future work related to the topic of that manuscript. Each of these chapters presents a novel approach for the bottom-up creation of ordered organic nanostructures in two-dimensions. The selective anchoring of a large organic adsorbate on a templated substrate is shown in Chapter 3. The use of aromatic interactions for supramolecular organization in two-dimensions is shown in Chapter 4. A refined approach for self-assembly in 2D is given in Chapter 5, where the creation by self-assembly of a range of supramolecular structures is demonstrated for a particular combination of functional units of two co-adsorbates. In Chapter 6, the application of synthetic routes known from polymer science towards the creation of covalent surface-supported organic structures is shown at the example of polyimides. A different type of ordering on the nanoscale is demonstrated in Chapter 7. An adsorbed endohedral fullerene is shown to posses an ordered endohedral structure. A general outlook, linking the individual production concepts and conclusions for all projects presented in Chapters 3-7 is given in Chapter 8.

---

[2] It should be noted that the manuscript presented in Chapter 7 has not been submitted at the moment of handing in this thesis but is expected to be ready for submission (with minor modifications with respect to the version shown in Chapter 7) soon.

2 Experimental and theoretical methods

All experiments presented in this work have been performed in ultra high vacuum (UHV) systems with typical base pressures below $2 \cdot 10^{-10}$ mbar. Scanning tunneling microscopy (STM) and X-ray photoelectron diffraction (XPD) have been used as the principal methods of investigation. The basic principles underlying both methods are shortly described in this chapter. Another technique relevant to this work is low energy electron diffraction (LEED) which has been used to a lesser extent and for routine analysis only. An extensive description of this technique can be found elsewhere [*48*].

2.1 Scanning tunneling microscopy

The tunneling process is one of the most widely known direct consequences of quantum mechanics. While phenomena involving quantum size effects had already been used without knowing their origin before the development of quantum mechanics itself, the theoretical understanding of quantum size effects was necessary in order to be able to fully exploit these properties. When suggesting “to make the electron microscope 100 times better“ in his famous speech in 1959 [*5*], Feynman had foreseen that a more thorough understanding of quantum effects would eventually lead to microscopes capable of resolving individual atoms. While this had already been achieved by electron microscopes in the 1960s, it took until 1982 for Binning and Rohrer [*23*] to demonstrate the realizability of an instrument – the STM – capable of resolving individual atoms based on the quantum tunneling effect, opening the way for a new branch of surface science studies.

2.2 Principles of STM

The general set-up of an STM is shown in Figure 3a. An atomically sharp metallic tip sitting on a piezoelectric element is scanned over a conducting substrate with a potential difference applied between the two elements. At tip-sample separations on the order of a few to a few tens of Angstroms, a tunnelling current flowing between the tip and the sample can be detected. This current is monitored during scanning and converted into a real space image of the topography of the substrate. The most widely used operation mode is the so-called ‘constant-current’ mode in which an external feedback adjusts the tip-sample distance during measurement to keep the tunnelling current fixed to a set value.

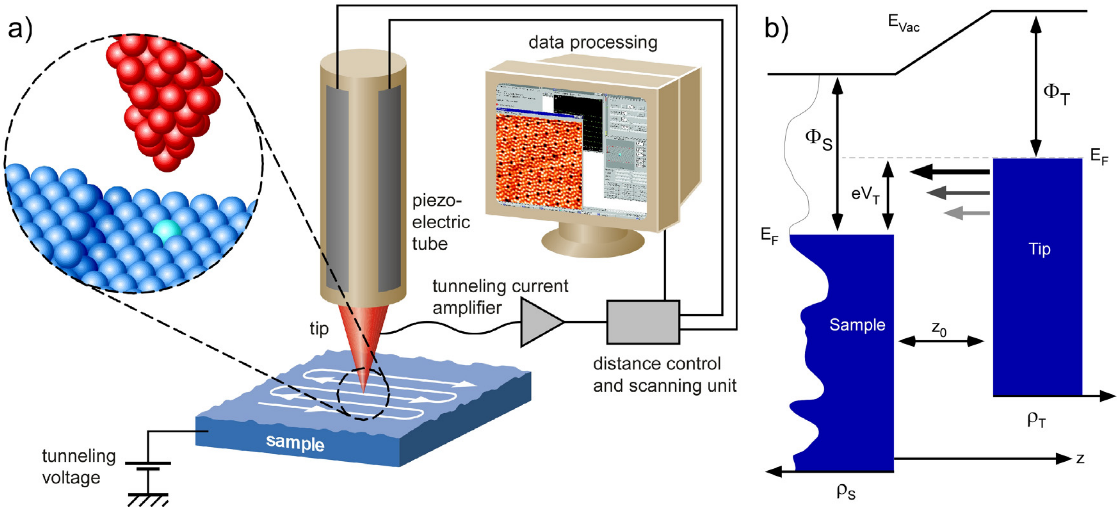

Figure 3: (a) Schematic set-up of an STM. By applying voltages to the piezo-tube the tip can be scanned across the sample. The tunneling current is used as a feedback signal to control the tip-sample distance. (b) Schematic energy diagram for a tunneling junction between a metallic sample and a perfect tip (ρ_T=const.).

The STM has been widely used to study surface phenomena and properties of metals, alloys, semiconductors, thin oxide, insulator and molecular films over the past 25 years. It has been used at pressures ranging from UHV to above standard pressure and also in electrochemical environments [*49*] and solution. In this work, however, only STM studies performed under UHV conditions are presented. Several recent reviews on the current state of the art of STM within various fields of surface science can be found in the literature [*36, 37, 50-54*].

The tunnelling effect describes the probability for the – classically forbidden – penetration through a potential barrier of height V by a particle of kinetic energy E. A typical textbook example of such a problem is the calculation of the transmission probability of an electron through a rectangular potential barrier in one dimension. Even though being a crude approximation to the situation in an STM tunnelling junction, the resulting transmission coefficient T represents a good approximation to the qualitative interpretation of STM images.

$$T \propto e^{\kappa z} \text{ where } \kappa = \sqrt{2m(V-E)}\,\hbar^{-1} \qquad (1)$$

This implies that increasing the barrier thickness z (or by analogy the tip-sample distance) by about 1 Å results in a decrease of the tunnelling current by approximately one order of magnitude. The tunnelling current in an STM is hence concentrated to a few atoms at the apex of the tip allowing for an imaging of the sample with very high lateral resolution (<1 Å). In the z direction, picometer resolutions can be achieved.

In reality there is however not only a single electronic state contributing to the total tunnelling current but the signal is a function of the electronic structure of both the tip and the sample within an energy interval given by the applied sample bias. The relevant parameters are given in Figure 3b. Based on Fermi’s golden rule, the tunnelling current between the tip states μ and the sample states υ is given by

$$I = \frac{2\pi e}{\hbar}\sum_{\mu\nu} f(E_\mu)[1-f(E_\nu+eV)] \times \left|M_{\mu\nu}\right|^2 \delta(E_\mu - E_\nu) \qquad (2)$$

where $M_{\mu\upsilon}$ is the tunnelling matrix element between the states υ and μ and $f(E)$ is the Fermi distribution which accounts for the temperature of the system. Bardeen [*55*] has shown that the matrix element can be computed by integrating the current density j over any surface lying entirely in the gap region:

$$M_{\mu\nu} = \int j_{\mu\nu}\cdot dS = -\frac{\hbar^2}{2m}\int_S d\vec{S}(\Psi_\mu^*\vec{\nabla}\Psi_\nu - \Psi_\mu\vec{\nabla}\Psi_\nu^*) \qquad (3)$$

While equation (3) is mathematically correct for any tunnelling geometry, it is not very useful since it involves knowledge of the exact wavefunctions of both the tip and the sample, so it is desirable to simplify it based on some adequate approximations. The most widely used model is the one proposed by Tersoff and Hamann [*56, 57*], where it is assumed that only s-wave tip-states are present in the spherical tip of radius R. Furthermore, the applied bias is assumed to be small compared to the work function of tip and sample, which are supposed to be equal. Equation (2) then simplifies to:

$$I \propto V\sum_\nu \left|\Psi_\nu(r_t)\right|^2 \delta(E_\nu - E_F) = V\rho_S(r_t, E_F) \text{ where } \quad r_t = R + z \qquad (4)$$

While the Tersoff-Hamann model is only strictly valid within the mentioned approximations, it shows that constant-current images can be interpreted as contours of constant LDOS at the Fermi level of the substrate. For simple systems (e.g. clean metal surfaces) these LDOS-contours can be readily interpreted as topographic maps, whereas this simplified interpretation is not applicable for systems where the local work function is not constant over the scanned area. It should also be noted that the approximation of small applied biases is not correct for most results presented in this work in which case the more general expression of the tunnelling current should be used:

$$I(V) \propto \int_0^{eV} \rho_t(E-eV)\rho_s(E)T(z,E,eV)dE \qquad (5)$$

where the transmission coefficient T is computed for a trapezoidal barrier

$$T(z,E,eV) = e^{-2(z+R)\kappa} \text{ with } \kappa^2 = \frac{2m\Phi_{eff}}{\hbar^2} \text{ where } \Phi_{eff} = \frac{1}{2}(\Phi_s + \Phi_t + eV) - E$$

For simplicity, the density of states of the tip ρ_t is often assumed to be constant over the energy interval probed at a bias *V*, such that equation (4) will only depend on the density of states of the sample ρ_S, allowing for a more direct interpretation of STM-images. More detailed descriptions of the theory of STM can be found in the literature [*58*, *59*].

2.3 Imaging Adsorbates with the STM

As outlined in the previous section, within the Tersoff-Hamann approach, STM maps contours of the local density of states at the Fermi level allowing for a straightforward interpretation of corrugations in images obtained on metallic surfaces. However, in the last decade the STM has also been successfully applied to systems which have a gap at the Fermi level, e.g. thin films of insulators such as organic molecules, metal oxides or ionic crystals grown on conducting substrates. While studies of film thicknesses of up to 100 nm have been reported, only the case of monolayer thick organic films is considered here.

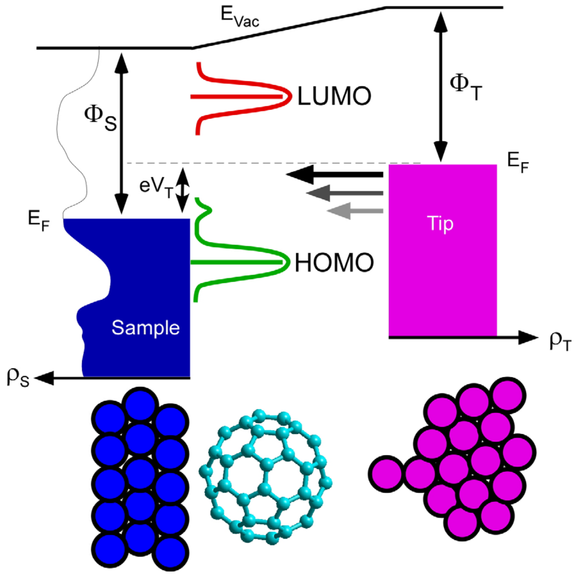

Figure 4: Schematic energy level diagram with energy levels relevant for STM-imaging of an organic adsorbate. The HOMO and LUMO levels are broadened compared to the gas phase due to the interaction with the substrate. The HOMO (which is in this example assumed to be lying closer to the Fermi level) extends up to E_F with a small induced density of states near E_F determining the appearance of the adsorbate in STM images. At the particular bias shown, the LUMO does not contribute to the tunnelling current.

For single atomic adsorbates it has been shown that the induced change of the local density of states near the Fermi level gives rise to the contrast in STM maps [*60*]. Depending on the substrate and adsorbate electronic structure, an adsorbate may hence be imaged either as a protrusion or a depression [*60*], showing that the simplistic picture of interpreting STM images as purely topographic images can fail completely when imaging adsorbed molecules.

In the hypothetical case where the electronic structure of the substrate remains unchanged by the presence of an adsorbed organic molecule, it would only be possible to image the latter at applied bias voltages exceeding the LUMO (positive sample bias) or HOMO (negative sample bias) energy since no states localized on the adsorbate would contribute to the tunnelling current in the intermediate energy interval. In reality, also physisorbed species will influence the LDOS of the substrate such that they can be imaged due to the modified density of states also when a bias between the HOMO and LUMO is applied. Furthermore, molecular orbitals are broadened upon adsorption due to the interaction with the underlying metal states, especially the d-band [*61*, *62*]. This broadening results in extended tails of these resonances, which can even contribute to the LDOS at the Fermi level (Figure 4). It has also been shown that the molecular orbital lying closer to the Fermi level will normally dominate the appearance of the adsorbate [*63*]. In general and especially for large organic adsorbates, several molecular orbitals will contribute to the appearance [*64*] of the latter and the way in which the molecule is imaged will depend on the applied bias (see e.g. PTCDA in Chapter 5).

While the above interpretation of STM images is true for all types of adsorbates, for larger adsorbates having a pronounced three-dimensional shape, images can be interpreted in a more straightforward way by directly relating protrusions with bulky units of the molecule that are pointing away from the latter (see e.g. contorted HBC in Chapter 4). This has been shown before theoretically by using elastic scattering quantum chemistry (ESQC) calculations, which have reproduced STM images of large adsorbates such as the 'Lander' molecule [*65*, *66*], spirobifluorene [*67*] or hexaphenylbenzene [*68*] by computing the full scattering matrix of the system, including the tip, adsorbate and substrate.

2.4 Photoelectron spectroscopy

Photoelectron spectroscopy is widely used for the determination of the valence electronic structure and chemical composition of thin films and surfaces. It is based on the detection of electrons emitted into the vacuum by the photoelectric effect, which had first been observed by Hertz [*69*] and later explained by Einstein [*70*]. A monoenergetic photon beam is directed towards a sample and the emitted photoelectrons are run through an electron energy analyser, which allows for a determination of the kinetic energy distribution of the photoelectrons. Using the well-known relationship between the kinetic energy E_{kin}, the analyser work function φ and photon energy $h\upsilon$

$$E_B = h\nu - E_{Kin} - \varphi \tag{6}$$

the binding energy E_B of a measured photoelectron line can be obtained.

Depending on whether the energy of the incident photons falls within the ultraviolet region (~5-50 eV) or the soft X-ray range (~200-2000 eV), the technique is referred to as ultraviolet or X-Ray photoelectron spectroscopy with acronyms UPS and XPS respectively. While UPS probes the valence electronic structure, XPS is used to study core levels, yielding information on the chemical composition of a sample. Additionally, so-called chemical shifts, i.e. variations in binding energy of core-levels, yield information on the coordination and chemical state of a given emitter. The inherent surface sensitivity of the technique stems from the short inelastic mean free path of the photoelectrons inside the solid within the energy range of interest, which is on the order of 5-20 Å [*71*].

2.5 Photoelectron diffraction

The possibility that electrons might be diffracted by atoms is a direct consequence of the wave-particle duality proposed by deBroglie in 1924 [*72*]. Experimental verifications of electron diffraction have been published by Davisson [*73*] as well as Thomson [*74*] independently only a few years after deBroglie's ground-breaking proposal. Over a few decades, the effect has been studied in more detail and finally matured into applications in nowadays standard surface science tools such as electron microscopy and low energy electron diffraction. In these techniques, an external beam of electrons is scattered by the electric potential produced by a periodic array of atoms in the sample. In photoelectron diffraction on the other hand, the scattered photoelectron emanates from the sample itself and is scattered by the electronic potential of neighbouring atoms before leaving the sample towards the vacuum.

The principle of XPD from an adsorbate is schematically sketched in Figure 5a. A spherical photoelectron wave from an emitter atom is elastically scattered by the neighbouring atoms and the unscattered wave interferes with the scattered waves resulting in a modulation of the photoelectron current as a function of emission direction. This modulation is measured by scanning the sample orientation with respect to the analyzer, hence sampling different emission angles. The shape of the scattered wave depends on the kinetic energy of the photoelectron, the atomic type and electronic configuration of the scatterer and the scattering angle. At high kinetic energies (>500 eV), the so-called 'forward-focussing' effect is dominant [*75*, *76*]. In this energy range, the scattering amplitude exhibits a sharp and pronounced peak along the nearest-neighbour directions (Figure 5b). For simple systems (e.g. single crystal metal surfaces) this effect then allows for a direct assignment of peaks in the diffraction pattern with nearest neighbour directions in the sample. For large organic adsorbates, where there are many inequivalent emitter-scatterer orientations, the interpretation of XPD patterns is less direct and involves a more complete theoretical modelling (see Chapter 2.6). It should be noted that in general, the outgoing wave is not only scattered at one atom but is sequentially scattered from several atoms.

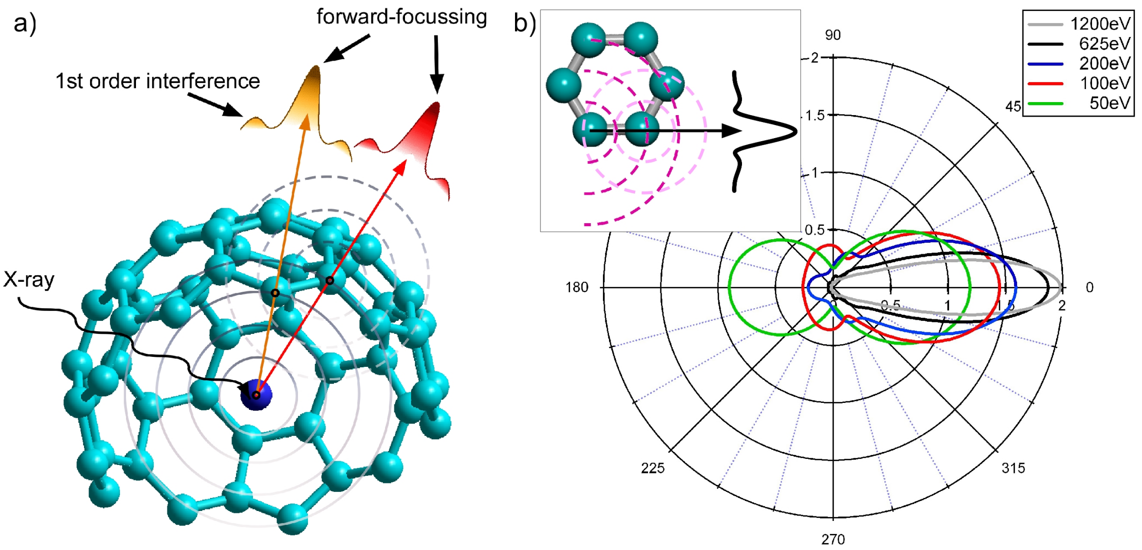

Figure 5: (a) Principle of XPD of an adsorbate, illustrated at the example of an endohedral fullerene. The photoelectron source wave emanating from the endohedral nitrogen atom (blue) is diffracted by the neighbouring carbon atoms of the cage (turquoise). For each emitter-scatterer direction, a forward-focussing component and true interference related intensity modulations are present. (b) Polar plot illustrating the forward-focussing of a diffracted wave at high kinetic energies, as calculated for an aromatic system (inset). 1200 eV corresponds to the kinetic energy of C1s photoelectrons when excited with a standard laboratory AlKα X-ray source while 625eV is a typical kinetic energy for the same level when excited at photon energies used for synchrotron-based XPD in this work.

XPD has been used to study surface structures [*77*], adsorbates [*78*] and buried interfaces [*79*]. The applicability of XPD to the study of large organic adsorbates has also been shown in the case of C_{60} [*80, 81*] and heptahelicene [*82*]. Both the energy-scanned variety and angle-resolved XPD have also been used for the analysis of small organic adsorbates [*83-86*]. Several recent reviews on the current state of the art of XPD can be found in the literature [*77, 79, 87-91*].

In the work presented in Chapters 3 and 7, an emphasis is placed on the combination of XPD and STM which allows for a more complete determination of the adsorption behaviour of large organic adsorbates due to the complementary information that can be obtained from each of the two techniques. While STM allows for the determination of adsorption sites, superstructure etc., the ability to precisely determine the conformation of an adsorbate is limited because of the sensitivity of the STM signal to the electronic rather than the geometric structure. In some studies, extensive theoretical modelling – based on DFT – has been performed for adsorbate systems to simulate STM images, which have then been compared to the measurements until a conformation which best fits the experimental appearance of an adsorbate was found [*92-94*]. The precision of this approach is however very limited and computationally expensive. XPD directly probes the local geometric order around an emitter and is hence sensitive to the property of the adsorbates, which is overlooked by the STM.

All XPD results presented in this thesis have been measured using synchrotron based XPD. Compared to standard laboratory X-ray sources, the photo-ionization cross-section of the relevant core levels of the elements present in the organic adsorbates used in this work are increased by about a factor of three at the used synchrotron energies (see Figure 6), resulting in an improved counting statistics for a given measurement time. An additional advantage of synchrotron-based XPD is that the excitation energy can be chosen below the minimum energy needed for excitation of a particular electronic shell of the substrate (in this work usually the L-shell of Cu) hence considerably reducing the number of secondary electrons present in the sample, which will limit ageing effects of the adsorbates during measurement. At the same time, Auger features involving these core levels are suppressed, lowering the secondary electron background over a wide energy range, which further improves the counting statistics.

It should be noted that unlike other diffraction based, surface-sensitive techniques, where the diffraction pattern produced by an external beam of electrons/photons is analyzed – such as LEED or surface X-ray diffraction [95] – XPD does not require long range order of the adsorbate, making the technique applicable to systems which cannot be analyzed by these techniques. What is required for XPD to be suitable for a given adsorbate system is a low number of co-existing adsorbate configurations, i.e. a low number of equally oriented emitter-scatterer systems. A system which falls within this class is the adsorption of HBC across gold step edges presented in Chapter 3.

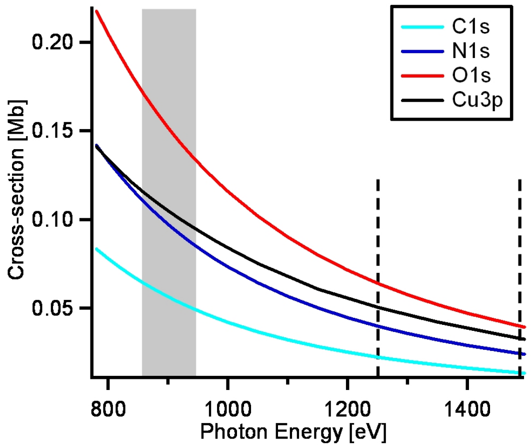

Figure 6: Photo-ionization cross-sections of core levels of organic adsorbates (and a substrate core level for illustration) as a function of photon energy. Dashed lines correspond to the photon energies of standard laboratory X-ray sources MgKα (1253.6eV) and AlKα (1486.6eV) respectively. The grey shaded area designates the photon energy interval commonly used in this thesis for synchrotron-based XPD.

2.5.1 Resonant X-ray photoelectron diffraction

The detection limit of XPS is usually specified as ~1% of a monolayer depending on the element. It may however be possible to detect even smaller quantities of adsorbates by increasing the photo-ionization cross-section for a core level of interest by choosing an appropriate photon energy, which is achieved by reducing the difference between the photon energy used for excitation and the binding energy of the core level. The cross-section can this way easily be increased by more than one order of magnitude compared to standard laboratory X-ray energies, allowing for the efficient detection of minute quantities of an adsorbate species. While this approach will strongly increase the core-level signal, leading to an increased counting statistics in XPD, the simultaneous reduction in kinetic energy of the photoelectrons is often undesirable since kinetic energies within the forward-focussing regime are favoured in XPD from large organic adsorbates in order to minimize diffraction signal due to backscattering from substrate atoms. At the same time, an increased signal to background ratio is needed under certain circumstances since integration times at every analyser position will otherwise make experiments extremely long, which may be an issue for samples sensible to radiation damage. Furthermore, diffraction signal from adsorbate photoemission lines may be shadowed by close-lying substrate photoemission lines, which can contribute to a strongly anisotropic background.

A way to circumvent these problems is to use the resonant enhancement of Auger lines by setting the photon energy to a value where a maximum in x-ray absorption spectroscopy is found as schematically shown in Figure 7a. The signal-to-background ratio of such a resonantly enhanced Auger line can easily exceed the corresponding value of the related core level by more than an order of magnitude hence considerably increasing the counting statistics. This is illustrated at the example of a monolayer of $Dy_3N@C_{80}$ on Cu(111) (see Figures 7b&7c). The signal-to-background ratio of a

Dy-MNN Auger line can be increased by a factor of about 50 compared to the Dy4d core level by setting the energy to an appropriate value.

Resonant X-ray photoelectron diffraction has been used before to study defects in TiO_2 [*96, 97*]. To be consistent with this published work, the same name for this variety of XPD is used in this thesis, even though the author feels that the technique should more correctly be referred to as resonant X-ray absorption enhanced Auger electron diffraction.

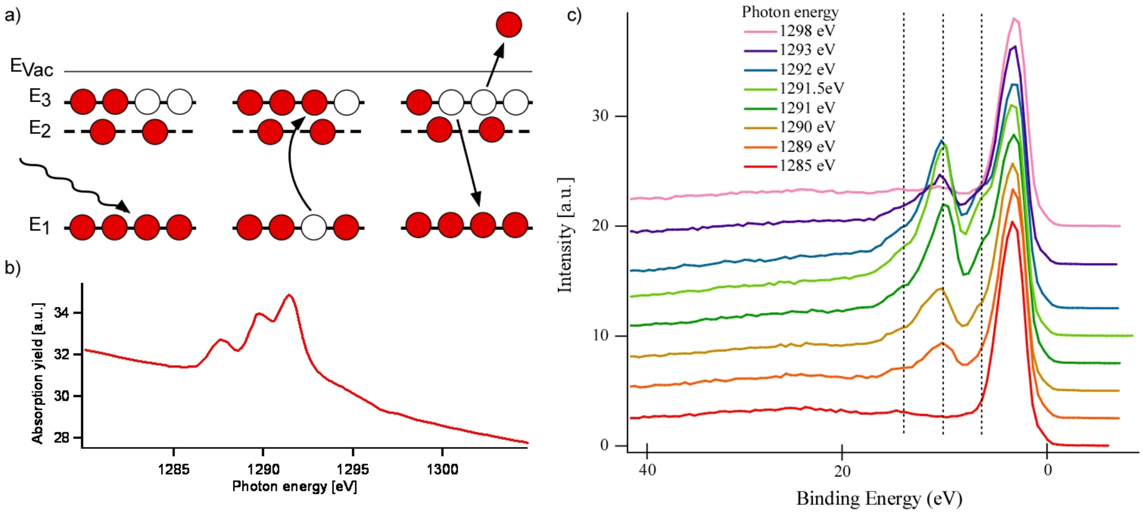

Figure 7: Resonant X-ray photoelectron diffraction. (a) Resonant absorption of a photon of energy $h\upsilon=E_3\text{-}E_1$ and subsequent excitation of an Auger electron. (b) X-ray absorption spectrum across the Dy-3d edge of a monolayer of $Dy_3N@C_{80}$ on Cu(111). (c) Enhancement of Auger features (denoted by dashed lines) as a function of photon energy. The spectra have been measured on the same sample as in (b).

2.5.2 Background subtraction in XPD

The background of inelastically scattered photoelectrons on which the elastic photoelectron peaks are sitting is not isotropic but exhibits an angular modulation. The diffraction pattern measured on the background usually has an inverted character [*98, 99*] compared to on-peak diffraction patterns of the substrate with minima instead of maxima found along high symmetry directions of the substrate. In any photoelectron diffraction experiment, the background is always inherently recorded simultaneously together with the peak signal and must therefore be properly subtracted in order to obtain the diffraction signal produced by the photoelectrons from the peak alone.

A straightforward approach to determine the background signal underneath an isolated photoemission peak is illustrated in Figure 8a. In this context, ‘isolated’ means that the background on both the high/low kinetic energy side of the peak can be taken as constant over a short energy interval, i.e. there are no in-/elastic tails of nearby peaks extending up to this peak (as illustrated in Figure 8b). The background underneath the peak can then be approximated by measuring the modulation of the diffraction pattern on the background at an energy ±ΔE away from the peak (blue arrows in Figure 8a) and taking the average between these two measurements, while also accounting for eventual differences in channeltron counting efficiencies.

For some photoemission lines this simple approach fails because of other close-lying adsorbate/substrate lines, which make it impossible to measure the ‘true’ background at a position ±ΔE from the peak (Figure 8b). In these situations it is usually only possible to measure the background on one energy side of the peak. One then has to find the optimum weight η_{opt} for which I_{peak} - $\eta_{opt} \cdot I_{peak}$ corresponds to the ‘true’ diffraction pattern produced by photoelectrons from this emission line. This can be done by ‘guessing’ an appropriate value for η which should reflect the ‘true’ height of the background at the energetic position of the peak. A new approach exploiting the symmetry properties of the peak-to-background signals has been developed and used in these cases to properly remove substrate background contributions to the measured modulation in photocurrent. Figures 8c to 8f illustrate this approach at the example of submonolayers of contorted HBC on

Cu(111) (see Chapter 4 for details on this particular adsorbate system). The diffraction pattern produced by the substrate – measured on the high kinetic energy side of the C1s peak – is – due to the C_{3v} symmetry of the substrate – threefold symmetric (Figure 8d) while the signal from the adsorbate must be six-fold symmetric due to the 6-fold symmetry of the terminal copper layer. Due to the overlaid background signal, the raw signal measured on the C1s peak (Figure 8c) has however a three-fold appearance. By subtracting a carefully weighted background, the required 6-fold symmetry can be recovered (Figure 8e). In such a situation, where the known symmetry properties of the background and adsorbate signal differ, η_{opt} can be determined by analyzing the symmetries of the background subtracted pattern as a function of η using the multipole coefficients. The multipole coefficients a_{lm} of a diffraction pattern $I(\theta,\varphi)$ are given by

$$a_{lm} = \frac{1}{4\pi}\int \chi(\theta,\varphi) Y^{*}_{lm}(\theta,\phi)\, d\Omega \qquad (7)$$

where Y^{*}_{lm} are the complex conjugates of the spherical harmonics and $\chi(\theta,\varphi)$ is the angle dependant part of the diffraction pattern which depends on the polar θ and azimuthal φ orientation of the sample. The symmetry-factor S for a given n-fold rotational symmetry is then defined as:

$$S_n = \frac{\sum_{l}\sum_{m=kn} a_{lm}}{\sum_{l,m} a_{lm}} \quad \text{where } k \text{ is an integer} \qquad (8)$$

S_n is a simple measure of the symmetry character of the pattern, based on the symmetry properties of the spherical harmonics Y_{lm} [*100*]. A spherical harmonics function Y_{lm} posses an m-fold rotational symmetry around its longitudinal axis. The numerator in equation (8) is hence the total weight of all spherical harmonics possessing a given symmetry n (including integer multiples of n) for a given pattern. The denominator is the total weight of all spherical harmonics functions. The optimum weight is then defined as the value where $\frac{S_{adsorbate}}{S_{substrate}}$ is maximized (Figure 8f).

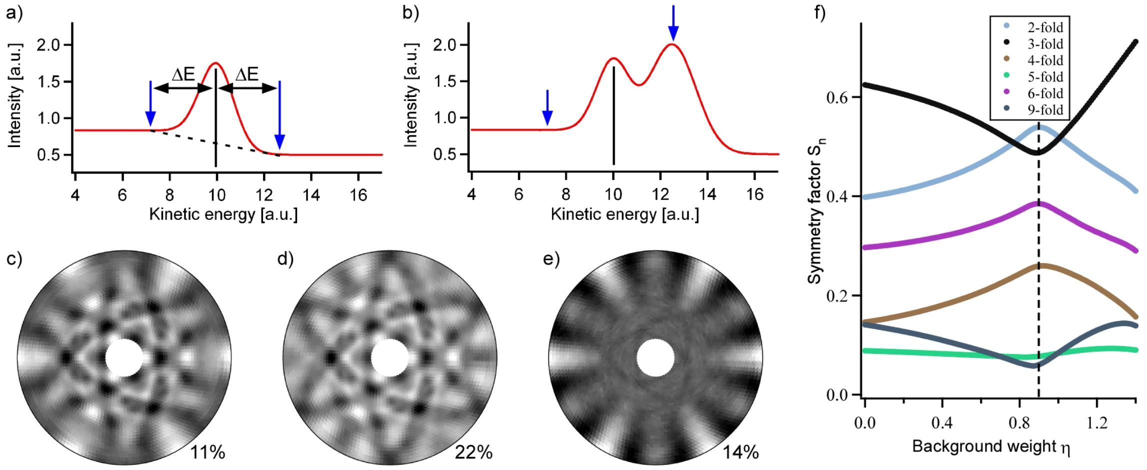

Figure 8: Background subtraction in XPD. (a) Isolated photoelectron-peak where the background at a distance ±ΔE can directly be measured and used to approximate the background underneath the peak (dashed line). (b) Schematic situation where a close-lying peak prevents measuring the background as in (a). (c)-(e) XPD patterns measured on 0.3 ML contorted HBC / Cu(111). Three-fold rotational symmetry has been imposed on all patterns. Percentages refer to the relative anisotropies of the patterns. (c) Raw XPD pattern measured on the C1s peak. (d) Background measured on the high kinetic energy side of the C1s peak. (e) Background subtracted C1s-XPD. (f) Symmetry properties of background subtracted pattern as a function of background weight. The dashed line shows the optimum weight, where 6-fold symmetry is maximized and 3-fold symmetry is minimized.

2.6 Single Scattering Cluster Simulations

While the direct assignment of diffraction maxima to nearest neighbour directions is useful for a first interpretation of photoelectron diffraction patterns within the forward-focussing energy range, the large number of nearest neighbour orientations and the manifold degrees of structural freedom of large organic adsorbates requires a more elaborate analysis of photoelectron diffraction patterns in order to be able to fully determine a maximum number of parameters for the conformation and geometry of a given adsorbate. Diffraction patterns hence have to be modelled in a more complete way. In general, modelling of a photoelectron diffraction process involves the following steps:

1. Excitation process; A photon impinging on an atom creates a spherical photoelectron source wave with quantum numbers l, m i.e. with given angular momentum symmetry.
2. Elastic scattering processes; The outgoing source wave is scattered off the neighbouring atoms.
3. Inelastic scattering; The outgoing wave is scattered inelastically leading to an attenuation of the wave amplitude.
4. Incoherence due to thermal vibrations; The coherent contribution to the elastic scattering processes is reduced.
5. Refraction; The surface potential step leads to a refraction of the outgoing wave.
6. Summation; Different paths within the sample can lead to contributions along the same orientation in vacuum. These different contributions have to be added together for the final intensity along a given direction.

In the present work, diffraction patterns have been simulated within the framework of single scattering cluster (SSC) theory [*75*]. Within this approximation, the intensity from a particular emitter is calculated as the square of the coherent sum of the unscattered photoelectron wave and all singly scattered amplitudes from neighbouring atoms.

While SSC has been widely used due to its simplicity and ability to correctly reproduce experimental patterns in a wide variety of cases, more involved modelling based on multiple scattering is being used increasingly in recent years. MSC overcomes some of the problems of SSC, e.g. the overestimation of forward-focussing peaks along atomic chains and has been shown to better reproduce fine structure features observed in photoemission patterns from Cu(111)[101]. However, MSC calculations are computationally more costly, preventing their use for large adsorbate systems where a large number of inequivalent configurations are analyzed to find the one which best reproduces the experiment. Additionally, the fine structure – resulting from multiple scattering – in photoelectron diffraction patterns recorded from large organic adsorbates is usually negligible since the patterns are dominated by maxima, which are broad compared to maxima of substrate diffraction patterns. The reason for the broadening are on one side the lower and broader forward scattering amplitude of the atoms within organic adsorbates (typically low Z-atoms such as O,C and N) and the large number of close-lying nearest neighbour directions that are present for some of the investigated adsorbates (e.g. C-C directions in C_{80}, see Chapter 7). The superposition of diffraction patterns produced by differently oriented adsorbates further leads to a broadening of the diffraction maxima.

To evaluate the quality of the fit between an experimental diffraction pattern and its simulated counterpart, a reliability Factor (R-factor) based on the multipole coefficients a_{lm} (eq. 7) of the two patterns is used [102]. The R-factor is defined as the distance between the complex multipole coefficients a_{lm} summed over all l and m:

$$R_{mp} = \sum_{l=0}^{l_{\max}} \sum_{m=-l}^{l} \left| a_{lm}^{ssc} - a_{lm}^{\exp} \right| \qquad (9)$$

Determination of adsorbate structure and geometry based on SSC and the above defined R-factor is then performed starting from a guessed structural model based on a forward-focussing model and the adsorption parameters (e.g. azimuthal orientation or tilt with respect to the surface plane) are then refined by calculating SSC patterns for all parameters within a reasonable configuration space in order to find the absolute minimum of the R-factor.

A well-known deficiency of SSC simulations is the overestimation of forward-focussing intensities [*75*]. Additionally, the computed angular dependence of the photoemission intensity as a function of polar emission angle [103] generally only roughly agrees with experiment. To minimize these effects in the computation of the *R*-factor, experimental and simulated patterns have been normalized by dividing each data point by the average computed for all data points with the same polar angle θ. The normalized data sets have then been scaled to the interval {0,1} in order to have the same anisotropy for both simulated and experimental patterns which are then compared using eq. (9).

2.7 Theoretical Methods

For the projects described in Chapters 3-7, computational modelling at different levels of theory has been performed. Calculations based on empirical and semi-empirical models have been performed by the author of this thesis using the Hyperchem program package [104]. Higher level simulation results from density functional theory (DFT) have been provided by Kristian Polatos and Werner Hofer (Chapter 3) respectively Manh-Thuong Nguyen, Carlo Pignedoli and Daniele Passerone (Chapter 5). A short introduction to the type of empirical and semi-empirical methods used in this work is given in the following two chapters. An overview on the current state of DFT can be found elsewhere [105-107].

2.7.1 Semi-empirical quantum chemistry methods

The properties of a system of *n* particles at zero temperature can be deduced from knowledge of the energy E_0 of the ground state wavefunction, which is the solution of the Hamiltonian equation

$$H\left|\Phi_0(x_1,x_2,...x_n)\right\rangle = E_0\left|\Phi_0(x_1,x_2,...x_n)\right\rangle \qquad (10)$$

For large *n* and interacting particles, finding an exact solution to the eigenvalue equation can present considerable difficulty. Therefore, approximation techniques have been developed among which the variational method. Among the most popular variational methods is the Hartree-Fock method [108-110], which derives from the central idea that the many-body problem can be replaced – as a first approximation – by an effective one-body problem where the state of mutually interacting particles $\Psi(x_1,x_2,\ldots,x_n)$ is expressed as the product of effective single-particle functions $\varphi(x_1)\varphi(x_2)\ldots\varphi(x_n)$ determined in a manner that minimizes the energy.

Semi-empirical quantum chemistry methods are based on the Hartree-Fock formalism but make additional approximations in order to fit some quantities from empirical data. The two-electron part of the Hamiltonian is not explicitly included, which renders the calculations faster compared to their *ab initio* counterparts.

In the present work, semi-empirical methods have been used routinely to determine the gas-phase conformation of individual molecules and compute the energy level splitting of interacting dimers (Austin Model 1) and to simulate approximate topographic STM images of individual molecules (extended Hückel Method).

The Austin Model 1 (AM1) [111] is based on the neglect of differential diatomic overlap integral approximation. This method has been found to well reproduce the geometric structure of a variety of molecules. The extended Hückel method [112] is – as directly stipulated by its name – a development of the earlier Hückel method [113], which in turn is a simple linear combination of atomic orbitals molecular orbitals method. It had initially been developed for the determination of the energies of molecular orbitals in conjugated hydrocarbon systems. While the initial method only included π-orbitals, the extended version also includes σ-orbitals. Electron-electron repulsions are not explicitly considered but incorporated in the form of a single-electron potential.

The electron density of the molecule, without taking the surface into account, is given by a three-dimensional reconstruction of the Slater orbitals [114] on the basis of the eigenvectors calculated by Hyperchem. To mimic a constant current STM image, the relevant molecular orbitals are integrated and a constant electron density contour is generated. Then, the vertical position of the contour is displayed in a colour-coded image [115]. The density level for which the contour is plotted can be varied in order to produce images representing different tip-sample distances and tunneling currents respectively. The experimental broadening of individual features can be mimicked by applying a gauss filter to the simulated image. An illustrative example of an STM image based on extended Hückel simulations is shown in Figure 9. Simulation of STM-images of adsorbates based on this method has proven to accurately reproduce experimental images [66, 116-120].

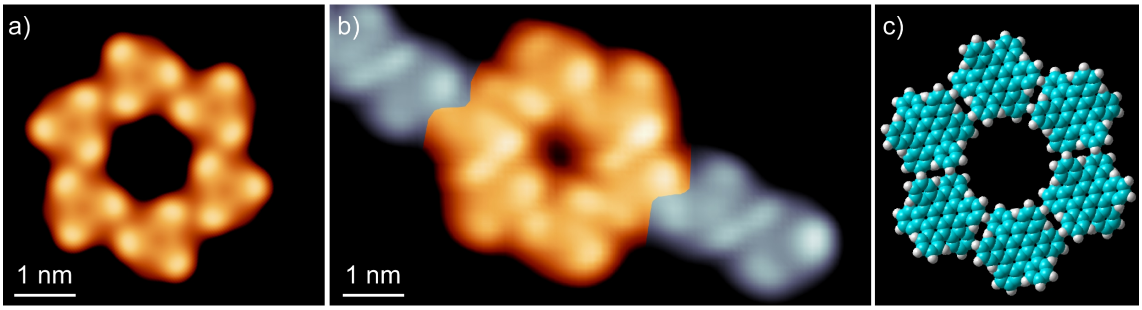

Figure 9: (a) STM image of a honeycomb consisting of six cHBC molecules based on extended Hückel simulations. (b) Corresponding experimental STM image. The molecules within the honeycomb are highlighted in yellow-orange while others are displayed in greyscale. (c) Molecular model of honeycomb cluster. Details on this adsorbate system can be found in Chapter 4.

2.7.2 Force-fields

The term *force-field* refers to an empirically derived set of parameters that are used to determine the potential energy surface and physical properties of a system of atoms and/or molecules within the framework of molecular mechanics simulations. These parameters are based on a functional form which encapsulates terms describing both covalent and noncovalent contributions to the interaction energy, such that the energy of the system is always of the form

$$E_{tot} = E_{covalent} + E_{noncovalent} = (E_{bond} + E_{angle} + E_{dihedral} + \ldots) + (E_{Van-der-Waals} + E_{electrostatic})$$

where the terms in the first (second) bracket represent the individual components of the covalent (non-covalent) interaction energies. The specific mathematical description of each term depends on the force-field. In force-fields that do not allow bond breaking, the bond and angle terms are usually modelled by harmonic oscillators. Additional terms may include improper torsional angles to enforce planarity of aromatic and conjugated systems and cross terms between internal variables. Van-der-Waals and electrostatic interactions are generally modelled by a Lennard-Jones potential and Coulombs law respectively [121].

The popularity of force-fields within the framework of molecular mechanics simulations stems from their applicability to a wide range of chemical and biological systems [122-124]. While simulations using force-fields are computationally much less costly than higher level methods, they deliver good results for molecular structure determination, especially for large molecules, which cannot be treated by higher level methods.

Individual force-fields are optimized for a given class of molecules and type of chemical interaction respectively and will hence yield best results if applied to systems belonging to the same type as the ones for which the parameters were optimized. A different set of parameters is defined for each type of atom. For example, the parameters for a carbon atom within an aromatic system would differ from those of the same atom in a carbonyl group. In the context of the present work, the CHARMM22 (Chemistry at HARvard Macromolecular Mechanics) force-field [123] has been used to compute the interaction energies between aromatic systems since this particular force-field has been shown to correctly reproduce binding of the benzene dimer [125].

3 Site-selective anchoring of a molecular building block on a templated substrate

3.1 Introduction

Surface templating is an efficient way for the creation of tailored nanostructures produced in top-down processes. It is also bound to be used in future technological combinations of top-down and bottom-up approaches [126], where self-assembled nano-units would link the pre-fabricated larger units.

The selective anchoring of a molecular building block to specific sites on a templated substrate is demonstrated in this chapter for the PAH hexa-peri-hexabenzocoronene [127] on the naturally templated vicinal Au(11 12 12) surface [128]. The long-range ordering and adsorption site(s) are determined by STM while the unusual adsorption geometry is determined by XPD. The chemical, electronic and geometrical properties of HBC can be tuned extensively through chemical functionalization [129, 130], justifying the use of this particular prototypical adsorbate, whose derivates might be used in surface-supported supramolecular architectures or even as single molecule electronics devices [131].

Molecular self-assembly guided by the steps of a vicinal Au(11 12 12) surface – respectively related vicinal surfaces – has been demonstrated before [27, 132, 133]. The work reported here is however novel, due to the unusual adsorption geometry across steps that is found for this adsorbate. Instead of forming ordered strands along steps, as observed for C_{60} [132] and a bi-molecular adsorbate system [*27*], individual molecules are stably adsorbed at kink sites with no correlation between neighbouring adsorbates. This particular adsorption behaviour bears the potential to be useful for the creation of extended two-dimensional supramolecular architectures on this template since the molecule is able to act as a connector between different terraces. In addition, the selective anchoring of a first adsorbate to well-defined sites on a template is key in the use of self-assembly for the production of nanostructures. Apart from the need for production of nanostructures of well-defined size and shape, a major issue in bottom-up creation by self-assembly is the ability to 'place' these nanostructures at pre-defined positions on the substrate (see illustration in Figure 10), since this is needed if single organic nanostructures are to be used in future electronic devices. The across-kink adsorption of HBC presented in this chapter suggests that nucleation of a structure can be controlled if selective decoration of a nucleation site by a first adsorbates is achieved. On homogeneous crystalline substrates this lateral positioning is not possible since displacing a supramolecular system by one nearest-neighbour distance results in an iso-energetic position of the latter.

On the Au(11 12 12) crystal used in this work, the ordering along the steps is unsatisfactory due to the random distribution of kinks. This deficiency might however be improved by using a naturally kinked vicinal Au(111) crystal.

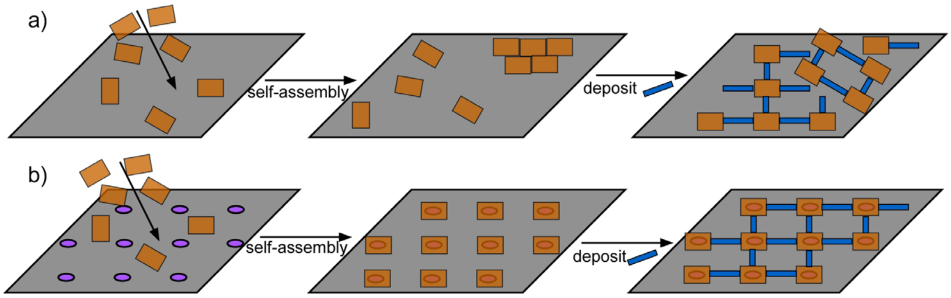

Figure 10: Schematic representation of use of site-selective anchoring of a first adsorbate in supramolecular architectures. On a homogeneous substrate (a), the supramolecular structures are randomly distributed across the substrate, while networks grown from selectively anchored adsorbates on a templated substrate (b) are highly ordered.

3.2 Living on the edge: A nanographene molecule adsorbed across gold step edges

Surface Science 602 (2008) L84–L88

Contents lists available at ScienceDirect

Surface Science

journal homepage: www.elsevier.com/locate/susc

Surface Science Letters

Living on the edge: A nanographene molecule adsorbed across gold step edges

Matthias Treier [a,*], Pascal Ruffieux [a], Richard Schillinger [b,c], Thomas Greber [b], Klaus Müllen [d], Roman Fasel [a]

[a] *Empa, Swiss Federal Laboratories for Materials Testing and Research, nanotech@surfaces Laboratory, Feuerwerkerstrasse 39, Thun 3602, Switzerland*
[b] *Physics Institute, University of Zurich, Zurich 8057, Switzerland*
[c] *Swiss Light Source, Paul Scherrer Institute, Villigen 5232, Switzerland*
[d] *Max-Planck-Institute for Polymer Research, Mainz 55128, Germany*

ARTICLE INFO

Article history:
Received 10 March 2008
Accepted for publication 25 April 2008
Available online 6 May 2008

Keywords:
Photoelectron diffraction
Scanning tunneling microscopy
Adsorption
Polycyclic aromatic hydrocarbons
Hexabenzocoronene
Au(1 1 1)
Kinks
Vicinal single crystal surfaces

ABSTRACT

The unusual adsorption geometry of the large graphene-like polycyclic aromatic hydrocarbon hexa-*peri*-hexabenzocoronene (HBC) across kinks on the stepped vicinal Au(11 12 12) surface has been studied by synchrotron radiation X-ray photoelectron diffraction (XPD) and scanning tunneling microscopy (STM). By a combination of the two techniques a complete characterisation of the adsorption behaviour is achieved, yielding information on preferential adsorption sites (STM) and molecular orientation (XPD). At low coverage (<0.15 ML) HBC adsorbs across kink sites in fcc-stacking regions with its axis rotated by 19° with respect to the step edge normal direction and the polyaromatic disc tilted by 12° relative to the (1 1 1) terraces of the substrate. Furthermore, a small fraction of HBCs adsorbs across straight step edges. The possible exploitation of the characteristic step- and kink-adsorption of molecular derivates of HBC in supramolecular architectures is exemplified at the example of the adsorption of a HBC-derivative on the same substrate.

Understanding the mechanisms that govern the adsorption, self-assembly and electronic properties of adsorbed organic molecules plays an important role towards a better insight into the organic–inorganic interface which is relevant to various fields of technology [1]. Since properties of organic nanostructures and thin films directly (and strongly) depend on the geometric order and conformation of the first layer(s), numerous studies have focussed on the determination of the adsorption behaviour of organic molecules on metallic substrates [2–6].

Scanning tunneling microscopy (STM) is among the most popular methods to characterise organic adsorbate systems in the (sub-) monolayer range. However, the information gained from STM by itself is often insufficient to allow for a complete characterisation of the adsorbate structure, geometry and possible adsorption-induced conformational changes. Combining the highly local STM with surface integrating probes such as low energy electron diffraction [7,8], normal incidence X-ray standing wavefield absorption [9] or near-edge X-ray absorption fine structure [10,11] allows for a more complete characterisation of organic adsorbate systems. Here, we show that the combination of the local and non-local probes STM and X-ray photoelectron diffraction (XPD) allows for a complete determination of the adsorption behaviour and orientation of a large organic adsorbate at low coverage.

At low coverage many adsorbates preferentially decorate surface defect sites like steps or kinks [12–14]. Depending on the electronic structure of the adsorbate, the electron rich/deficient regions below/above the step edges are preferred. An unusual adsorption geometry with the molecular π-system lying across step edges has recently been suggested for hexa-*peri*-hexabenzocoronene (HBC; see Fig. 1a) on Au(1 1 1) [15]. The specific adsorption on kink sites and a well-defined orientation of the π-system make HBC-derived molecules a potential anchor in multicomponent supramolecular networks when extended with appropriate functional side groups. However, on Au(1 1 1) there are several types of differently oriented steps and the local step density will vary considerably between different sample areas. To study the usability of the on-kink adsorption for supramolecular assemblies we have chosen Au(11 12 12), a naturally templated vicinal Au(1 1 1) crystal. Crystals of this ($n\,m\,m$) type exhibit highly regular arrays of steps in one direction and are – due to the quenching of the herringbone reconstruction – naturally patterned along the direction parallel to the steps [16]. Successive fcc- and hcp-stacking regions are separated by the so-called discommensuration lines. The resulting rectangular 5.8 × 7.2 nm superstructure has successfully been used to grow highly ordered metallic nanodots [17], molecular nanowires [18] and bi-component

---

[*] Corresponding author. Tel.: +41 332282237; fax: +41 332284490.
E-mail address: matthias.treier@empa.ch (M. Treier).

doi:10.1016/j.susc.2008.04.031

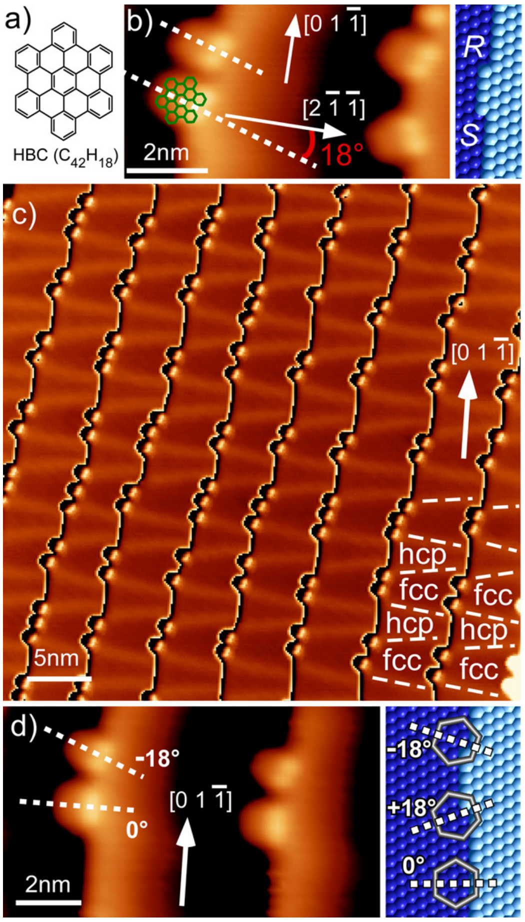

Fig. 1. Chemical structure and STM-images of ∼0.12 ML HBC on Au(11 12 12). (a) Chemical structure of HBC. (b) STM image of four kink-adsorbed HBC showing the two characteristic protrusions over the uppermost benzene rings and the rotation of the molecular axis (dashed white line) with respect to the $[2\bar{1}\bar{1}]$ step normal direction. The molecules on the right are adsorbed across a *R*- resp. *S*-type kink. A model of an *R*- and *S*-type kink is given on the right (not to scale; −50 mV; 30 pA). (c) Overview STM image showing the confinement of HBC to fcc-stacking regions. Contrast has been applied to each terrace separately (2 V; 50 pA). (d) STM image showing molecules adsorbed across kinks (upper) and molecules adsorbed across straight step edges (lower). Model of the three adsorption sites observed on Au(11 12 12) and the relative rotation of the molecular axis (dashed lines) in each case. From top to bottom: HBC adsorbed across *R*-kink, *S*-kink and straight step edge (−200 mV; 30 pA).

supramolecular structures [19]. The Au(11 12 12) surface is nominally free of kinks but will always be imperfect in reality for entropic reasons. The intrinsic kink concentration of the employed crystal depended on the exact preparation procedure and allowed for a study of the kink-adsorption of HBC on this substrate. Typical local kink concentrations were on the order of 1–3 kinks per 5.8 × 7.2 nm^2 surface unit cell.

Angle-scanned X-ray photoelectron diffraction experiments were performed at the near node-endstation of the X11MA-SIM beamline at the Swiss Light Source. Low temperature STM (LT-STM) measurements were conducted using an Omicron LT-STM. Both systems were operated at ultra high vacuum conditions with base pressure below 2×10^{-10} mbar. The Au(11 12 12) substrate was cleaned by repeated cycles of Ar^+ ion sputtering and subsequent annealing to 670 K. HBC was deposited at a deposition rate of approximately 3 ML/h from resistively heated stainless steel crucibles at 685 K onto the sample which was held at room temperature. Coverage was evaluated by comparison of the C1s signal to a reference sample of 1 ML which had been obtained by desorption of a multilayer upon heating. The synthesis of HBC is described elsewhere [20]. For the STM measurements, the sample was cooled down to 77 K after evaporation. XPD was performed with the sample held at room temperature and a photon energy of 920 eV. For XPD, the substrate orientation has been determined by the positions of the low index crystal directions in the Au4f-photoelectron diffraction pattern.

High resolution LT-STM images [21] show that HBC adsorbs across the regularly spaced steps of the Au(11 12 12) surface (Fig. 1b). The characteristic feature of this adsorption geometry are two protrusions centred above the uppermost benzene rings and a rotation of the molecular axis by 18° ± 2° with respect to the $[\bar{2}\,1\,1]$ axis of the substrate. As shown in Fig. 1c, at low coverage (<0.15 ML) only the step edges within the fcc-stacking regions are decorated, with some of the molecules lying on the discommensuration lines. Selective decoration of fcc-stacking regions on Au has been reported for various organic adsorbates in the literature [13,22]. However, a universal understanding of this stacking-selective adsorption is still missing. Up to three HBC molecules can be found within a single fcc-stacking region (including the discommensuration lines) while the step edges within the hcp-stacking regions are free from adsorbates. It should be noted that the adsorption across kinks is also found at room temperature by STM [15].

A confinement of kinks to fcc-stacking regions – as reported for Au(6 7 7) [23] – prior to deposition of HBC has been observed, implying that the kinks are already present within the fcc-regions when HBC is being deposited and are not moved to these sites by the adsorbate. The energy difference – computed by DFT [15] – between adsorption across a kink and across a straight step edge is 0.16 eV. Computed kink formation energies on vicinal Au(1 1 1) [24,25] are between 0.24 and 0.26 eV and hence substantially larger than the energy gain per molecule for adsorption across a kink as compared to adsorption across a straight step edge. Therefore, it can be concluded that HBC does not reconstruct the step edges to create a kink site but rather decorates kinks that are naturally present on this substrate with our employed substrate preparation conditions. This is confirmed by the observation of a second stable adsorption geometry where the molecule adsorbs across straight step edges in a way similar to the adsorption across kinks (see Fig. 1d). As for the on-kink adsorption, there is an apparent elevation of two of the peripheral benzene rings which is seen as an elongated protrusion in the STM images. Unlike in the kink-adsorption, the mirror axis of the molecule is perpendicular to the step edge in this adsorption geometry. Removing molecules from this site by the STM-tip – by lowering the tip-surface distance while scanning in the vicinity of the adsorbates – shows that the underlying portion of the step edge is completely straight. Since kinks are not created by the HBC molecules, the local density of molecules adsorbed across a straight step edge can vary considerably depending on the local substrate quality.

Since XPD does not require long range order of the adsorbate, it is ideally suited to study the kink-adsorption of HBC on Au(11 12 12). The C1s photoelectron diffraction pattern from a submonolayer of HBC on Au(11 12 12) is shown in Fig. 2a. The pattern corresponds to the sum of five different samples with coverages between 0.1 and 0.2 ML with a total integration time of 45 s per emission direction. All diffraction features seen in Fig. 2a are also

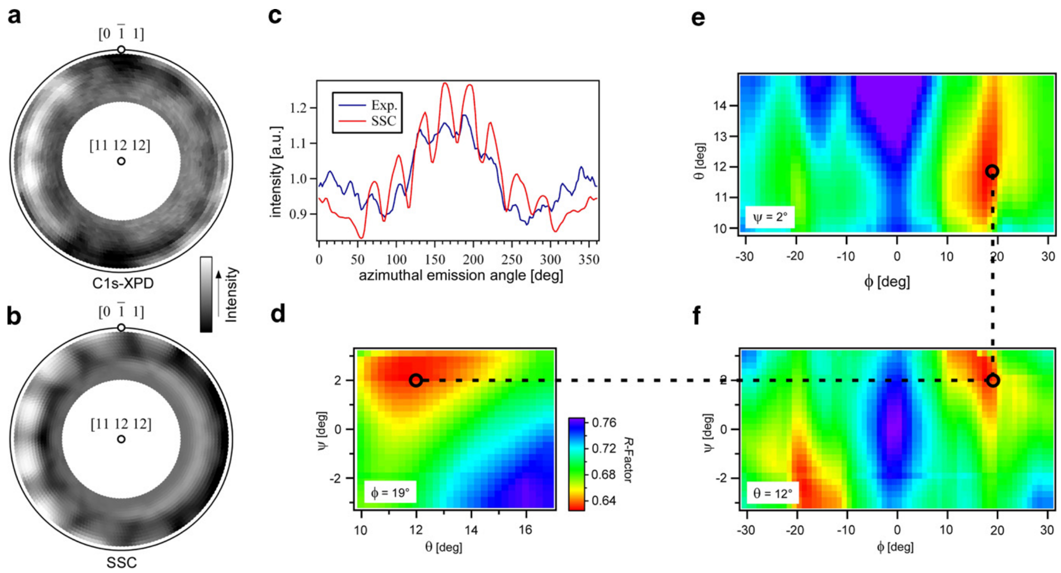

Fig. 2. (a) Experimental and (b) simulated C 1s XPD patterns of ~0.15 ML of HBC on Au(11 12 12) for polar emission angles between 86° and 56°. (c) C 1s intensity at a polar emission angle of 80°. (d)–(f) *R*-factor plots for the three angles *Φ*, *θ* and *ψ* defining the orientation of the molecular disc with respect to the Au(11 12 12) surface (see Fig. 3).

present in the individual patterns from each sample showing that all measured coverages correspond to the same adsorption regime. The samples did not show any sign of degradation during measurements. The central part of the diffraction pattern (not shown) does not show diffraction features due to the adsorbate. The diffraction maxima on the left hand side of the pattern are overlapping forward-focussing features which directly show that the molecules must be adsorbed in a tilted configuration. The asymmetry of the pattern with respect to the $(0\bar{1}1)$ plane stems from the inequivalent abundance of molecules adsorbed across *R*- and *S*-type kinks [26], thus directly reflecting the deviation of the used crystal from the nominal (11 12 12) orientation. Single scattering cluster (SSC) simulations [27] have been used to find the molecular orientation yielding the best agreement with the experiment and hence the lowest reliability factor (*R*-factor) [28]. Scattering by hydrogen atoms was neglected since the elastic scattering cross-section is negligible compared to the one of carbon. Backscattering from substrate atoms has not been included in the calculations since the backscattering yield is very low within the kinetic energy range used for this work (>600 eV). Furthermore, because of the unusual adsorption geometry the number of inequivalent carbon–substrate atom orientations and distances is very large so that backscattering from the substrate is expected to be almost isotropic. Partial wave phase shifts have been computed within a muffin-tin formalism [29]. The orientational angles of the adsorbate with respect to the substrate which were left as free parameters in the simulations are defined in Fig. 3a. The abundance of molecules adsorbed across *R*- and *S*-type kinks has equally been left as a free parameter. The simulated diffraction pattern corresponding to the minimized *R*-factor is shown in Fig. 2b. The lowest *R*-factor is obtained for $\theta = 12.0 \pm 3°$, $\Phi = 19.0° \pm 2°$, $\psi = 2.0° \pm 2°$ (see Fig. 2d–f) and a ratio of *R*- to *S*-type kinks of 4:5. Diffraction signal due to molecules adsorbed straight across steps has also been included in the simulation. It was found that less than 10% of all adsorbates are adsorbed across straight step edges, which is in line with the much lower abundance of step-adsorbed HBC compared to kink-adsorbed molecules observed by STM. The overall agreement between the experimental and simulated diffraction patterns is very good, with the positions – in both the azimuthal and polar direction – of the most prominent diffraction features being well reproduced by the simulations (see cut-views in Fig. 2c). The larger anisotropy in the simulated diffraction signal stems from the well-known overestimation of the forward-focussing peaks by SSC [27]. The orientational angles of the molecule suggest, that the adsorbate not only adopts a position that aligns its π-system with the smoothed out electron density over the step edge, but – because of the non-zero value of *ψ* – also adjusts its orientation along the step due to the smoothing of the electron density contours around the kink. These results from XPD experimentally prove that the most stable adsorption geometry (see Fig. 3b) is a tilted one as predicted by DFT. The azimuthal orientation $\Phi = 19° \pm 2°$ is in excellent agreement with both results from STM (18° ± 2°) and DFT (17°). The experimentally determined tilt angle $\theta = 12° \pm 3°$ with respect to the terraces is somewhat larger than the corresponding value suggested by DFT (9°) but clearly confirms the unusual tilted adsorption geometry.

In the gas phase, the polyaromatic disc of HBC is perfectly planar. However, there are several almost isoenergetic conformations [30]. A slightly nonplanar conformation has been suggested by DFT [15] for kink-adsorbed HBC with some of the outer benzene rings tilted by up to 2° with respect to the coronene core. Because of the multitude of isoenergetic conformations in the gas phase, a small adsorption-induced conformational change is likely to accompany the adsorption process as the energetic cost to change the conformation is low. It was not possible to evidence or exclude such small conformational changes from the SSC calculations since the variation in *R*-factor is too low to yield unambiguous information.

The unusual adsorption of HBC across straight and kinked step edges may be used in supramolecular assemblies by anchoring a properly functionalized HBC-derivate within the fcc-stacking regions of a Au(*nmm*) crystal surface. A subsequently deposited molecular species with matching functionalization can then be

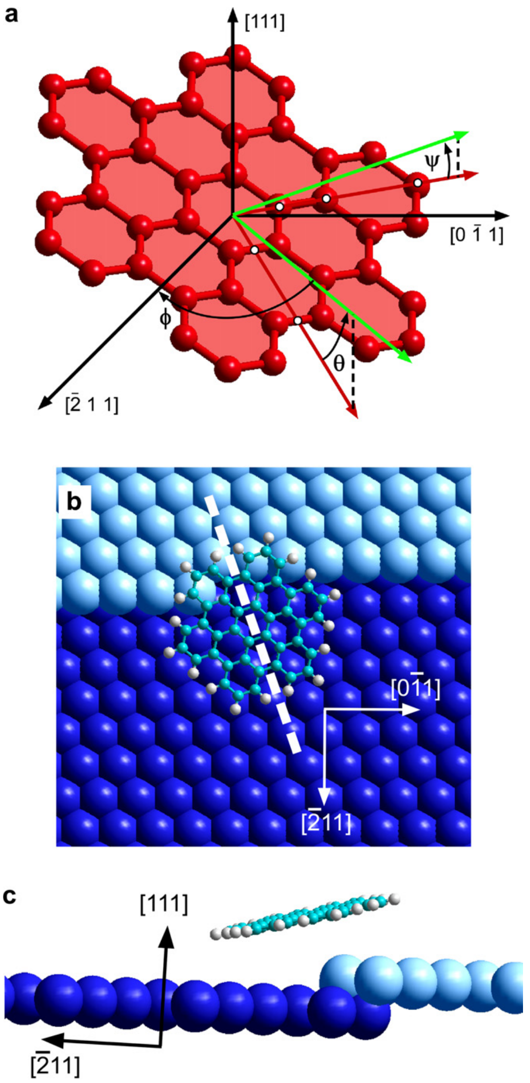

Fig. 3. (a) Definition of orientational angles for across-kink adsorption of HBC on Au(11 12 12). The red axes are lying in the plane of the molecular disc. Green arrows correspond to projections of the red axes onto (1 1 1) along [1 1 1]. (b) Visualization of the tilted adsorption geometry of HBC across a *S*-type kink. The dashed line visualizes the molecular axis (see also Fig. 1). (For interpretation of the references to colour in this figure legend, the reader is referred to the web version of this article.)

used to form template-mediated supramolecular assemblies. In Fig. 4 we show that dodecamethyl-HBC (ddmHBC) adsorbs in a way similar to HBC across steps and kinks within fcc-stacking regions on Au(11 12 12). Simulated STM-images based on extended Hückel calculations of ddmHBC show that molecules adsorbed in a planar way on the flat terrace should be imaged as three identical elongated protrusions centred over two neighbouring upwards-facing methyl-groups. Three protrusions can be discerned on the molecules shown in Fig. 4. These protrusions have significantly different apparent heights with the two protrusions lying on the upper terraces appearing 1.5–2.5 Å higher than their counterpart

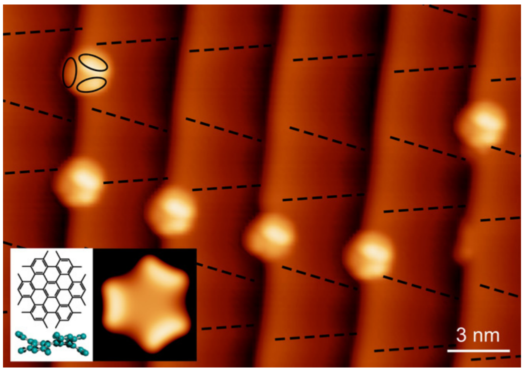

Fig. 4. STM image showing kink- and step-decoration of ddmHBC. Molecules are imaged as three elongated protrusions (visualized on a molecule on the upper left side) of which two appear higher than the third one. Dashed lines indicate the position of the discommensuration lines (tunneling parameters: −1.9 V; 20 pA). The insets show the chemical structure and nonplanarity of ddmHBC and a simulated STM image for a molecule adsorbed on a planar terrace based on extended Hückel calculations.

on the lower terrace. Based on the tilted adsorption geometry determined for HBC we conclude that ddmHBC also adsorbs in a tilted way across steps and kinks. Even though the π-system of ddmHBC is distorted (inset Fig. 4) and lifted above the surface because of the methyl groups, the adsorption behaviour is very similar to HBC. Due to their tilted adsorption geometry across kinks and step edges, functionalized HBCs may thus be used as anchoring molecules on Au(nmm) template surfaces and act as specific linkers between supramolecular assemblies on adjacent terraces.

In conclusion, we have shown that synchrotron-based XPD can be used for the determination of the orientation of large organic adsorbates at coverages as low as 0.15 ML if the number of coexisting adsorption configurations is small. The adsorption geometry of HBC on Au(11 12 12) determined by XPD experimentally confirms the tilted adsorption of HBC across gold kinks suggested by DFT. Furthermore, we have shown how the tilted adsorption across step edges of functionalized HBC-derivates may be exploited in supramolecular assemblies on naturally templated vicinal Au surfaces.

Acknowledgements

XPD experiments have been performed at the Swiss Light Source (SLS); generous allocation of synchrotron beamtime is gratefully acknowledged. We would like to thank F. Nolting and the staff at the SIM Beamline for experimental support. Financial support by the Swiss National Science Foundation and the NCCR “Nanoscale Science” is gratefully acknowledged.

References

[1] S.R. Forrest, Nature 428 (2004) 911.
[2] J.A. Theobald, N.S. Oxtoby, M.A. Phillips, N.R. Champness, P.H. Beton, Nature 424 (2003) 1029.
[3] J.V. Barth, Ann. Rev. Phys. Chem. 58 (2007) 375.
[4] G. Pawin, K.L. Wong, K.-Y. Kwon, L. Bartels, Science 313 (2006) 961.
[5] F. Rosei, M. Schunack, Y. Naitoh, P. Jiang, A. Gourdon, E. Laegsgaard, I. Stensgaard, C. Joachim, F. Besenbacher, Prog. Surf. Sci. 71 (2003) 95.
[6] S.M. Barlow, R. Raval, Surf. Sci. Rep. 50 (2003) 201.
[7] K. Glockler, C. Seidel, A. Soukopp, M. Sokolowski, E. Umbach, M. Böhringer, R. Berndt, W.D. Schneider, Surf. Sci. 405 (1998) 1.
[8] V.A. Langlais, Y. Gauthier, H. Belkhir, O. Maresca, Phys. Rev. B 72 (2005) 085444.
[9] D.P. Woodruff, Appl. Surf. Sci. 254 (2007) 76.
[10] M.E. Cañas-Ventura, F. Klappenberger, S. Clair, S. Pons, K. Kern, H. Brune, T. Strunskus, C. Wöll, R. Fasel, J.V. Barth, J. Chem. Phys. 125 (2006) 184710.

[11] M. Böhringer, K. Morgenstern, W.D. Schneider, M. Wuhn, C. Wöll, R. Berndt, Surf. Sci. 444 (2000) 199.
[12] T. Zambelli, P. Jiang, J. Lagoute, S.E. Grillo, S. Gauthier, A. Gourdon, C. Joachim, Phys. Rev. B 66 (2002) 075410.
[13] M. Vladimirova, M. Stengel, A. De Vita, A. Baldereschi, M. Böhringer, K. Morgenstern, R. Berndt, W.-D. Schneider, Europhys. Lett. 56 (2001) 254.
[14] J.I. Pascual, J.J. Jackiw, K.F. Kelly, H. Conrad, H.-P. Rust, P.S. Weiss, Phys. Rev. B 62 (2000) 12632.
[15] P. Ruffieux, K. Palotas, O. Gröning, D. Wasserfallen, K. Müllen, W.A. Hofer, P. Gröning, R. Fasel, J. Am. Chem. Soc. 129 (2007) 5007.
[16] S. Rousset, V. Repain, Y. Garreau, J. Lecoeur, J. Phys. Condens. Mater. 15 (2003) S3363.
[17] V. Repain, G. Baudot, H. Ellmer, S. Rousset, Europhys. Lett. 58 (2002) 730.
[18] N. Néel, J. Kröger, R. Berndt, Appl. Phys. Lett. 88 (2006) 163101.
[19] M.E. Cañas-Ventura, W. Xiao, D. Wasserfallen, K. Müllen, H. Brune, J.V. Barth, R. Fasel, Angew. Chem. Int. Ed. 46 (2007) 1814.
[20] V.S. Iyer, M. Wehmeier, J.D. Brand, M.A. Keegstra, K. Müllen, Angew. Chem. Int. Ed. 36 (1997) 1604.
[21] I. Horcas, R. Fernandez, J.M. Gomez-Rodriguez, J. Colchero, J. Gomez-Herrero, A.M. Baro, Rev. Sci. Instr. 78 (2007) 013705.
[22] W. Xiao, P. Ruffieux, K. Ait-Mansour, O. Gröning, K. Palotas, W.A. Hofer, P. Gröning, R. Fasel, J. Phys. Chem. B 110 (2006) 21394.
[23] F. Leroy, G. Renaud, A. Létoublon, S. Rohart, Y. Girard, V. Repain, S. Rousset, A. Coati, Y. Garreau, Phys. Rev. B 77 (2008) 045430.
[24] L. Vitos, H.L. Skriver, J. Kollar, Surf. Sci. 425 (1999) 212.
[25] C.-L. Liu, J.B. Adams, Surf. Sci. 294 (1993) 211.
[26] A. Ahmadi, G. Attard, J. Feliu, A. Rodes, Langmuir 15 (1999) 2420.
[27] C.S. Fadley, in: R.Z. Bachrach (Ed.), Synchrotron Radiation Research: Advances in Surface Science, vol. 1, Plenum, New York, 1990, pp. 421–518.
[28] R. Fasel, P. Aebi, J. Osterwalder, L. Schlapbach, R.G. Agostino, G. Chiarello, Phys. Rev. B 50 (1994) 14516.
[29] J.B. Pendry, Low Energy Electron Diffraction, Academic press, London, 1974.
[30] A. Soncini, E. Steiner, P.W. Fowler, R.W.A. Havenith, L.W. Jenneskens, Chem. Eur. J. 9 (2003) 2974.

3.3 *Further aspects and outlook*

3.3.1 Mechanism behind across step adsorption of PAHs

A tilted adsorption geometry across step edges has not only been found for HBC and ddmHBC on Au(11 12 12) but also for other molecules with a polycyclic aromatic core. While it is widely accepted that adsorbates will on most surfaces preferentially decorate defects (e.g. steps, kinks) at low coverage, a complete understanding of the mechanisms governing this empirically derived rule is still missing. It has been suggested that electro-/nucleophilic adsorbates will preferentially decorate the lower/upper step edges [134, 135] due to the increased/decreased electron density resulting from an electron overspill due to the Smoluchowski effect [136]. However, detailed theoretical modelling has only been performed for few adsorbate systems [137, 138]. We have observed that contorted HBC (cHBC) [139], octobenzocircumbiphenylene (OBC) [140] and permethoxylated HBC (pHBC) [129] adsorb in a tilted geometry across step edges on different surfaces (Figure 11) resembling the adsorption geometries found for HBC and ddmHBC, suggesting that this adsorption behaviour is an inherent property of molecules containing an extended aromatic core and is valid for adsorption on most low-index inert metal surfaces and not only for adsorption on B-type steps on Au(111). It should also be noted that cHBC, OBC and pHBC are all nonplanar due to steric hindrance in the peripheral units, further proving that the across-step adsorption does not crucially depend on the planarity of the π-system as already suggested in the previous chapter, based on the results on ddmHBC.

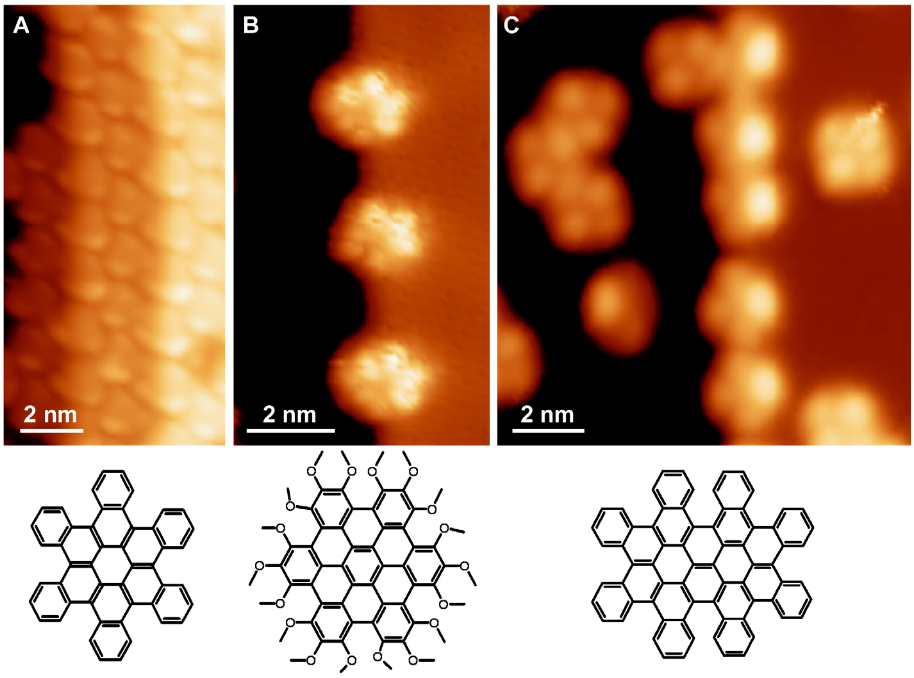

Figure 11: Across-step adsorption of molecules with a large aromatic core. (a) cHBC / Cu(111) (b) pHBC / Au(111) (c) OBC / Cu(110). Molecular structures are shown in the bottom part of the images.

At the present stage, we explain this general trend by a gain in adsorption energy resulting from a dipole-induced dipole interaction between the lateral component of the dipole at the step edge and the polarizeable polyaromatic system, as schematically shown in Figure 12. The interaction energy between a fixed dipole u and a polarizable system with polarizability α at a distance r is given by

$$E_{dipole-induced\ dipole} = \frac{u^2 \alpha (1 + 3\cos^2 \theta)}{2(4\pi\varepsilon_0)^2 r^6} \qquad (11)$$

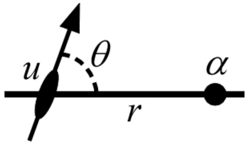

The common property of all mentioned molecules is the comparably high polarizability due to the polyaromatic core. For HBC the polarizability is 116 Å^3 in the plane of the polyaromatic board and

$30\,\text{Å}^3$ orthogonal to this plane [141]. While polarization of the adsorbate orthogonal to the surface may be present and contribute to the adsorption energy at all adsorption sites (terraces or steps), a fixed lateral dipole moment is only present at step edges. Using equation (11) a typical adsorption height of 3.25 Å for PAHs on Au(111) [142] and further assuming a lateral dipole of the order of the orthogonal component at the step edge (~0.2D/edge atom) [143], an interaction energy of ~3 meV is obtained. While this energy appears too small compared to the observed strong selectivity and stability of across-step adsorption for these systems, a more complete modelling of the dipolar field across a step edge and a microscopic treatment of dipole-induced dipole interactions will yield a more meaningful result. Preliminary calculations for HBC on B-type Au step edges [144] show an interaction energy of the order of 30-50 meV, which appears to be on the correct order of magnitude to explain the highly selective nucleation across step edges. Astonishingly, there seem to be no theoretical studies of the lateral dipolar field of step edges to date. A detailed understanding of the electronic distributions across step edges would yield information relevant to catalysis, since these defect sites are key elements in catalytic processes [145]. The orthogonal component of the step-dipole has however been determined experimentally for different surfaces [143, 146, 147].

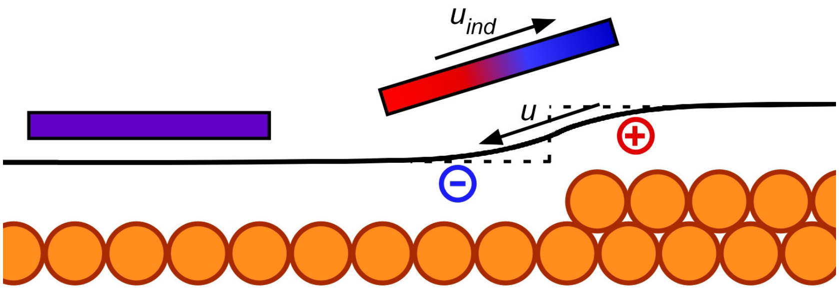

Figure 12: Schematic model of tilted step adsorption of polycyclic aromatic adsorbates driven by dipole-induced dipole interaction. Due to the electron overspill across the physical step edge (dashed lines), there is charge accumulation/depletion on the lower/upper terrace near the step edge resulting in a dipole u which induces a dipole u_{ind} in the polarizable π-board of the adsorbate. On the flat terrace (left) there is no net lateral dipole leaving the adsorbate with no net polarization in the plane parallel to the surface.

3.3.2 HBC/ Au(11 12 12): A benchmark system for theoretical modelling?

In the manuscript presented in the previous chapter, only low coverages <0.15 ML of HBC on Au(11 12 12) have been analyzed. By increasing the coverage in a stepwise fashion, the relative energy of different possible adsorption sites has been determined. In order of decreasing adsorption energy, these are (Figure 13):

1 across-kink adsorption within *fcc*-stacking areas (~<0.1-0.12 ML)
2 across-step adsorption within *fcc*-stacking areas (<0.15 ML)
3 across-step adsorption within *hcp*-stacking areas (0.15 ML < x <0.25 ML)
4 single occupation of *fcc*-areas on terraces (>0.25 ML)
5 single occupation of *hcp*-areas on terraces (>0.30 ML)

At even higher coverages, molecules are distributed across the terraces in a way which maximizes the intermolecular distances. The adsorbate-adsorbate interaction hence appears to be repulsive.

This particular adsorbate system with its energetically inequivalent adsorption sites may hence be used as a reference system for future model calculations of adsorption on Au(111). In a semi-empirical approach, a model may be refined until the clear dependency on substrate stacking and selective kink/step decoration of HBC is reproduced.

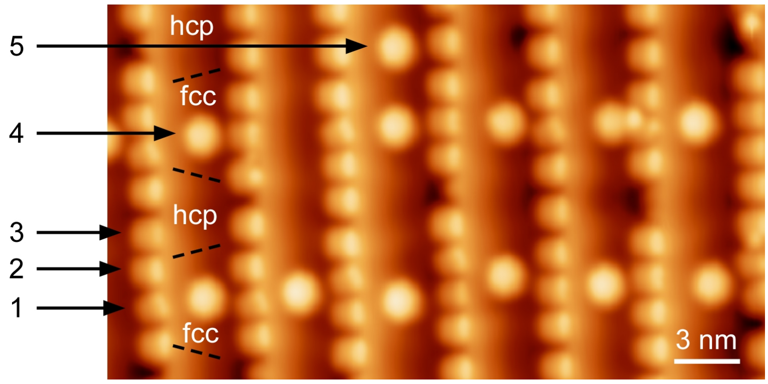

Figure 13: Adsorption sites of HBC on Au(11 12 12). Dashed lines indicate the positions of the discommensuration lines. See text for details on the adsorption sites numbered 1 to 5. Scan parameters: -0.2V, 100pA, 5K.

3.3.3 Mapping the adsorption potential landscape of a constrained adsorbate

When imaging at 77 K, individual HBC molecules on Au(111) terraces cannot be imaged stably even at very high gap resistances. These molecules are imaged as smeared-out, fuzzy protrusions with the apparent size depending on the employed gap resistance (Figures 14a-14c). If the tip is brought closer to the substrate (i.e. if the gap resistance is lowered) the apparent size of the adsorbates increases. From this mode of imaging we conclude that individual molecules are mobile but constrained to single *fcc/hcp*-stacking regions between two step edges at this temperature. The molecular motion can be frozen out by cooling down the sample to 5 K where all adsorbates, including individual molecules on terraces can be imaged stably for typically employed gap resistances (Figure 14d).

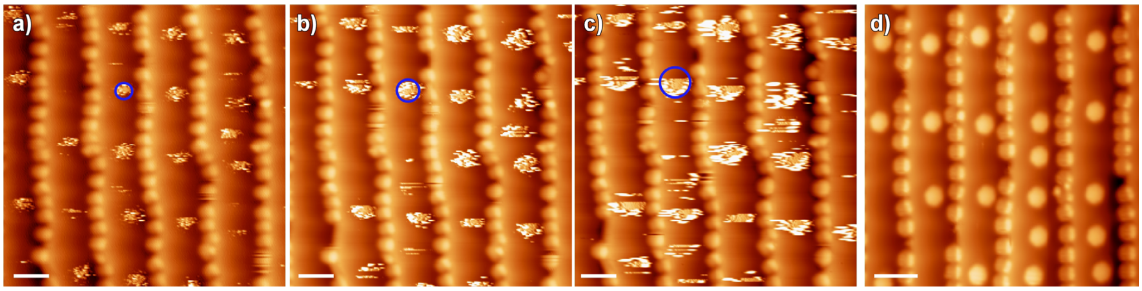

Figure 14: Constrained mobility of HBC on Au(11 12 12). STM images (a) to (c) have been recorded at 77 K while (d) was measured at 5 K. Scale bars are 4nm in each image. Blue circles in (a) to (c) visualize the increase in apparent shape of a mobile single HBC as a function of gap resistance. Diameters of the circles are (a) 1.9 nm (b) 2.5 nm (c) 3.4 nm. Scan parameters: (a) -1.8V, 9pA (b) -1.8V, 250pA (c) -1.8V, 2000pA (d) -2V, 1000pA.

Qualitatively, we explain the apparent size-dependence of the HBCs as a function of tip-position by the following model (Figure 15). The discommensuration lines are potential barriers within the adsorption potential of HBC, i.e. the adsorption energy is lowest on the discommensuration lines. This results in a lateral modulation of the adsorption potential experienced by a single molecule as a function of position on the terrace and thus the stacking of the underlying substrate. This potential landscape has a minimum at the centre between the discommensuration lines and a maximum on the latter. When scanning with the STM-tip in the close vicinity of the molecule, attractive interactions between the tip and the adsorbate (e.g. Van-der-Waals interactions) are present [148]. The molecule will hence be slightly ‘lifted’ from the substrate due to this attractive interaction allowing it to explore a larger region of the potential well, resulting in an increased apparent size. The closer the tip is brought to the surface (i.e. the lower the gap resistance), the stronger are the attractive interactions with the adsorbate, which allows the latter to be displaced further up on the adsorption potential energy curve. It is hence possible to determine the adsorption potential ‘felt’ by an adsorbate by measuring its apparent shape as a function of tip-adsorbate interactions.

However, it is important to note that the apparent shape of single HBCs not only depends on the gap resistance but also on the shape of the tip at the apex. Modifying the tip apex – e.g. by dipping it into the metal substrate – will alter the apparent size at a given gap resistance. This impedes theoretical modelling of adsorbate-tip interactions for a realistic tip, which will eventually determine if the method can be used only for the qualitative or also a quantitative description of the adsorption potential of adsorbates.

A way to partially remove the dependence on the tip shape is to monitor the apparent size at a high gap resistance with the same tip as a function of temperature. Mobility is ‘switched on’ at a temperature between 5 K and 77 K. At higher temperatures, thermal energy allows individual molecules to move within a larger portion of their potential well, leading to an increase in apparent size. If the gap resistance is chosen such that tip-adsorbate interactions are small compared to the thermal energy of the adsorbate at a given temperature, the population of each site within the potential well is determined by Boltzmann statistics. Analyzing the apparent size as a function of temperature should hence allow for a more quantitative evaluation of the adsorption potential.

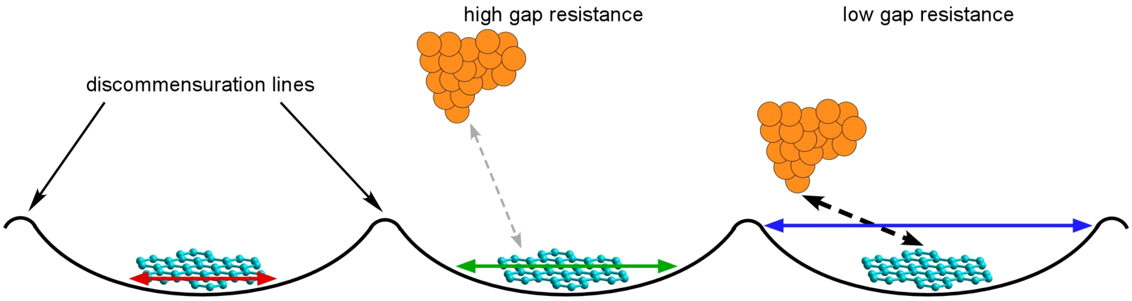

Figure 15: Model used to explain dependence of apparent size of HBC on Au(11 12 12) as a function of gap resistance. The mobility of HBC is intrinsically constrained by an adsorption potential with maxima centred over the discommensuration lines (black curve) leading to an apparent size of HBC visualized by the red arrow. At high gap resistance there is little attractive interaction between tip and adsorbates which hence only leads to a small increase in apparent size (green arrow) while at low gap resistance the tip strongly attracts the adsorbate hence allowing it to ‘climb’ further up the adsorption potential barriers leading to a strongly increased apparent size (blue arrow).

4 Supramolecular architectures based on aromatic interactions

4.1 Introduction

Many organic molecules whose adsorption behaviour has been studied on single crystal metal surfaces contain (poly)aromatic units. This is often motivated by the potential use of such substances in molecular electronic devices since aromatic units appear to be a unifying design feature of most organic semiconductors [149-151]. Molecular junctions based on aromatic interactions have been proven to be conducting even at the single molecule level [152].

Astonishingly, there seem to be no studies where aromatic interactions in two dimensions are quantitatively analyzed, even though they have been suggested to play a role in the self-assembly of large organic molecules on metal surfaces [153, 154]. There are two main reasons why these interactions have only been tentatively described in previous studies: First, aromatic interactions are very versatile as shown in Figures 16a&b. Attractive geometries between two benzene rings are such that the rings can face each other at every possible angle between 0° and 180° with an attractive geometry existing for every angle (by adjusting the offset between the rings or vice-versa). Experimentally, this versatility is proven by an analysis of the relative orientation between phenyl rings (Figure 16b) in protein crystals, which are found to be bound together in geometrical arrangements which cover all the theoretically predicted attractive configurational space (Figure 16a). The apparent non-directionality of aromatic interactions is in strong contrast to the directionality of other non-covalent interactions such as hydrogen bonds which have been shown to be strongly directional [155]. To be able to predict the contribution from aromatic interaction for a given adsorbate, its conformation on the surface has hence to be known, a requirement which is not routinely achieved by STM studies alone, especially if conformationally flexible aromatic units such as phenyl rings are present. On the other hand, Van-der-Waals interactions are one of the main contributions to aromatic interactions [156]. These dispersive interactions are however not reproduced by standard DFT simulations, which are widely employed for the theoretical analysis of such systems.

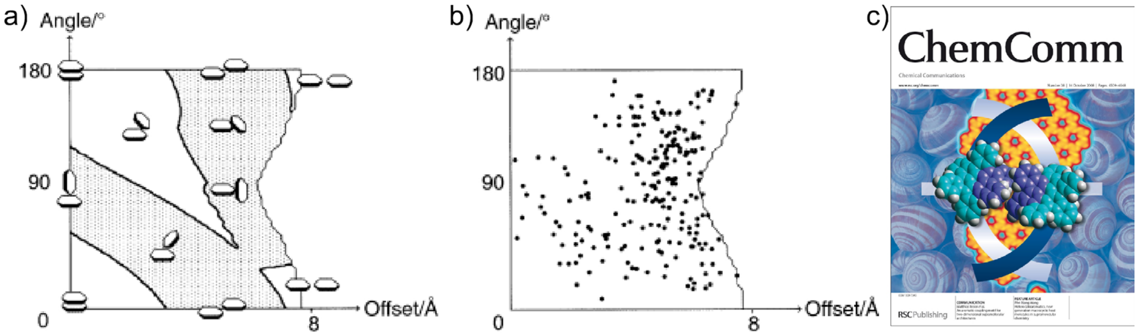

Figure 16: (a) Electrostatic interaction between two benzene rings as a function of relative orientation [157]. Shaded/unshaded areas designate attractive/repulsive interaction. (b) Geometries of phenylalanine side chain interactions observed in protein X-ray crystal structures. Figures a&b have been taken from reference [156]. (c) Inside front cover of Chemical Communications (issue 38, 2008) featuring the article presented in this chapter.

In this chapter, the self-assembly of the nonplanar PAH cHBC is shown to be governed by aromatic interactions between interdigitating helical aromatic units, which can be quantified using simple force-field simulations since the aromatic coupling motifs[3] responsible for the attractive interactions are rigid and their geometry in the adsorbed state is hence known. This first study opens the way for rationally designed and functional supramolecular structures based on aromatic interactions (Figure 17).

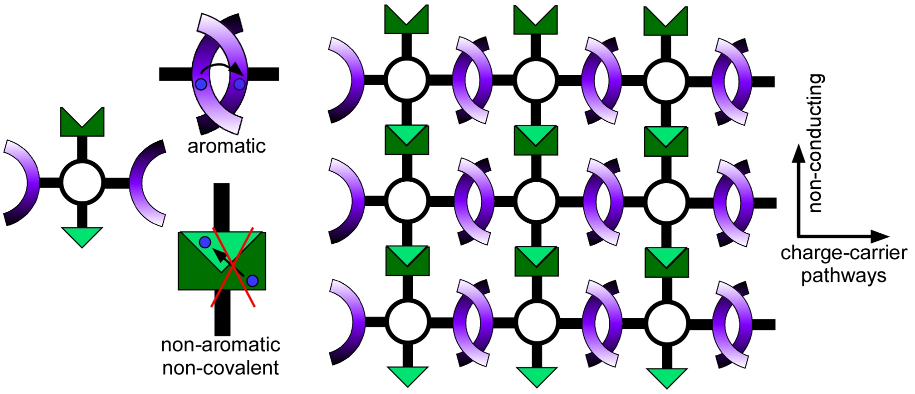

Figure 17: Schematic representation of a supramolecular system based on aromatic (violet) and non-aromatic (green) binding motifs. The aromatic coupling motifs have the additional advantage to allow charge-carrier pathways.

---

[3] It should be noted that the expression “coupling motif” instead of “binding motif” – which is commonly used in supramolecular architectures – is used for this particular system to emphasize that, apart from the intermolecular binding that is mediated by interdigitating helical aromatic units (which makes them a binding motif), the interdigitated geometry is also expected to lead to electronic coupling between π-orbitals, extending the use of aromatic coupling motifs beyond the one of “simple” structural binding motifs to applications in molecular electronics.

4.2 An aromatic coupling motif for two-dimensional supramolecular architectures

COMMUNICATION www.rsc.org/chemcomm | ChemComm

An aromatic coupling motif for two-dimensional supramolecular architectures†

**Matthias Treier,*[a] Pascal Ruffieux,[a] Pierangelo Gröning,[a] Shengxiong Xiao,[b]
Colin Nuckolls[b] and Roman Fasel[a]**

Received (in Cambridge, UK) 6th June 2008, Accepted 11th August 2008
First published as an Advance Article on the web 27th August 2008
DOI: 10.1039/b809618j

We show, using scanning tunneling microscopy, how a coupling motif based on self-complementary helical aromatic units is able to drive the formation of a chiral porous supramolecular network and chains based on lateral aromatic interactions in two dimensions.

Self-assembly is a promising concept for the nanoscale fabrication of future molecular electronic devices[1] allowing for 'automatic' bottom-up production guided by the design of the molecular building blocks and the underlying substrate surface.[2] Molecules containing polycyclic aromatic units are among the most promising candidates for such applications because of the comparably high charge carrier mobilities that can be achieved.[3] By adapting the principles of supramolecular chemistry to the two-dimensional (2D) case, supramolecular nanostructures of such molecules have been realized on single crystal surfaces by hydrogen bonding[4] and metal-coordination.[5] However, these types of bonds are generally non-conducting, which prevents nanoelectronic applications. We report on a lateral coupling motif which has the potential to overcome this problem by the use of aromatic interactions. This coupling motif, consisting of two self-complementary helical aromatic units, is capable of driving the formation of 2D supramolecular structures and holds promise for organizing charge carrier pathways.

Submonolayer coverage self-assembly of the non-planar polycyclic aromatic hydrocarbon (PAH) hexa-*cata*-hexabenzocoronene (HBC)[6] (Fig. 1) on Cu(111) has been investigated by scanning tunneling microscopy (STM). Sample preparation and measurements were conducted in an ultra high vacuum system with a base pressure below 2×10^{-10} mbar using an Omicron low temperature STM. The Cu(111) substrate was cleaned by repeated cycles of Ar^+ ion sputtering and subsequent annealing to 750 K. HBC has been deposited on the clean single crystal surface under ultra high vacuum at a rate of approximately 0.1 ML min^{-1} from resistively heated quartz crucibles at 560 K. During deposition, the sample was kept at room temperature and subsequently cooled down to 77 K for STM analysis.

At submonolayer HBC coverage, large islands of a porous network are formed, where each hole is surrounded by six HBC molecules (Fig. 1a). Neighboring molecules are rotated by 180° with respect to each other, such that upwards-/downwards-facing neighboring aromatic rings of one HBC molecule are pointing towards a downwards-/upwards-facing pair of rings of the neighboring molecule. The lateral binding motif consists of two interdigitated self-complementary helical aromatic units facing (and partially interlocked with) each other.

The same coupling motif can also lead to linear supramolecular chains (Fig. 1b) that show the same intermolecular distance and identical molecular orientation with respect to the substrate. The orientation of the adsorbate with respect to the Cu substrate is typical for adsorption of PAHs on this substrate, with acene units being aligned with close-packed directions of the substrate.[7] Partial overlap between π-electron systems of neighboring molecules makes the linear structures

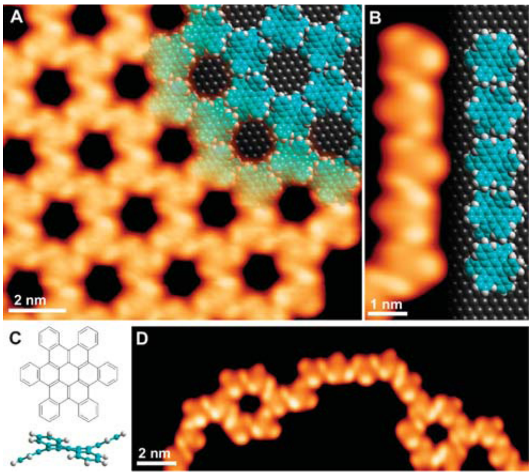

Fig. 1 (a) STM image‡ (−1.8 V, 30 pA) of a supramolecular HBC honeycomb network with 2.3 nm pore-to-pore distance and molecular model. (b) STM image (−1.9 V, 20 pA) and model of linear chain formed through the same coupling motif. (c) Chemical structure of HBC. The side view visualizes the non-planarity of the aromatic system. (d) STM image (−2.1 V, 50 pA) of interconnected linear strands and honeycomb structures of opposite chirality.

---

[a] *Empa, Swiss Federal Laboratories for Materials Testing and Research, nanotech@surfaces laboratory, Feuerwerkerstrasse 39, 3602 Thun, Switzerland. E-mail: matthias.treier@empa.ch; Fax: +41 33 228 44 90; Tel: +41 33 228 22 37*
[b] *Columbia University, Department of Chemistry, Havemeyer Mail Code 3130, 3000 Broadway, New York, NY 10027, USA*

† Electronic supplementary information (ESI) available: Experimental data (large scale STM images and manipulation of polymolecular units) and definition of tetrahelicene units. See DOI: 10.1039/b809618j

potential nanowire-like conductors. The orbital overlap results in a splitting of the HOMO/LUMO levels which gives rise to an increased mobility for holes/electrons.[8] These linear structures are observed growing out from step edges of the underlying substrate surface or as connections between honeycomb structures as shown in Fig. 1d.

For a given peripheral carbon ring, two mirror-symmetric enantiomers of the helical units can be defined (*M*- and *P*-tetrahelicene, see ESI for details†) leading to two inequivalent coupling directions and hence, to two chiral domains of the honeycomb network (Fig. 2a). Both domains are experimentally observed and correspond to commensurate 9 × 9 superstructures, with two molecules per unit cell. Lateral coupling *via* the *M*-tetrahelicene units gives rise to "left-handed" λ-domains of the honeycomb network, whereas "right-handed" ρ-domains consist of HBC molecules coupled *via* their *P*-tetrahelicene units (see Fig. 2b). It should be noted, that honeycombs are enantiopure (in the coupling motif) whereas linear strands correspond to enantiomeric mixtures of *M*–*M* and *P*–*P*-coupled units.

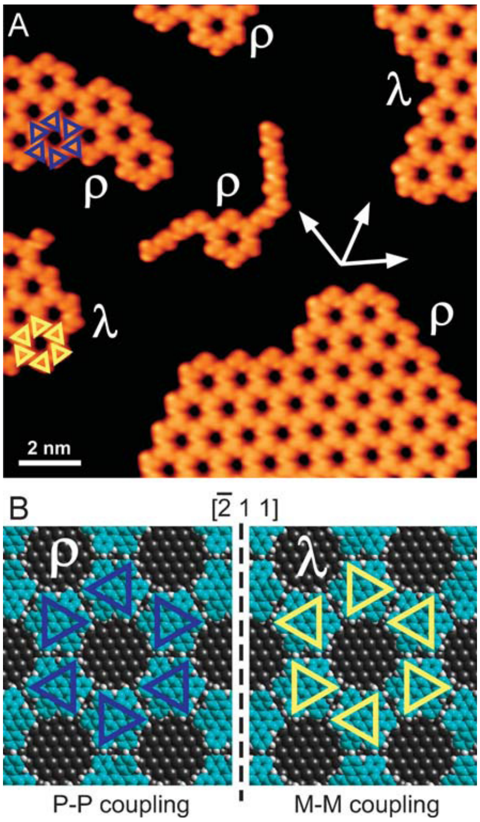

Fig. 2 (a) STM image (−1.9 V, 20 pA) showing the two chiral domains of the honeycomb network. The arrows indicate the orientation of the close-packed directions of the substrate. (b) Models for the ρ and λ honeycomb domains. The coloured triangles visualize the orientation of the adsorbates, with corners lying over upwards facing rings of HBC.

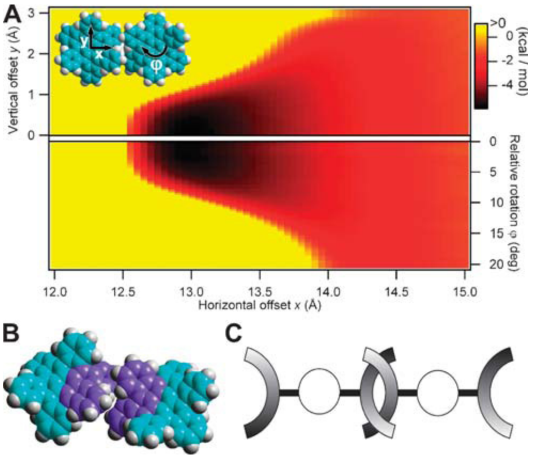

Fig. 3 (a) Interaction energy for two HBC molecules in the interdigitated helical aromatic units recognition geometry as a function of relative position and orientation. The upper/lower halves of the plot are relative to the left/right axes, respectively. The color scale shows the interaction energy in kcal mol^{-1}, with yellow corresponding to repulsive interaction. (b) Coupling motif driving supramolecular organization: Self-complementary helical aromatic units (violet) interdigitate and lock in place by aromatic interactions. (c) Schematic representation of the helical aromatic coupling unit and its incorporation in arbitrary supramolecular structures.

It can be seen that the lateral distance and respective orientation of nearest neighbors is identical in all three different structures, proving that they rely on the same lateral binding motif. Unlike the linear structures that grow from step edges, honeycomb networks are found at the centre of substrate terraces and do not extend up to the step edges surrounding these terraces. The honeycomb structures are more frequently observed than their linear counterparts. Apart from molecules decorating substrate defect sites (*e.g.* step edges) no individual molecules are found on the terraces, indicating a high molecular mobility at the deposition temperature.

The interaction energy of two HBC molecules in the interdigitated helical aromatic units recognition geometry has been computed as a function of relative molecular position and orientation by molecular mechanics calculations (see Fig. 3a).§ The color plot visualizes the shallow potential minimum for displacements along the coupling direction (*x*-axis) and the directionality of the coupling motif. It can be seen that due to steric hindrance between shifted (left axis) or rotated (right axis) helical units, lateral out-of-registry displacements and rotations are limited to less than 1 Å and a few degrees, respectively. Steric hindrance between hydrogen atoms of neighbouring adsorbates bestows to this coupling motif a strong orientational stability beyond the one expected for aromatic interactions between completely planar aromatic systems. The absolute minimum of the interaction potential is located at a center-to-center distance of 13.0 Å (at 0° relative rotation) which compares well with the experimentally observed distance of 13.3 Å (for both honeycombs and chains).

This shallow interaction potential will allow for a commensurate registry with various substrates as the energetic cost for variations in bonding distance is low. This is in line with the well-known versatility of aromatic interactions compared to stronger noncovalent bonds, which allows for a large range of energetically favorable bond lengths and angles as inferred for example by studies on aromatic interactions in proteins.[11]

The effective contact surface of the interdigitated tetrahelicene units is small compared to systems with strongly interdigitating units such as alkyl chains that are frequently used to stabilize solution-based 2D supramolecular architectures.[12] However, molecules containing several long alkyl chains can often not be sublimated intact, preventing studies under UHV conditions. The coupling motif which is here used for two-dimensional architectures might in principle also be applied for supramolecular architectures in three dimensions. However, in the absence of geometrical constraints, the interlocked helical units geometry might not be energetically favoured over other geometries in which the total overlap of aromatic subunits is maximized.

The possibility of small adsorption-induced conformational changes has also been investigated with molecular mechanics simulations. Changes in conformation would involve a collective upwards/downwards bending of the outermost molecular units. This would imply a change in the bending angle of the acene units. Calculations show that no important conformational changes can be expected in the adsorbed state since changes in bending angle by more than approximately 4° result in a significant increase in strain energy. The aromatic interaction between nearest neighbors has also been calculated for these conformations. Both the shape and total energy of the interaction potential remain unaffected by small conformational changes. This shows that the binding motif (Fig. 3b) is inherently rigid and remains unaffected by possible small adsorption-induced conformational changes, which is important as the conformation of large molecules in the adsorbed state is difficult to predict. Previous studies on the self-assembly of rubrene and calix[4]arenes on single crystal surfaces[13] have shown that aromatic interactions can play a major role in stabilizing two-dimensional supramolecular structures on single crystal surfaces. However, the conformational flexibility of the aromatic units of these molecules hinders the prediction of supramolecular structures of such molecules on different substrates, preventing a clear isolation of the coupling motifs. The inherently rigid aromatic coupling motif presented in this *communication* overcomes this problem, making aromatically bonded supramolecular structures more predictable. This coupling motif is not limited to work only on Cu(111) but should also be applicable to any other substrates on which adsorbate–substrate interactions only exhibit a weak lateral modulation.

In this work we have shown—using a non-planar PAH which incorporates self-complementary helical aromatic units—that surface-supported two-dimensional supramolecular architectures can be realized through lateral aromatic interactions. Interdigitated helical aromatic coupling motifs may be used with other molecular building blocks to grow tailor-made structures with overlapping π-electron systems (see schematic model in Fig. 3c). The aromatic interactions' ability to relax to characteristic substrate distances, combined with a careful patterning of the substrate surface presents a means to tailor structures for molecular electronics applications.

Financial support from the NCCR "Nanoscale Science" is gratefully acknowledged.

Notes and references

‡ STM images have been analyzed and processed using the freely available WSXM software.[9]

§ The molecular conformation of isolated molecules in the gas phase has been determined at the AM1 level of theory. Molecular mechanics calculations have been performed using the CHARMM22 forcefield. This forcefield has been found to correctly reproduce aromatic binding for the benzene dimer.[10] A simpler model for aromatic interactions has been developed by Hunter.[11] The nearest neighbour geometry in our work is found to be attractive also with this model.

1 C. Joachim, J. K. Gimzewski and A. Aviram, *Nature*, 2000, **408**, 541.

2 M. E. Cañas-Ventura, W. Xiao, D. Wasserfallen, K. Müllen, H. Brune, J. V. Barth and R. Fasel, *Angew. Chem., Int. Ed.*, 2007, **46**, 1814.

3 (*a*) W. Pisula, M. Kastler, D. Wasserfallen, M. Mondeshki, J. Piris, I. Schnell and K. Müllen, *Chem. Mater.*, 2006, **18**, 3634; (*b*) H. Klauk, M. Halik, U. Zschieschang, G. Schmid and W. Radlik, *J. Appl. Phys.*, 2002, **92**, 5259.

4 (*a*) J. A. Theobald, N. S. Oxtoby, M. A. Phillips, N. R. Champness and P. H. Beton, *Nature*, 2003, **424**, 1029; (*b*) R. Otero, M. Schöck, L. M. Molina, E. Laegsgaard, I. Stensgaard, B. Hammer and F. Besenbacher, *Angew. Chem., Int. Ed.*, 2005, **44**, 2270; (*c*) S. Clair, S. Pons, A. P. Seitsonen, H. Brune, K. Kern and J. V. Barth, *J. Phys. Chem. B*, 2004, **108**, 19392.

5 (*a*) S. Stepanow, M. Lingenfelder, A. Dmitriev, H. Spillmann, E. Delvigne, N. Lin, X. Deng, C. Cai, J. V. Barth and K. Kern, *Nat. Mater.*, 2004, **3**, 229; (*b*) T. Classen, G. Fratesi, G. Costantini, S. Fabris, F. L. Stadler, C. Kim, S. de Gironcoli, S. Baroni and K. Kern, *Angew. Chem., Int. Ed.*, 2005, **44**, 6142.

6 S. Xiao, M. Myers, Q. Miao, S. Sanaur, K. Pang, M. L. Steigerwald and C. Nuckolls, *Angew. Chem., Int. Ed.*, 2005, **44**, 7390.

7 (*a*) J. Lagoute, K. Kanisawa and S. Fölsch, *Phys. Rev. B: Condens. Matter Mater. Phys.*, 2004, **70**, 245415; (*b*) P. Ruffieux, O. Gröning, R. Fasel, M. Kastler, D. Wasserfallen, K. Müllen and P. Gröning, *J. Phys. Chem. B*, 2006, **110**, 11253; (*c*) L. Gross, F. Moresco, P. Ruffieux, A. Gourdon, C. Joachim and K.-H. Rieder, *Phys. Rev. B: Condens. Matter Mater. Phys.*, 2005, **71**, 165428.

8 J. L. Brédas, J. P. Calbert, D. A. da Silvo Filho and J. Cornil, *Proc. Natl. Acad. Sci. U. S. A.*, 2002, **99**, 5804.

9 I. Horcas, R. Fernandez, J. M. Gomez-Rodriguez, J. Colchero, J. Gomez-Herrero and A. M. Baro, *Rev. Sci. Instrum.*, 2007, **78**, 013705.

10 A. T. Macias and A. D. MacKerell, *J. Comput. Chem.*, 2005, **26**, 1452.

11 C. A. Hunter, *Chem. Soc. Rev.*, 1994, **23**, 101.

12 (*a*) D. Bléger, D. Kreher, F. Mathevet, A.-J. Attias, G. Schull, A. Huard, L. Douillard, C. Fiorini-Debuischert and F. Charra, *Angew. Chem., Int. Ed.*, 2007, **46**, 7404; (*b*) K. Tahara, C. A. Johnson II, T. Fujita, M. Sonoda, F. C. De Schryver, S. De Feyter, M. M. Haley and Y. Tobe, *Langmuir*, 2007, **23**, 10190.

13 (*a*) M.-C. Blüm, E. Cavar, M. Pivetta, F. Patthey and W.-D. Schneider, *Angew. Chem., Int. Ed.*, 2005, **44**, 5334; (*b*) M. Pivetta, M.-C. Blüm, F. Patthey and W.-D. Schneider, *Angew. Chem., Int. Ed.*, 2008, **47**, 1076; (*c*) V. A. Langlais, Y. Gauthier, H. Blekhir and O. Maresca, *Phys. Rev. B: Condens. Matter Mater. Phys.*, 2005, **72**, 085444.

Supporting information for

An Aromatic Coupling Motif for Two-Dimensional Supramolecular Architectures

Matthias Treier, Pascal Ruffieux, Pierangelo Gröning, Shengxiong Xiao,
Colin Nuckolls, Roman Fasel

Self-assembly of HBC on Cu(111)

The preferential adsorption sites for hexa-*cata*-hexabenzocoronene (HBC) on Cu(111) are step edges of the underlying substrate. Only once the step edges are completely decorated with adsorbates, supramolecular structures can be found on the terraces. No individual molecules are found on the terraces. While linear structures can grow out from step edges, extended honeycomb networks are exclusively formed away from the steps on the terraces. Domain sizes vary considerably between neighbouring islands (Figure 18) but can easily extend up to 10-15 honeycombs in each direction.

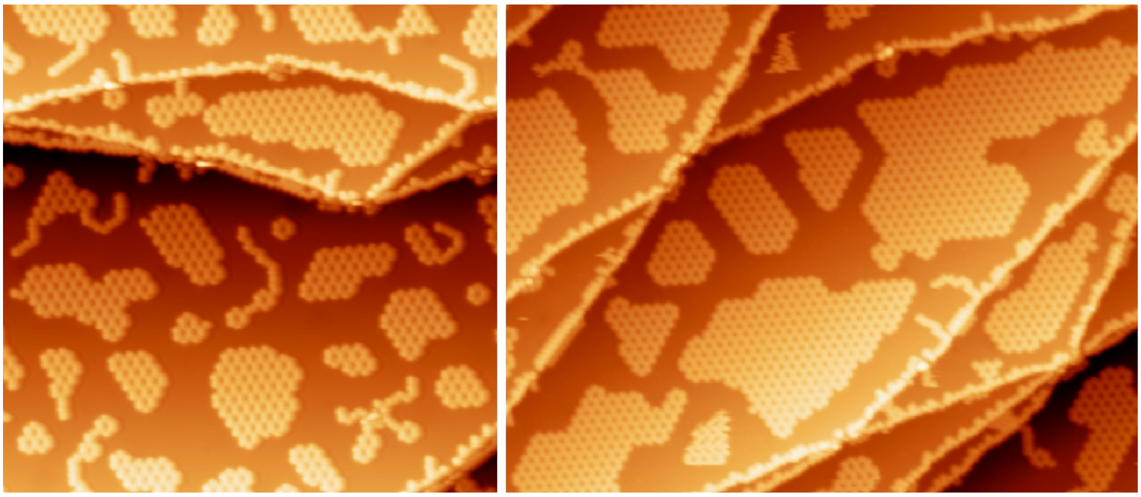

Figure 18: Overview STM images of contorted HBC on Cu(111). Parameters: 93 nm x 93 nm, -2 V, 20 pA, 5 K (left); 131 nm x 101 nm, -2 V, 10 pA, 77 K (right).

Tetrahelicene units of HBC

Hexa-*cata*-hexabenzocoronene can be regarded as three fused tetrahelicene units (Figure 19). The definition of these helical units is shown in Figure 19. Starting from a given peripheral carbon ring, two mirror-symmetric tetrahelicene units can be drawn by passing around the central coronene core to the neighbouring peripheral ring to the left or to the right. Following the nomenclature for the enantiomers of heptahelicene, these units are designated as M- and P-tetrahelicene. The HBC molecule can thus be regarded as consisting of either three fused M-tetrahelicene or three fused P-tetrahelicene units (Figure 19). Both descriptions are of course equivalent, and the HBC molecule itself is achiral. Lateral coupling of two HBCs, however, is only possible via two P- or via two M-tetrahelicene units, such that upwards-/downwards-facing neighbouring aromatic rings on one molecule point towards a downwards-/upwards-facing pair of rings of the neighbouring molecule (see bottom Part of Figure 19).

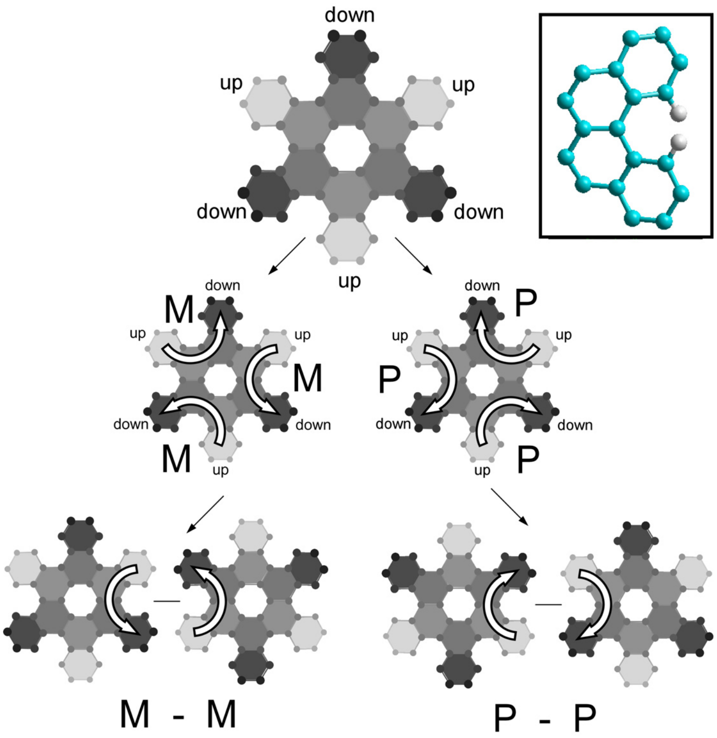

Figure 19: Definition of the helical subunits of HBC. Two helical tetrahelicene units of opposite chirality can be defined starting from every peripheral 6-membered ring. The greyscale colouring of the carbon atoms and the benzene rings visualizes the relative heights with dark units pointing "down". Lateral aromatic coupling is only possible via P-P or M-M tetrahelicene units. *Inset:* Schematic representation of a tetrahelicene unit. Only the hydrogen atoms responsible for nonplanarity (due to steric hindrance) are shown for visibility.

Stability of the interdigitated helical aromatic units coupling motif

Depending on the tunneling parameters and the state of the tip apex, a displacement of molecular units comprising several molecules can be induced by scanning repeatedly over a given supramolecular structure. An example of such a tip-induced movement of an intact poly-molecular structure is shown in Figure 20 where the three terminal molecules of an initially linear structure have been displaced between consecutive STM images. The intramolecular coupling is hence strong enough for entities comprising several molecules to be moved intactly.

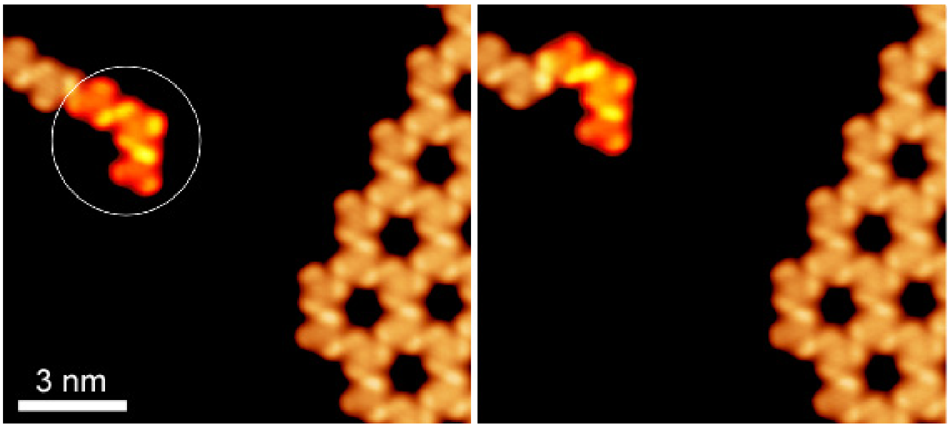

Figure 20: Consecutive STM images (-1.8V, 50pA) of the same region showing the intact displacement of a supramolecular unit (circle; highlighted in yellow-red).

4.3 Further aspects and outlook

The successful demonstration of aromatic coupling motifs as building blocks in two-dimensional supramolecular systems opens the way to a new class of surface-supported organic architectures. While a rational design of two-dimensional networks based on hydrogen-bonds [*22, 26, 27*] and metal-coordination [28, 158, 159] is now routinely achieved, the use of rationally designed lateral aromatic interactions is new to the field of two-dimensional supramolecular chemistry. All three types of interactions can be used in potential supramolecular networks that might serve as nanoscale templates.

In order to extend the ‘library’ of aromatic coupling motifs for supramolecular architectures, the use of self-complementary helical aromatic units different from the tetrahelicenes in cHBC has been investigated. Within the same class of helical aromatic structures, only pentahelicene units are expected to be efficient candidates for interdigitation. Smaller helical units, e.g. a potential trihelicene (i.e. a phenanthrene) are completely planar since there is no steric hindrance between hydrogen atoms in the bay region. Interdigitation in hexahelicene or even larger helicenes is limited due to an increased steric hindrance preventing an efficient overlap – which is the main contribution to the interaction energy – between aromatic units. Apart from helicene units, other types of spiral aromatics [160] might also be used as aromatic coupling motifs in two dimensions.

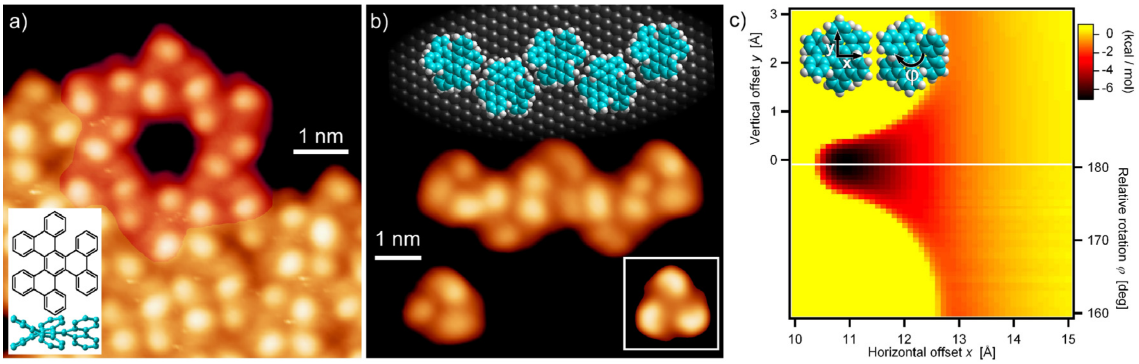

Figure 21: HBTP on Cu(111) (a) Honeycomb consisting of 6 HBTP based on interdigitated pentahelicene coupling motifs (highlighted in red), on the border of a more densely packed phase. (-1.7 V, 10 pA) The inset shows the chemical structure of the strongly distorted polyaromatic board of HBTP. Hydrogen atoms are omitted in the side-view for clarity. (b) Linear HBTP unit consisting of five molecules and corresponding molecular model. A single HBTP is seen at the lower left. The inset shows a simulated STM image for a single HBTP. (-1.8 V, 10 pA) (c) Interaction energy – computed with CHARMM22 [123] – of two homochiral HBTP in the interdigitated helical units recognition geometry as a function of relative position and orientation.

The bay regions of hexabenzotriphenylene[4] [161] (HBTP, see inset in Figure 21a) consist of pentahelicene units, making the molecule an ideal test candidate for the usability of interdigitated aromatic pentahelicene coupling motifs. Steric hindrance in the pentahelicene units is stronger than in the corresponding tetrahelicenes, leading to a strongly nonplanar geometry of HBTP [162]. Unlike cHBC, HBTP is chiral and each enantiomer only contains either M- or P-pentahelicene units.

Figure 21 shows self-assembled structures of HBTP on Cu(111) after deposition from resistively heated quartz crucibles with the sample held at room temperature. Most molecules assemble into a densely packed phase (bottom part of Figure 21a), which is stabilized by several different lateral aromatic interaction motifs. However, linear and honeycomb structures assigned to interdigitated pentahelicene coupling motifs can also be found, showing that pentahelicene units can couple in a way similar to tetrahelicene. As for cHBC, the lateral interaction has been quantified by force-field calculations using CHARMM22 [123]. Figure 21c shows the interaction energy between two HBTP of same chirality in the interdigitated helical units recognition geometry as a function of relative position and orientation. Compared to the corresponding interaction energy potential for cHBC, it is seen that the lateral and angular flexibility of the pentahelicenes is smaller compared to interdigitated

---

[4] The complete name of HBTP is hexabenzo[a,c,g,i,m,o]triphenylene. This compound has however also been referred to as dibenzo[f,j]phenanthro[9,10-s]picene.

tetrahelicenes. This is mainly due to stronger steric hindrance between hydrogen atoms of the two molecules. The maximum binding energy (7.0 kcal/mol) is higher than for the tetrahelicenes (5.8 kcal/mol), which is due to the larger area overlap between the outermost benzene ring that is possible due to the stronger nonplanarity of HBTP. It should be noted that apart from this interdigitated coupling motif between identical enantiomers of HBTP, interdigitated interaction geometries between opposite enantiomers are also possible. The phenanthrene unit of one enantiomer can interdigitate with the pentahelicene of the opposite enantiomer. This type of interdigitated geometry is – among other lateral aromatic interactions – present in the densely packed structures

The experimentally determined nearest neighbour distance of 1.2 ± 0.1 nm approximately corresponds to 5 nearest neighbour distances of the substrate (1.26 nm), suggesting that commensurate superstructures might also be created using this pentahelicene coupling motif. Individual adsorbates, which are sometimes observed on terraces, seem to be distorted/adsorbed in a nonplanar way as can be seen by the different apparent heights of the three protrusions centred over the upwards-pointing units of HBTP (Figure 21b). This difference in apparent height is also observed for molecules bound within linear structures. However, the lateral aromatic coupling does not appear to be affected by this distortion, further proving that – like self-complementary interdigitating tetrahelicene units – self-complementary pentahelicenes might be used as a design feature for rationally designed supramolecular architectures in two dimensions.

A first proof-of-principle of such a rationally designed architecture is shown in Figure 22. The large nonplanar PAH OBC contains both tetra- and pentahelicene units and can hence be schematically looked at as a rectangular building block with two types of aromatic coupling motifs on opposing sides (Figure 22a). On Cu(110), OBC forms close-packed islands (Figure 22b) whose structure agrees well with a model based on self-complementary interdigitating helical aromatic units (Figure 22c).

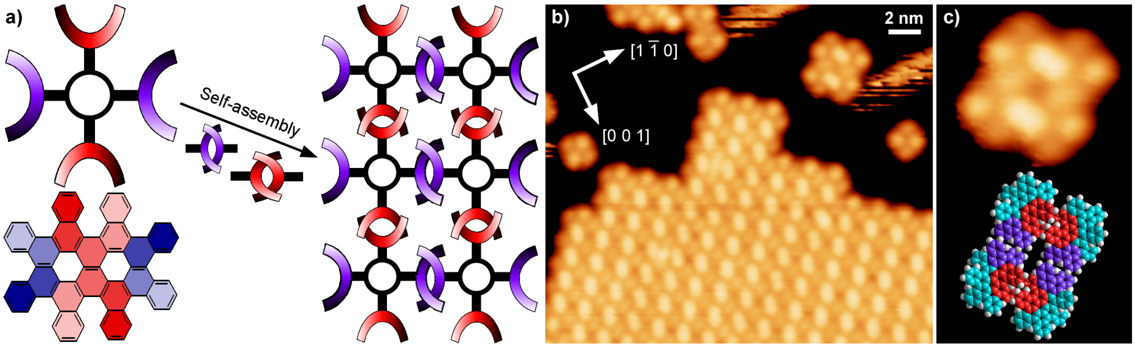

Figure 22: Rational design of supramolecular architectures using interdigitating aromatic coupling motifs. (a) Schematic model of designed rectangular supramolecular network based on a rectangular building block containing two types of aromatic coupling motifs. OBC (bottom left) contains pentahelicene (red) and tetrahelicene (blue) units. (b) STM image (1.2 V, 20 pA) of submonolayer of OBC on Cu(110). (c) Cluster of four OBC molecules on Cu(110) and proposed molecular model.

A major advantage of aromatic coupling motifs compared to other noncovalent bonds is that potential charge carrier pathways within the plane of the network are created due to partial overlap between π-orbitals of neighbouring molecules within the interdigitated units. Theoretical modelling at the semi-empirical level using AM1 has been performed to assess the potential charge carrier mobilities of such systems.

Charge transport in organic semiconductors can be described by an incoherent hopping model [163] in which charge can only be transferred between adjacent molecules. Each hopping event is treated as a non-adiabatic electron-transfer reaction and Marcus theory [164, 165] is used to express the hopping rate W between nearest neighbours as a function of the reorganization energy λ and the electronic coupling matrix M_{AB} which is dictated mainly by the orbital overlap [166]:

$$W = \frac{M_{AB}^2}{\hbar}\left(\frac{\pi}{\lambda k_B T}\right)^{1/2} \exp\left(-\frac{\lambda}{4k_B T}\right) \tag{12}$$

from which the diffusion coefficient D of the charge carriers follows as:

$$D = \frac{1}{2n} L^2 W \tag{13}$$

where n=3 is the dimensionality and L is the effective length associated with the hopping event. Using the Einstein relation [167], the drift mobility of hopping μ is then given by

$$\mu = \frac{e}{k_B T} D = \frac{1 e L^2 W}{6 k_B T} \tag{14}$$

The coupling matrix element M_{AB} of a given energetic level can be approximated – within the Marcus-Hush theory [164, 165, 168, 169] – by the splitting of that level in the dimer compared to the isolated neutral molecule. For organic systems, this means that the hole/electron mobilities will depend on the splitting of the HOMO/LUMO level.

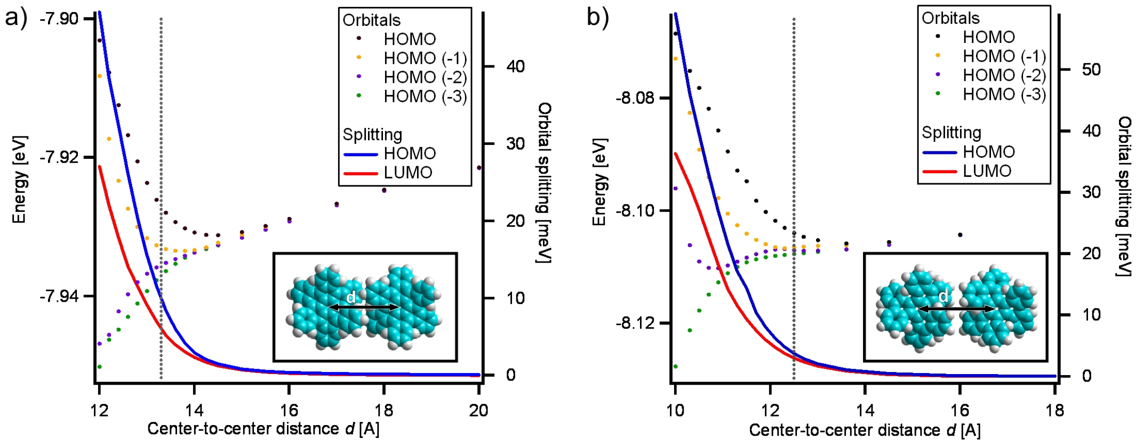

Figure 23: Orbital energy splittings for interdigitated helical aromatic units computed with AM1. (a) HOMO energies and relative splitting of the HOMO and LUMO as a function of nearest neighbour distance between two cHBC in the interdigitated helical units recognition geometry. (b) Corresponding diagram for HBTP. Dashed lines indicate the experimentally observed nearest neighbour distances. Both cHBC and HBTP have doubly degenerate HOMO and LUMO levels.

Figure 23 shows the relative splitting of the HOMO / LUMO levels of cHBC and HBTP in the interdigitated helical aromatics recognition geometry as a function of intramolecular distance. The order of magnitude of the computed splittings is in agreement with splittings computed with other methods for various organic semiconductors [166, 170-172]. The splitting of the LUMO is smaller than the splitting of the HOMO for both types of molecules, which is in agreement with the generally observed tendency for π-conjugated organic semiconductors that hole mobility is higher than electron mobility [173]. At the experimentally observed intermolecular distances, a HOMO-splitting of 10 meV (cHBC) respectively 4 meV (HBTP) is obtained. In the case of HBTP the nearest neighbour distance of 12.6 Å on Cu(111) is significantly larger than the minimum obtained with the force-field simulation (Figure 21c) which is located at 11.0 Å. It might hence be possible to obtain a larger HOMO-splitting on substrates where the nearest neighbour distance is closer to the computed minimum. At 11.0 Å a HOMO-splitting of 24 meV is obtained for HBTP.

In order to quantitatively predict possible charge carrier mobilities in these systems, the computed results are “normalized” by comparison of the computed splittings of a reference organic semiconductor with the values obtained for cHBC. By using a reference substance rather than directly computing charge carrier mobilities, under-/overestimating of the mobilities due to an under-/overestimation of the splitting (inherent to the computational method) is avoided. Pentacene has been chosen as a reference since it is probably the most widely studied conjugated organic semiconductor. The reason for this is that properties of pentacene-based organic thin film transistors are among the best for organic semiconductors [15, 174] with mobilities on the order of 3-5 $cm^2V^{-1}s^{-1}$ [175, 176] being routinely achieved. Exceptionally high mobilities of 35 $cm^2V^{-1}s^{-1}$ at room temperature have also been reported [177] even though theoretical simulations have suggested an upper limit of about

5.4 $cm^2V^{-1}s^{-1}$ for hole mobility in pentacene crystals [172]. A HOMO splitting of 200 meV is computed for pentacene with AM1 based on the nearest neighbour geometry in the crystal structure [178]. This value is about 20 times larger than the corresponding splitting for cHBC, resulting in a reduction of the hopping rate by a factor of about 400 (eq. 12). However, the hopping distance L in pentacene is only 4.7 Å compared to 13.3 Å, resulting in an increase by a factor of about eight of the diffusion coefficient (eq. 13). Using equation (14) and the above-mentioned quantities, the hole mobility within two-dimensional cHBC structures is hence estimated to be about 50 times smaller than for pentacene single crystals, i.e. on the order of 0.1 $cm^2V^{-1}s^{-1}$. While this value might appear small at first sight, it has to be emphasized that it is very large for a truly two-dimensional system where the lateral overlap between aromatic units is inherently smaller than in a three-dimensional crystal.

The reorganization energy of pentacene and cHBC have not been considered within this framework, however, the reorganization energy of cHBC can be expected to be smaller than the corresponding value for pentacene, as λ has been shown to decrease with increasing size of PAHs [172]. Since the hopping rate W increases with decreasing λ (eq. 12) an even higher mobility might be theoretically possible.

Transport measurements will be needed to experimentally demonstrate the theoretically suggested electronic coupling between interdigitated helical aromatic units. The honeycomb phase of cHBC on Cu(111) is the most promising superstructure for such measurements which can however not be performed on the conducting Cu(111) substrate. Transport measurements might however be possible on chemically inert substrates based on semiconductors, such as e.g. silver terminated Si(111) [179] on which supramolecular architectures have been constructed successfully [26, 180, 181].

5 Self-assembly guided by subtle energy balances

5.1 Introduction

While many approaches towards surface-supported organic supramolecular nanostructures have used specifically designed, complementary molecular units to steer the self-assembly [*22*], it is shown in this chapter, that rather than designing perfectly complementary molecular units, the design of complementary units whose homo- and heteromolecular interaction energies are such that intermixing and phase-separation are competing, results in a rich variety of structures that can be tuned by coverage and stoichiometry.

The formation of nanostructures of different dimensionality, formed by self-assembly of a bi-molecular mixture between the organic semiconductor PTCDA and an amine-containing hydrogen bonding spacer molecule on Au(111) have been investigated by STM.

Intermixing between co-adsorbates has been reported before [182] including several studies with PTCDA [183-185]. However, the structures reported in these studies rather correspond to two-dimensional lattices, where PTCDA is included in a bi-molecular superlattice rather than intermixing limited phase separation. The intermixing of co-adsorbates reported in this chapter on the other hand is different from the earlier studies since nano-units of PTCDA with ordering similar to monolayer phases [186] are intermixed with hydrogen bonding spacers.

The concept reported in this chapter (Figure 24) is probably the closest to self-assembly processes in nature, where the formation of large-scale ordered structures only depends on relative interaction energies and dynamics of competing interactions (which – in two dimensions – depend on coverage and temperature). In principle, there is no upper size limit for the PTCDA structures created by this approach since the size of the self-assembled PTCDA nanostructures should ultimately only depend on the concentration of hydrogen bonding spacers.

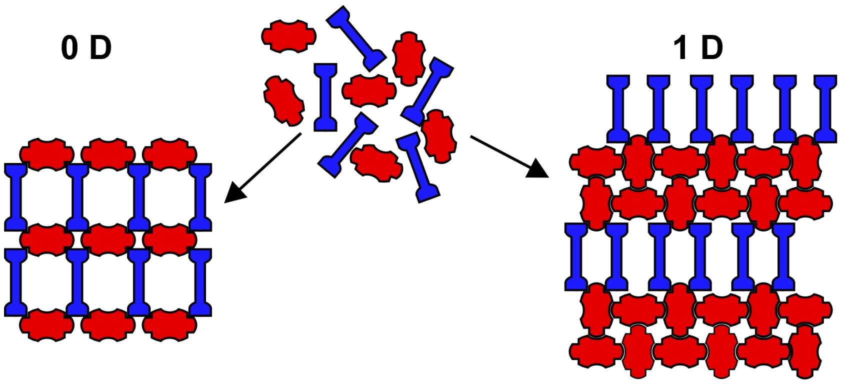

Figure 24: Schematic illustration of the concept of formation of nanostructures of a given species (red), capable of forming both homo- and heteromolecular hydrogen bonds, using hydrogen bonding spacers (blue). Both adsorbates are deposited on a substrate (middle) where they form ordered structures of different type (e.g. zero- or one-dimensional) that can be tuned by external factors such as stoichiometry, coverage or shape of the spacer molecule.

5.2 Tailoring low-dimensional organic semiconductor nanostructures

Matthias Treier[1], Manh-Thuong Nguyen[1], Neville V. Richardson[2], Carlo Pignedoli[1], Daniele Passerone[1], Roman Fasel[1]

[1] Empa, Swiss Federal Laboratories for Materials Testing and Research,
nanotech@surfaces laboratory, 3602 Thun and 8600 Dübendorf, Switzerland
[2] EaStCHEM, School of Chemistry, University of St. Andrews, St. Andrews KY16 9ST,
United Kingdom

Nano Letters **9**, 126-131 (2009)

Abstract

The quest for miniaturization of organic nanostructures is fuelled by their possible applications in future nanoscale electronic devices. Here we show how a range of nanostructures of reduced dimensionality of the organic semiconductor PTCDA can be realized on Au(111) by intermixing the latter with hydrogen bonding spacer molecules. The purpose of the spacers is to separate nano-units of pure PTCDA, using hydrogen bonds between the anhydride end of PTCDA and amine groups of the spacers. A highly regular array of potential quantum dots can be realized by this approach.

Organic semiconductors are set to play a key role in future nanoelectronic devices [*9, 10*] due to their extensively tuneable electronic properties. Besides readily commercially implemented applications of thin organic films in solar cells and photosensors [*16*], organic light emitting diodes [*14*] and transistors [*15*], future devices are also expected to exploit functionalities of single molecules [187] and/or small molecular clusters with tailored chemical and electronic properties. A key issue with regard to possible applications of organic semiconductor nanostructures is therefore the ability to create highly ordered arrays of nanostructures of well-defined size and shape which can then be integrated into a functional device. Apart from the inherent electronic properties – such as for example the HOMO-LUMO gap – of a given organic semiconductor, which can be tuned by appropriate chemical functionalization, the geometric properties of semiconductor nanostructures present an additional means for tailoring the electronic properties. It has, for example, been shown that a free-electron like, two-dimensional band state confined to 3,4,9,10-perylenetetracarboxylic dianhydride (PTCDA) islands is formed at the interface of PTCDA with Ag(111) [188]. Metal-induced interface gap states for the same molecule have also been suggested for adsorption on Au(111) [189]. Similar interface states have been found for pentacene, another widely studied organic semiconductor, on Cu(110) [190]. It is hence desirable to find ways to produce regular arrays of monodispersed nanostructures of such organic semiconductors in order to be able to exploit the unique electronic properties of these confined interface states.

Hydrogen-bonded supramolecular architectures have been realized on single-crystal metal surfaces using various molecules [22, 26, 27, 191], allowing for the creation of hydrogen-bonded supramolecular networks with a wide range of symmetries and geometric properties. However, these previous studies have focused mainly on the possibilities of obtaining ordered networks by the use of chemically complementary building blocks rather than using hydrogen bonds to stabilise nanostructures of one molecular species embedded in a matrix of the second species, i.e. to achieve a partial but well-defined nanoscale phase separation. We demonstrate that, by an appropriate choice of complementary functional groups capable of forming hydrogen bonds, systems where partial intermixing of two adsorbates is favoured over complete phase separation can be created. Using scanning tunneling microscopy (STM), we show that using hydrogen bonds of intermediate strength, it is possible to grow a range of different nanostructures of the prototype organic semiconductor PTCDA that are separated by hydrogen-bonded spacer molecules. We report on zero- (0D) and one-dimensional (1D) PTCDA nanostructures self-assembled on Au(111) by intermixing with the amine-functionalized co-adsorbates 4,4''-diamino-p-terphenyl (DATP) and 2,4,6-tris(4-aminophenyl)-1,3,5-triazine (TAPT) studied by STM. Density functional theory (DFT) calculations show that it is the subtle energy balance between homo- and heteromolecular interactions that drives the formation of these regular self-assembled arrays of organic nanostructures of reduced dimensionality. Our results suggest that the embedding of a molecular species in a matrix of hydrogen-bonding spacer molecules can be used as a general conceptual approach towards the fabrication of low-dimensional organic semiconductor nanostructures.

Experiments have been performed in an ultra high vacuum system (base pressure $1\cdot10^{-10}$ mbar) using an Omicron low-temperature STM operated at 77K. The Au(111) single crystal substrate was cleaned prior to deposition of the molecules by standard sputtering-annealing cycles. PTCDA (97% purity, Fluka), DATP (95% purity, ABCR) and TAPT (see Figure 25a for chemical structures) were deposited sequentially from resistively heated quartz crucibles held at 510, 380 and 470 K respectively at deposition rates of approximately 0.2 ML/min. During deposition of the molecules the sample was kept at room temperature (RT). The samples with PTCDA and DATP were annealed to 370 K for 10 minutes after deposition in order to desorb impurities stemming from the DATP source material, facilitating the STM analysis. Samples containing TAPT and PTCDA were transferred directly to the STM without annealing. STM images have been processed using the WSxM software [192].

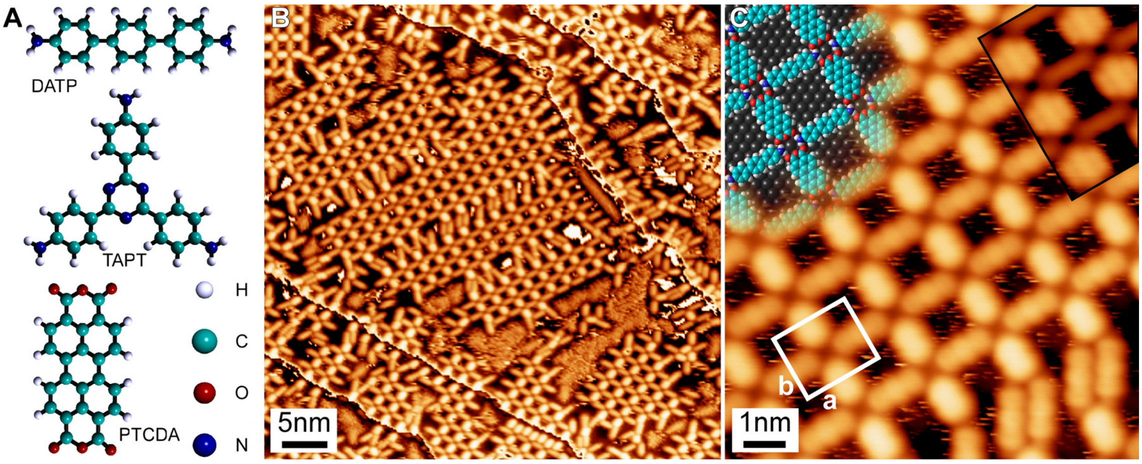

Figure 25: (A) Chemical structures of molecules used in this study. (B&C) Hydrogen-bonded rectangular superstructure between PTCDA and DATP on Au(111). (B) Overview STM image showing all three rotational domains. Contrast has been applied to each terrace individually. (V=-1.0V; 20pA). (C) High-resolution image and model of the rectangular superstructure. (V=-1.8V, 20pA). The boxed part at the upper right has been measured with opposite bias, showing the characteristic intramolecular contrast of PTCDA on Au(111) (V=+0.5V, 20pA).

Density Functional Theory (DFT) using the B3LYP hybrid functional [193, 194] was employed for calculations of binding energies of molecular dimers. In order to accurately describe properties of the hydrogen-bonds of the systems, the valence triple zeta basis set augmented with d- and p-like polarization functions 6-311 G(d, p) [195] was chosen. The energies of periodic systems have been computed using plane wave calculations using the q-Espresso code. Extensive details on all DFT calculations can be found in the supporting information.

Submonolayers of PTCDA deposited together with DATP form an open rectangular hydrogen-bonded network with a 1:1 stoichiometry as shown in Figure 25. These networks can also be regarded as arrays of regularly spaced and identically oriented PTCDA. The long axis of PTCDA is aligned with the <110> directions of the substrate and the long axis of DATP lies along the <211> directions and orthogonal to PTCDA within each domain. The unit cell (Figure 25c) has dimensions a = 1.95 ± 0.05nm; b = 1.7 ± 0.05nm, corresponding within the errors to a commensurate (6x4√3)rect structure.

The networks are stabilized by 4 NH···O hydrogen bonds per unit cell. There are only three equivalent rotational domains proving that the superlattice must be rectangular as an oblique lattice would result in at least six rotational/reflectional domains due to matching with the C_{3v} substrate symmetry. Networks are always terminated by DATP molecules even if the local coverage of PTCDA is higher than that of DATP. Excess PTCDA will simply form pure PTCDA islands. The size and quality of the networks cannot be improved significantly by further annealing up to 450 K. Neighbouring network domains are often interconnected by double rows of DATP (Figure 25b&c) or similar hydrogen-bonding patterns of DATP. These geometries allow for bifurcated hydrogen bonds between DATP and PTCDA (see supporting information).

Surface-supported supramolecular structures based on hydrogen bonds between molecules containing amine and anhydride functional groups have been reported for different molecules on a silver terminated Si(111) surface [26, 196, 197]. Unlike those previously reported PTCDA structures, the superstructures presented herein depend crucially on both homo- and heteromolecular interactions. The computed interaction energy per PTCDA molecule within the PTCDA herringbone phase is 0.44 eV compared to 0.87 eV per PTCDA in the binary rectangular PTCDA-DATP superstructure (see supporting information). Intermixing of PTCDA and DATP will hence be favoured over a phase separation because it lowers the overall energy of the system. DATP cannot form strong homomolecular hydrogen bonds due to the absence of hydrogen bond acceptor units. The DATP-DATP interaction energy is dominated by dispersive (Van-der-Waals) contributions which are small compared to the hydrogen bonding energies due to the small contact surface between nearest neighbours, which prevents the formation of ordered DATP structures at submonolayer coverage. Submonolayer structures of non-functionalized polyphenyls on various substrates indicate that the interaction is only very weakly attractive or even repulsive [198, 199]. The DATP-DATP interaction energy being negligible, the intermixing of the two constituents hence maximizes the overall binding energy. PTCDA has four carbonyl oxygens which can form carbonyl-amine hydrogen bonds. Additionally, bifurcated hydrogen bonds between an amine and the carbonyl and bridging oxygens in PTCDA are possible, offering a variety of energetically favourable hydrogen bonding geometries.

At a bias voltage of 0.5V, PTCDA displays intramolecular features (see inset of Figure 25c) identical to the ones reported by Kröger [133] for pure PTCDA islands. In Krögers work, these features were observed only at higher bias voltages (>0.8V) suggesting that the LUMO, which is responsible for this particular contrast, is significantly shifted to lower energies due to the hydrogen-bonding DATP neighbours within the networks.

At higher adsorbate coverage (i.e. at coverages exceeding that required for complete decoration of the substrate with the rectangular phase of Figure 25b), a different type of superstructure can also be observed, as shown in Figure 26. Single- or double-rows of PTCDA are separated by pairs of DATP, which are again aligned along <211> directions. The structures shown in Figure 26 correspond to 2:1, 3:2 and 1:1 ratios of PTCDA:DATP respectively. The structure within the double-rows closely resembles the well known square phase of PTCDA [200], with molecules inside the rows being rotated by ~85°±5° with respect to each other. Within the single rows, nearest neighbours are either in a geometry close to the one found in the square phase or tilted by 70±10° with respect to each other. The double strands are not completely straight but contain kinks (denoted by arrows in Figure 26) every 2-8 molecules. The DATP adjacent to these kinks has only three rather than the maximum of four hydrogen bonds with PTCDA. We attribute this apparent reduction in interaction energy to an overall improved registry of the PTCDA rows along the <211> directions of the substrate achieved by the introduction of the kinks. Between neighbouring rows, the location of kinks is correlated as indicted by the series of arrows in Figure 26a.

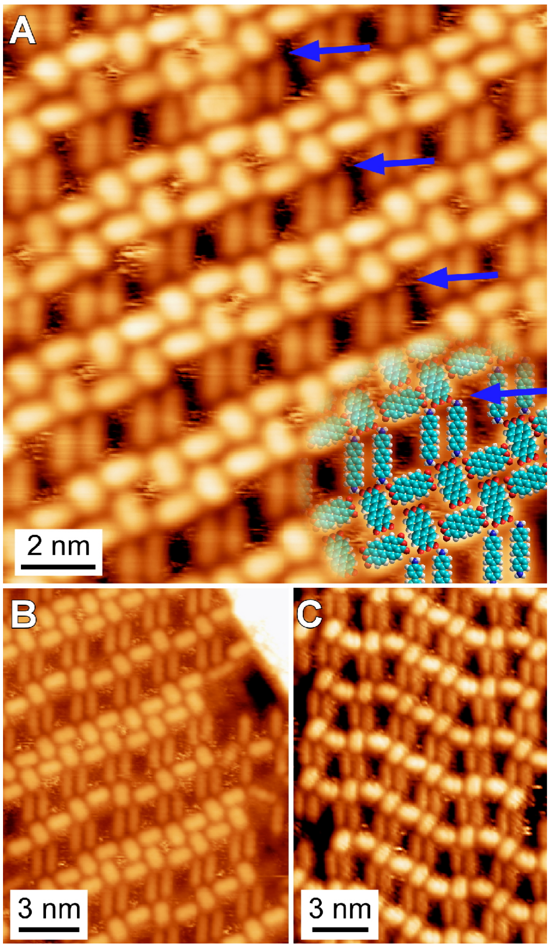

Figure 26: Linear PTCDA nanostructures: (A) Double-row structure with schematic molecular model. Arrows designate kinks along the PTCDA rows. (B) Alternate double-/single-row structure. (C) Single-row structure. Scan parameters: (A) +0.5V, 25pA (B) -0.2V, 50pA (C) -0.5V, 20pA.

The 1D PTCDA row-structures (Figure 26) are observed only at higher coverage, whereas the rectangular 0D PTCDA networks (Figure 25) are also present at submonolayer coverage when the surface is incompletely decorated with adsorbates. The packing density of the 1D structures is higher than that of the rectangular superstructure with the relative density increasing with increasing PTCDA content. This suggests that at a stoichiometry of 1:1, the average interaction energy per PTCDA-DATP pair is higher for the rectangular structure but there is a change to the linear phase at higher coverage because the interaction energy density (per unit area) is higher, although there is a cost in the average energy per PTCDA-DATP pair. This is possible because of the higher packing density of the linear structures, with a unit cell, containing one PTCDA and one DATP molecule, of 3.1±0.3 nm^2 for the linear structure compared with 3.3±0.1 nm^2 for the rectangular structure. The energy difference for the average PTCDA-DATP interaction energy between the two structures must therefore be <7%. The persistence of the rectangular structure at higher coverages we ascribe to kinetic limitations on the phase change.

The DATP dimers are connected to the double-/single-rows (Figure 26) in a way similar to the geometrical arrangement that can be found as linkers between neighbouring rectangular domains, with the two DATP being oriented at ~30° with respect to the adjacent PTCDA molecules (see also Figure 25c). However, when bonding to the PTCDA-rows, hydrogen bonds to two differently oriented PTCDA molecules are present except for DATP lying at a kink. The binding energies for PTCDA within the single-, alternate- and double-row structures are all estimated to be between 0.6-0.8 eV, where the energies are estimated using the hydrogen bonding energies computed for the periodic rectangular superstructure and herringbone PTCDA monolayer (see supporting information). However, hydrogen bond strengths might be different in these geometrical arrangements. On the other hand, this simple estimate supports the tendency for intermixing also at these higher coverages since the energies are between the ones found for the pure PTCDA phase (0.44 eV) and the rectangular superstructure (0.87 eV). It should also be noted that the relative packing density increases when going from single- to double-PTCDA rows with packing densities of the structures shown in Figure 26a & 26b being approximately 4.1±0.3nm^2 (per 1 DATP + 2 PTCDA) and 3.4±0.3nm^2 (per 1DATP + 1.5 PTCDA) respectively.

Figure 27 shows an STM image of the regular PTCDA nano-islands that are formed by co-adsorption with TAPT. The unit cell of this superstructure contains seven PTCDA and four TAPT which represents - to the best of our knowledge - the largest supercell of a self-assembled, bi-component organic supramolecular structure in two dimensions to date. A variation on this superstructure is also observed but less frequently, mostly on borders of large islands of the 7:4 superstructure. In this alternative phase, clusters consisting of three or four PTCDA are surrounded by TAPT (see supporting information). The stoichiometry in these phases can vary considerably from the dominating 7:4 structure, showing that the overall stoichiometry is not crucial for the formation of the ordered nanodot array, since at least small deviations from the optimal stoichiometry can be compensated by the creation of domains with different stoichiometry.

The five central PTCDA molecules show an ordering similar to the one observed in the PTCDA herringbone phase with nearest neighbours at ~80° with respect to each other, while the two outermost molecules are tilted by ~45° with respect to their nearest neighbours; a configuration which has no monolayer analogue.

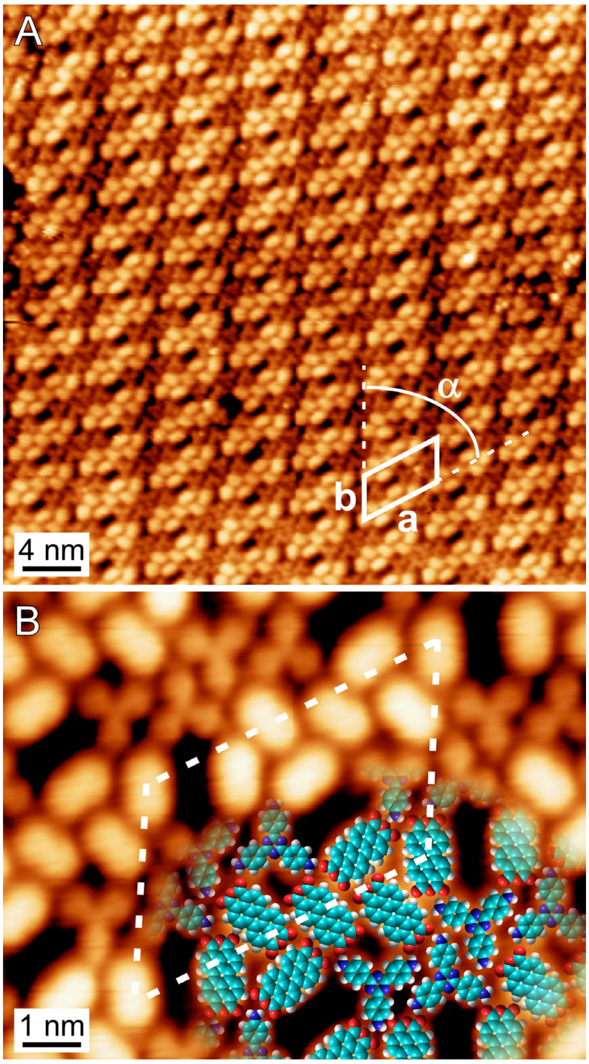

Figure 27: Superlattice of PTCDA nanoislands. Overview (A) and detailed STM image with model (B) of array of seven-molecule PTCDA nanoislands produced using TAPT as a hydrogen bonding spacer. Unit cell dimensions in A: a = 5.5 ± 0.2 nm, b = 3.5 ± 0.2 nm, α = 60° ± 5° with both a and b aligned along <211> directions. Scan parameters: (A) -1.5V, 10pA (B) -0.8V, 50pA.

From the structure determined by STM, we estimate that there are 16 NH···O hydrogen bonds present in each unit cell out of 24 potentially available NH bonding sites. The different types of PTCDA bonding geometries present in these organic nanostructures show that there are several energetically favourable PTCDA-PTCDA interactions in addition to those which are similar to the bulk interactions. Indeed, PTCDA superstructures with different intramolecular spacing and nearest neighbour orientations have been reported for various substrates (*116-118*) experimentally proving the flexibility of the PTCDA-PTCDA interactions. This is supported by B3LYP DFT calculations for different nearest neighbour geometries which turn out to be almost isoenergetic with binding energies of about 0.2 eV (see supporting information). At the same level of theory a binding energy per NH···O hydrogen bond in the rectangular phase (Figure 25b&c) of 0.15 eV is obtained. This indicates that a careful design of the amine functionalized spacer molecules should permit a tailoring of low-dimensional PTCDA nanostructures. Arrays of PTCDA on Au(111) have been created by co-deposition of small amounts of Fe-atoms [201]. However, the approach reported here results in a much sharper size distribution, which is crucial since the geometric shape of the cluster is of importance for their electronic properties. It should also allow greater control over size, shape and separation of the clusters.

Intermixed phases upon co-adsorption of two adsorbates have been reported previously [182-184]. The systems reported here are however different from previous work as the resulting structures are not a true mixing of two molecular species but nanosized islands of the pure phase of one molecule (PTCDA) are incorporated in a matrix of strongly bound spacer molecules (DATP or TAPT).

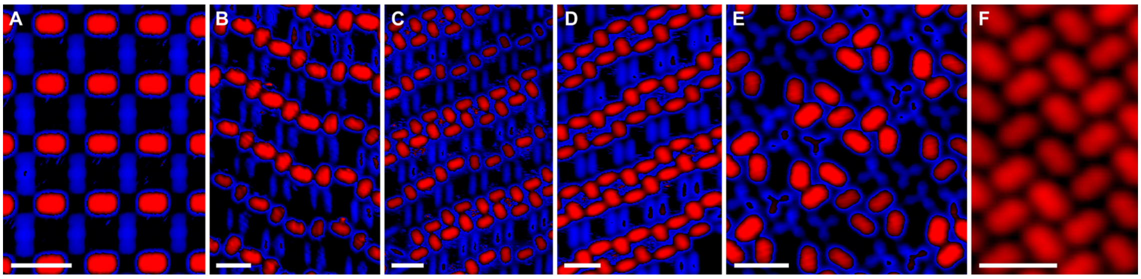

Figure 28: Zero- and one-dimensional PTCDA nanostructures grown on Au(111) using hydrogen bonding spacer molecules. Contrast is set such that PTCDA appears red while the spacers (which have a lower apparent height) are blue. Scale bars are 2nm in each image. (A) Array of equally spaced individual PTCDA molecules stabilized by DATP hydrogen-bonding spacers. (B) Single-row PTCDA structure. (C) Alternate single-/double-PTCDA rows. (D) PTCDA double-row structure. (E) Array of PTCDA nanoislands using TAPT as a spacer. (F) Herringbone phase of PTCDA formed without co-deposition of spacer molecules.

The range of PTCDA nanostructures that have been grown in two dimensions during this study, based on the use of hydrogen bonding spacers, is summarized in Figure 28. Stoichiometry, overall coverage and particularly the shape of the amine-functionalized spacers can be used to tune the PTCDA structures. The concept of hydrogen-bonding spacers is obviously not limited to Au(111) but will work on any substrate where the adsorption structure does not crucially depend on adsorbate-substrate interactions. This approach hence offers a way towards the creation of ordered arrays of organic semiconductor nanostructures with potential application as 2D quantum dots [188]. The same construction concept might also be extended to three dimensions. By growing structures in a layer-by-layer fashion, the size of the PTCDA clusters may be modulated as a function of thickness by varying the stoichiometry and/or the hydrogen bonding spacers. The concept is not limited to the PTCDA-amine system presented here but should work for any combination of carefully designed molecules A and B for which homomolecular interactions e.g. A···A are less stable than heteromolecular complexes A···B, with the additional constraint that both these interactions are nevertheless much stronger than the second type of homomolecular interactions e.g. B···B such that A···B>(A···A+B···B)/2. Stoichiometry and geometric design of B will hence allow the creation of pure A phases resembling monolayer/bulk structures separated by type B spacers.

In summary, we have presented a model system where binary self-assembly critically depends on a subtle balance between homo- and heteromolecular interactions, which then allows for a variety of intermixed supramolecular structures consisting of nanoislands of the species exhibiting strong homomolecular interactions embedded into a spacer matrix consisting of the second species. This approach may be used for the growth of self-assembled nanostructures of the organic semiconductor PTCDA with the ability to tune the structures by the co-deposition of amine-functionalized spacer molecules exploiting the subtle balance between homomolecular PTCDA interactions and hydrogen bonding with the spacer molecules. The hydrogen bonds between PTCDA and amine groups of polycyclic aromatic hydrocarbons are ideal candidates to compete with PTCDA-PTCDA interactions due to their comparable interaction energies, giving rise to highly ordered arrays of PTCDA clusters. The range of nanostructure superlattices might easily be extended and their exact shape tuned by appropriate design of the amine-functionalized hydrogen bonding spacers.

Supporting information for

Tailoring low-dimensional organic semiconductor nanostructures

Matthias Treier, Manh-Thuong Nguyen; Neville V. Richardson, Carlo Pignedoli,
Daniele Passerone, Roman Fasel

Superstructure between TAPT and PTCDA with stoichiometry different from 7:4

Apart from the predominant superstructure where clusters consisting of 7 PTCDA are spaced using 4 TAPT per unit cell, a variety of this superstructure is also observed as shown in Figure 29. Clusters consisting of 3 or 4 PTCDA molecules are surrounded by TAPT. These PTCDA clusters closely resemble subunits of the larger 7-membered PTCDA clusters as becomes apparent by comparing Figures 29 and 27. The smaller clusters are occasionally observed at the edges of larger islands comprising exclusively 7-PTCDA clusters.

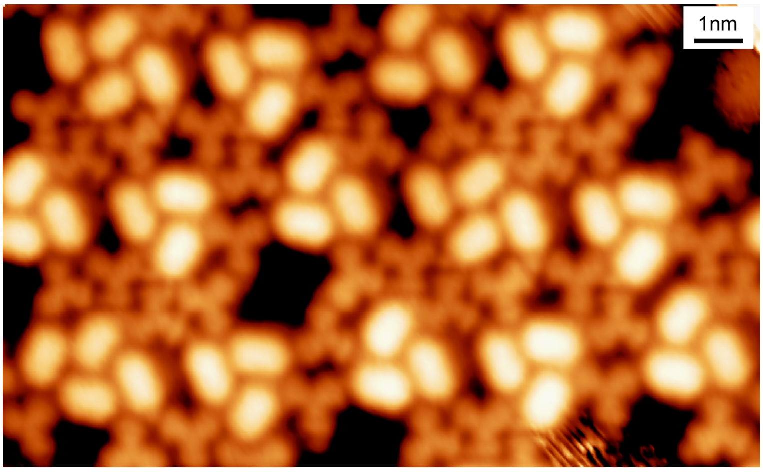

Figure 29: STM image of alternative superstructure formed by TAPT and PTCDA. Clusters consisting of 3/4 PTCDA molecules are kept apart by TAPT. Scan parameters: -1.5V, 10pA.

Homomolecular DATP / PTCDA superstructures on Au(111)

At submonolayer coverage, no stable homomolecular DATP structures have been observed at 77K on Au(111). DATP not bound within intermixed structures cannot be imaged stably at this temperature and is believed to be responsible for noisy features in the STM images. Ordered DATP superstructures have only been observed at almost complete monolayer coverage. An example of such a structure is given in Figure 30. Molecules are close-packed with a packing density of approximately one molecule per nm^2. An example of the close packed herringbone structure of PTCDA on Au(111) is also given in Figure 30. The reconstruction of the underlying substrate is still visible.

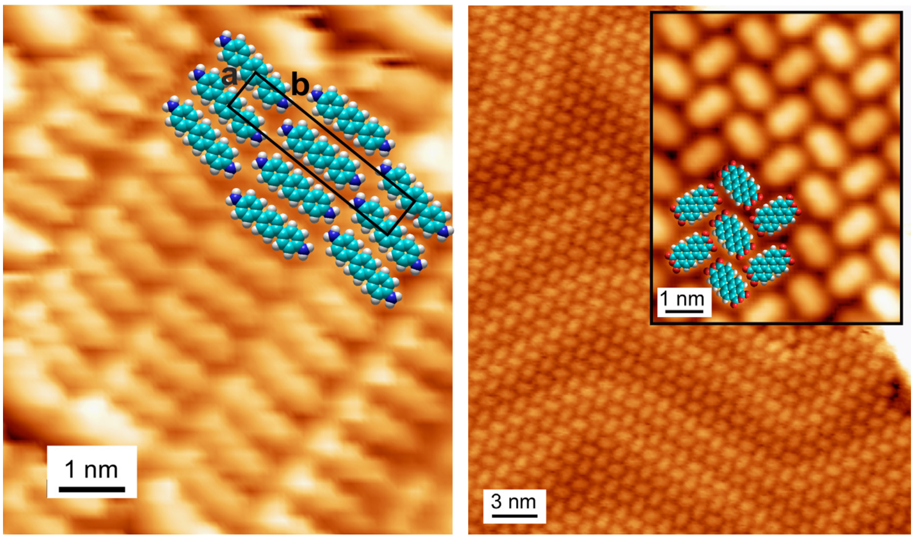

Figure 30: (left) DATP superstructure observed at almost complete monolayer coverage. Unit cell dimensions: a=0.65nm, b=3.1nm. Scan parameters: -0.6V, 10pA. (right) Herringbone superstructure formed by PTCDA. Scan parameters: -1.8V, 10pA

Computational details

Density Functional Theory (DFT) simulations were carried out to compare the binding energies of mixed DATP-PTCDA and pure PTCDA two-dimensional phases. Moreover, we investigated at a higher level of theory some of the possible dimers that can act as building blocks for the observed nanostructures.

For the plane wave calculations we used the q-Espresso [202] code. Ultrasoft pseudopotentials were used for all atomic species and a cut-off of 35 Ry (280 Ry) was used for the expansion of wavefunctions (charge density) in plane waves. We calculated the formation energies of flat hydrogen-boned configurations with respect to flat isolated molecules. All geometries were fully relaxed, no symmetry constraints were imposed. The initial planarity of the molecules is preserved during optimization.

For PTCDA a unit cell of size (19.63 x 24.75 x 10) Å^3 containing four molecules was used to model an infinite periodic aggregate (Figure 31a). We then relaxed the isolated molecule in the same supercell, and we found an energy gain of 0.88 eV per molecule-couple.

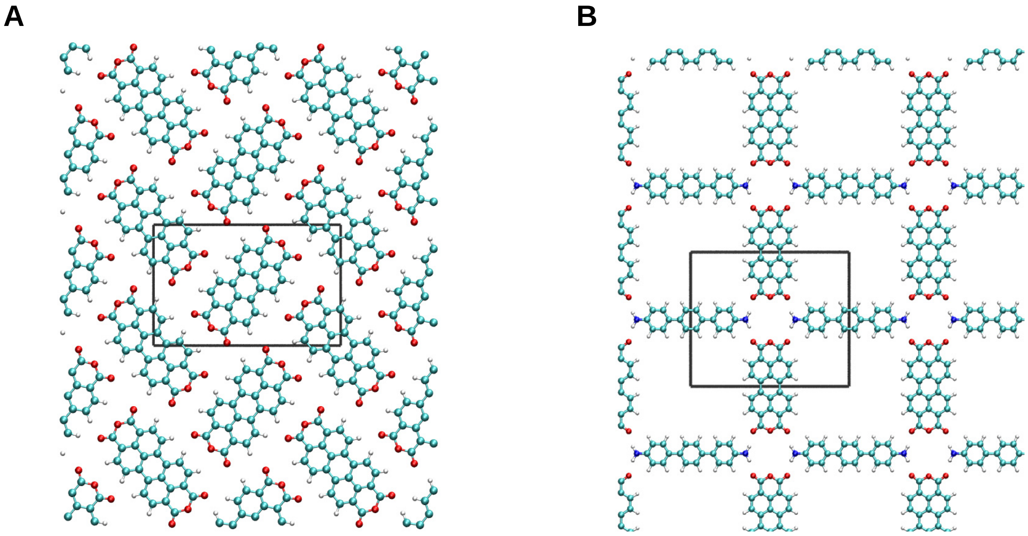

Figure 31: Geometries of two periodic superstructures investigated with DFT calculations: (A) PTCDA network; (B) planar DATP-PTCDA cross network. In both cases the unit repetition cell is indicated; the simulated cell was twice as big in the y direction in both cases.

For the DATP-PTCDA superstructure, we considered a 2DATP-2PTCDA cross configuration in a periodic supercell of (20.93x34.52x10) Å ^{3} (Figure 31b). After relaxing DATP and PTCDA separately with the same supercell size, we found the energy gain to be 0.87 eV per DATP-PTCDA unit (degenerate, according to our accuracy, with the PTCDA-PTCDA periodic case) resulting in 0.22 eV per hydrogen bond. We note in passing that calculations done in the same cell for dimers in the gas phase (not shown) at the same level of theory have shown a binding energy per hydrogen bond of the same order of magnitude for both cases, thus allowing to exclude at present any resonance assisted hydrogen bonding enhancing the stability of the periodic structures.

At this stage, the effect of the surface was implicitly included only by keeping the superstructure planar. The major effect of the gold surface, apart from dispersive interactions with the aromatic rings of both molecules, is expected on the amine ends of DATP. Whether and how these interactions will affect the relative strength of both superstructures investigated is an important matter of future theoretical work.

Next, we investigated in detail different dimers in the framework of quantum chemistry with Gaussian basis sets, using the hybrid functional B3LYP, which includes 20% of exact exchange [193, 194]. This functional has shown a good predictive power in the case of hydrogen bonding structure. We used the valence triple zeta basis set augmented with d- and p-like polarization functions 6-311 G(d, p) [195], as encoded in PCGAMESS [203].

Before computing intermolecular interactions, the geometries of PTCDA and DATP have been relaxed in the gas phase. The relaxed geometry of PTCDA in our simulation is in excellent agreement with these results. However, the energetic positions of frontier orbitals are E^{HOMO}= -6.69 eV and E^{LUMO}=-4.13eV (energy gap = 2.56 eV) in our case compared with -6.61eV and -4.00eV (energy gap = 2.61 eV)[204], respectively. There are no published theoretical studies of DATP. Relaxed in the gas phase, a nonplanar global minimum structure is found for DATP with the central ring being rotated by ~40° with respect to the two terminal rings (not shown here). However, in view of conformational adaptation in the adsorbed state, we restricted our research to planar geometries of DATP.

The binding energies of several PTCDA-DATP dimers have been computed within different reasonable relative orientations. All simulations have been performed in the gas phase with the influence of the surface being accounted for by restricting the geometry to being planar. The binding energy of a molecular system, which is defined as the energy difference between the total energies of the whole system and its constituents, is determined using single point energy calculations of the fully optimized systems.

In the Gaussian basis set framework, the full system contains more orbitals than each of its constituents do, which results in the well-known basis set superposition error (BSSE), which would be zero if the basis sets were complete. One of the most successful approaches to minimize this error is the a posteriori counterpoise method introduced by Boys and Bernardi [205]. Mathematically, this binding energy is expressed as [206]:

$$\Delta E^{cp}(AB) = [E_{AB}^{AB}(AB) - E_{A}^{A}(A) - E_{B}^{B}(B)] + [E_{AB}^{A}(A) - E_{AB}^{AB}(A) + E_{AB}^{B}(B) - E_{AB}^{AB}(B)] = \Delta E(AB) + \delta_{AB}^{BSSE}$$

Where $E_Y^X(Z)$ stands for the total energy of system Z at geometry Y with basis set X. It should be noted that with plane-wave there is no need to consider the BSSE at all.

PTCDA-DATP and PTCDA-PTCDA dimers

PCGAMESS was used to study dimers of one DATP and one PTCDA at the B3LYP level of theory. Planarity was imposed on the system. The optimized geometries for two different dimers are shown in Figure 32. The computed binding energies in both cases (A) and (B) are found to be 0.15 eV. The molecular axes are at a right angle in 32a and at about 45° in 32b. Experimentally, a geometrical arrangement resembling the one in Figure 32b is found within the double DATP structures between islands of the rectangular superstructure (Figure 25c). However, experimentally an angle of only 30° between the molecular axes is observed.

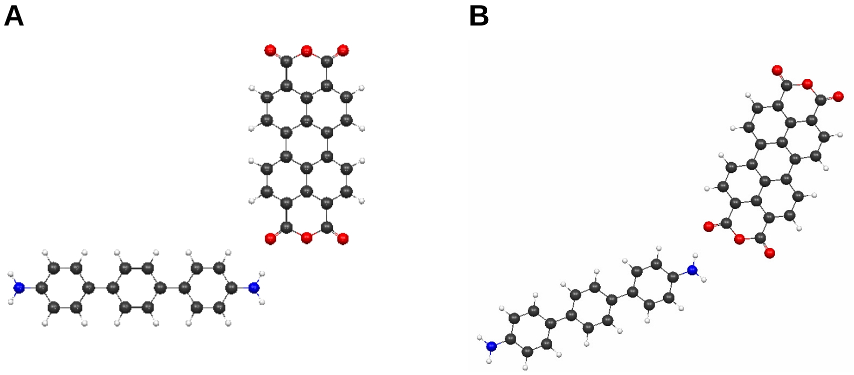

Figure 32: Geometries of two relaxed coplanar DATP-PTCDA dimers. (A) Dimer in which orthogonality between the molecular axes has been imposed. (B) Dimer relaxed without constraints (apart from planarity) imposed on the system. In both cases the binding energy was found to be 0.15 eV.

At the same level of theory we also studied different PTCDA dimers (Figure 33). In all cases we found almost the same binding energy of about 0.2 eV, thus indicating the flexibility of this building block that is reflected in the possibility of building different 2D structures on the surface. These numbers cannot be directly compared with the results with the BLYP functional in the plane wave framework. We are currently investigating periodic systems at a higher level of theory using appropriate quantum chemistry packages.

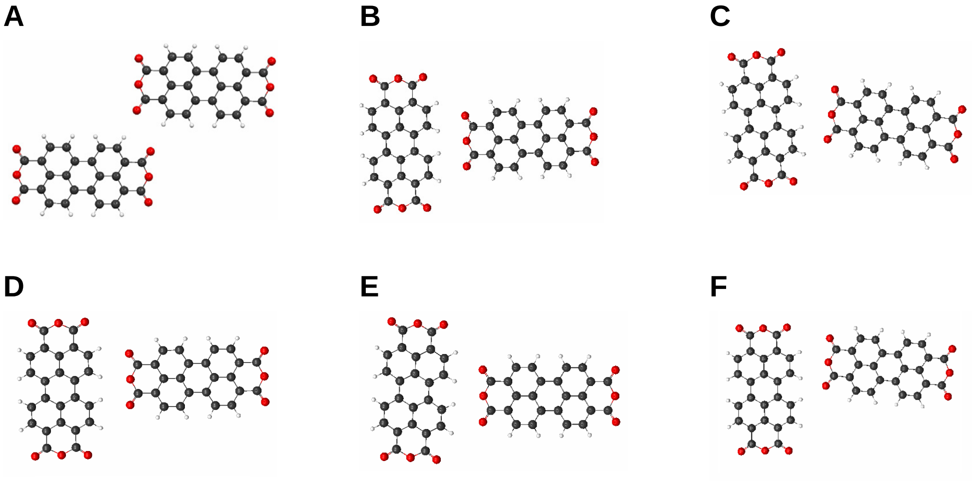

Figure 33: Geometries of PTCDA dimers. Computed binding energies are (A) 0.19eV, (B) 0.21eV, (C) 0.18eV, (D) 0.20eV, (E) 0.21eV, (F) 0.17eV.

6 Covalent supramolecular architectures

6.1 Introduction

Among the most promising potential applications of self-assembled supramolecular architectures on surfaces is their use as templates for the subsequent growth of both organic and inorganic nanostructures. While proof-of-principle experiments have demonstrated that this works for C_{60} [26, 207, 208] or other fullerenes [209, 210] and even self-assembled monolayers [211], the overall stability of such networks when used as templates with respect to both temperature and chemical environment is often far from being useful for technological applications as illustrated in Figure 34. Also, an ideal template would be applicable to a wide range of organic/inorganic materials. However, networks based on hydrogen bonds will obviously be affected if a molecular adsorbate – capable of forming hydrogen bonds with one of the network partners – will be deposited on it, or if a metal that can be coordinated by the functional groups of the network molecules is deposited. The same applies analogously to metal-coordination networks.

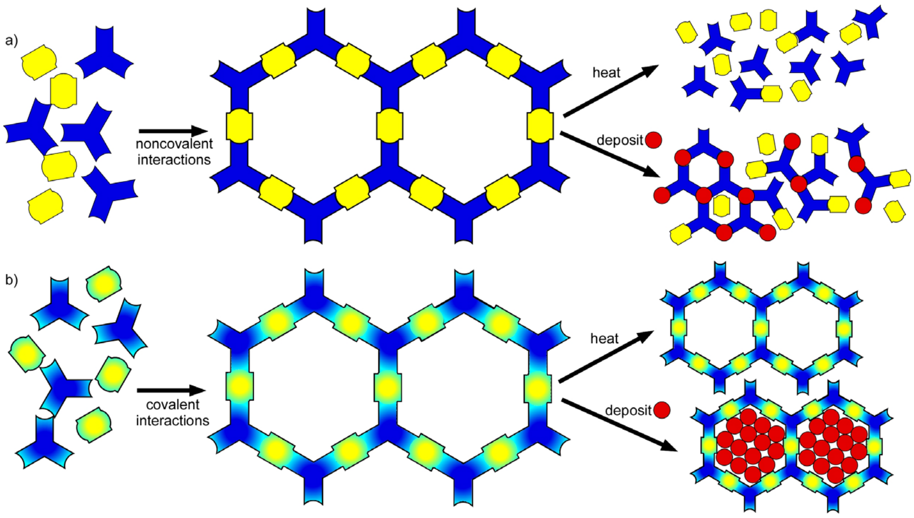

Figure 34: Schematic illustration of advantages regarding thermal and chemical stability of covalent (a) over non-covalent (b) networks.

To achieve a higher chemical and thermal stability, networks formed by covalent bonds rather than noncovalent interactions are necessary. This has fuelled research interest in the creation of surface-supported polymeric networks over the last few months [212-215]. Reactions known from polymer chemistry have been found to proceed also if the reactants are confined to two dimensions. While catalytic reactions of small molecules had been studied on single crystal surfaces for several decades, the formation (and detailed observation by STM) of submonolayer thick polymeric structures is a very young field of surface science. Tip-induced reactions had been reported previously [216, 217]. However, these reactions did obviously not have the potential for the large scale creation of extended covalently linked supramolecular networks, which are now achieved by temperature activated reactions.

The formation of extended covalently bound supramolecular structures formed by surface-confined imidization on Au(111) has been investigated by STM in this chapter. While the ultimate goal – a highly ordered porous network – has not been achieved, a highly stable porous network has been realized and – depending on the preparation conditions – polyimide strands are found to self-assemble into patches of locally aligned polymeric units, showing that even large polymeric molecules can form ordered structure through self-assembly. Furthermore, a detailed investigation of the imidization condensation reaction for reactants confined on a surface in UHV is presented in this chapter.

6.2 Fabrication of surface-supported low-dimensional polyimide networks

J|A|C|S
COMMUNICATIONS

Fabrication of Surface-Supported Low-Dimensional Polyimide Networks

Matthias Treier,† Neville V. Richardson,‡ and Roman Fasel*,†

EMPA, Swiss Federal Laboratories for Materials Testing and Research, 3602 Thun, Switzerland, EaStCHEM, School of Chemistry, North Haugh, University of St. Andrews, St. Andrews, KY16 9ST, United Kingdom

Received July 10, 2008; E-mail: roman.fasel@empa.ch

A wide variety of highly regular supramolecular architectures, based on noncovalent bonds, has been realized on single crystal metal surfaces over the past decade.[1] In view of possible applications as templates, covalent bonding is however preferable to meet the optimal requirements of thermal and chemical stability. Attempts to fabricate covalently interlinked polymeric networks on single crystal metal surfaces have been reported only very recently.[2] Different types of chemical reactions have been found to proceed even though the reaction partners are confined to two dimensions,[3] while novel reaction pathways, which have no known equivalent in 3D chemistry, have also been reported.[4]

Polyimides represent a particularly important class of polymers which have found applications, inter alia, in electronic device insulation, X-ray windows, planar substrates for LCD displays, or cryogenics.[5] Synthesis of polyimide films has been achieved by various routes including physical vapor deposition of the precursor monomers[6] and spin casting[7] or Langmuir−Blodgett deposition of the intermediate polyamic acid.[8] Polyimides are generally chemically resistant, low-k dielectrics with a high decomposition temperature,[5] hence ideally fulfilling the requirements of thermal and chemical stability needed for potential technological applications of covalent surface-supported networks.

Here, we investigate the formation of ultrathin polyimide films on Au(111) using low temperature scanning tunneling microscopy (STM). According to textbook chemistry, imidization (Scheme 1) proceeds via rearside, out-of-plane nucleophilic attack of the amine on a carbonyl group, a mechanism which is expected to be strongly hindered when the two reactants are confined to two dimensions. We show, however, that the surface-confined imidization of aromatic amines and anhydrides readily takes place above ∼570 K but that the temperatures needed for the different reaction steps are different from the corresponding reaction in solution or in bulk films. Covalently linked (sub)monolayer, one precursor molecule thick, polyimide films can be grown on Au(111) whose detailed structures can be tuned from parallel linear strands to an extended, 2D connected, porous network by varying the amine species used in the reaction.

STM experiments were performed in an ultrahigh vacuum system using an Omicron low-temperature STM operated at 77 K. The Au(111) crystal was cleaned by sputtering and subsequent annealing to 700 K prior to adsorbate deposition. 4,4′-Diamino-*p*-terphenyl (DATP, 95%, ABCR), 2,4,6-tris(4-aminophenyl)-1,3,5-triazine (TAPT), and 3,4,9,10-perylenetetracarboxylic-dianhydride (PTCDA, 97%, Fluka) (Figure 1a) were deposited from resistively heated quartz crucibles held at 380, 470 and 510 K, respectively, resulting in deposition rates of ∼0.2 ML/min. During deposition, the sample was kept at room temperature. To initiate the formation of polyimides, the sample was annealed to 570 K for 15 min before transfer to the STM.

Scheme 1. Imidization Condensation Reaction

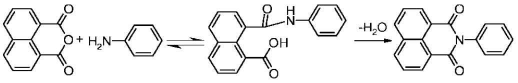

Figure 1b shows the rectangular hydrogen-bonded superstructure formed by DATP and PTCDA on Au(111) at submonolayer coverage when approximately equal amounts of the two species are present. Both molecules adsorb in a planar geometry on this substrate as widely found for molecules containing polycyclic aromatic units.[10] In contrast to solution-based and solid-state polyimide formation, poly(amic acid) is not formed within the first monolayer at room temperature. The hydrogen-bonded structures are not modified by annealing the sample up to approximately 470 K for several minutes. At even higher annealing temperature (∼470 to 540 K), few species ascribed to the amic acid intermediate are observed (see Supporting Information) but

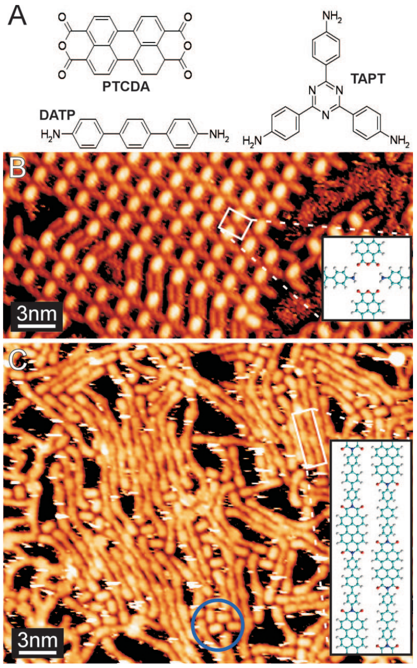

Figure 1. (a) Chemical structure of compounds used for surface polyimide formation. (b) STM image[9] (−0.5 V, 20 pA) of hydrogen-bonded DATP-PTCDA superstructure on Au(111). The inset shows a junction of the rectangular network. Bright molecules are PTCDA and long, dimmer molecules are DATP. (c) STM image (−1.8 V, 50 pA) of parallel polyimide strands formed from DATP and PTCDA after annealing at 570 K. The blue circle highlights a small cluster of nonreacted PTCDA. The inset shows a model of two parallel oligomers.

---

† EMPA.
‡ University of St. Andrews.

10.1021/ja805342n CCC: $40.75

no pure phases of this reaction intermediate can be obtained. Complete imide formation is possible even within the restricted geometry on the surface as observed by the formation of polyimide oligomers after annealing to 570 K as shown in Figure 1c. Individual oligimides agglomerate into patches of locally parallel strands. As can be seen by comparing Figure 1 panels b and 1c, the appearance of DATP and PTCDA is only weakly affected by the reaction with both precursors remaining easily identifiable within the polymeric units. Higher coverages can be achieved by repeating the deposition-annealing cycles. The sample shown in Figure 1c is richer in PTCDA resulting in most oligomers being terminated by PTCDA. Excess PTCDA, which has not reacted, can be found within voids of the polymeric structure as highlighted in Figure 1c. The chain termination can be changed to either PTCDA or DATP by simply providing an excess of the appropriate species during sample preparation. At coverages similar to or higher than the one shown in Figure 1c, no correlation between the orientation of the polyimide strands and the underlying substrate is observed. After annealing to 540 K, no unreacted DATP can be found on the substrate. Hence, the desorption temperature and the temperature needed for the onset of the reaction lie close together, suggesting that a high mobility of DATP is needed for reaction. This might be related to the known out-of-plane reaction geometry of the rearside nucleophilic attack, which might be achieved at temperatures close to the desorption temperature of DATP.

The periodicity along chains is 2.5 nm, in excellent agreement with the theoretical value of 2.56 nm obtained from relaxing an oligomer in the gas phase at the AM1 level of theory.[11] A hypothetical linear hydrogen-bonded structure would have a periodicity of ~3.0 nm, further indicating that the observed structures do not result from unreacted molecules. Typical chain lengths are 5−10 nm corresponding to 4−8 reacted molecules. Patches of coparallel oligomers are densely packed with a strand-to-strand spacing of ~0.75 ± 0.05 nm stabilized by CH•••O hydrogen bonds (see inset of Figure 1c). Longer chains and better ordering of the chains are probably inhibited by the confinement to two dimensions and the high coverage. Also, chain lengths can vary on the same sample depending on the local coverage, indicating that the length might be limited by kinetics during the polyimide formation process. By this method, a second layer cannot be grown on top of the first polyimide layer, since both reaction partners will desorb before the reaction temperature. The preparation of a monolayer thin polyimide film based on DATP and PTCDA on Au(111) can hence be a self-limiting process.

To explore the potential use of this surface-supported condensation reaction for the fabrication of extended two-dimensional polymeric networks, the imidization between PTCDA and the 3-fold symmetric triamine species TAPT has also been investigated. At a stoichiometry of 2 TAPT to 3 PTCDA, a hypothetical hexagonal polyimide honeycomb network with a pore-to-pore distance of 3 nm could be expected (see Supporting Information). Figure 2 shows the covalently linked structures formed by PTCDA and TAPT after annealing to 600 K. Regularly spaced pores are not obtained under these sample preparation conditions even if the required stoichiometry is met, as is the case for the sample shown in Figure 2, where polyimide structures are terminated by either of the two molecules. However, compared to the structures formed by the linear DATP, the network formed from PTCDA and TAPT is highly porous and exhibits an extensive 2D connectivity although pore shapes different from the anticipated hexagonal pores are common.

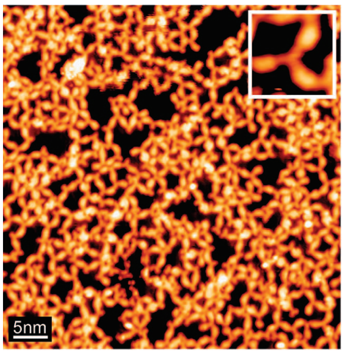

Figure 2. STM image (−0.8 V, 20 pA) of a porous polyimide network formed by TAPT and PTCDA at an approximate 3:2 stoichiometry. The inset shows a TAPT molecule at the center of a triangular arrangement connected by imidization to three PTCDA molecules.

While a highly regular network has not been realized with the preparation conditions chosen, the overall geometric properties of the submonolayer polyimide structures clearly depend on the choice of precursors, which hence represents a means to tailor the properties of the resulting polyimide monolayer.

In summary, we have shown that the condensation reaction between diamines and dianhydrides, resulting in the formation of polyimides, can be thermally initiated on Au(111), giving rise to covalently linked subnanometer thick polymeric structures, whose geometric properties can be tuned by an appropriate choice of the reaction partners.

Acknowledgment. We would like to thank N.R. Champness and S. Argent for providing the TAPT sample.

Supporting Information Available: STM images of amic acid; hydrogen-bonded superstructure and potential polyimide honeycomb network between TAPT and PTCDA. This material is available free of charge via the Internet at http://pubs.acs.org.

References

(1) (a) Theobald, J. A.; Oxtoby, N. S.; Phillips, M. A.; Champness, N. R.; Beton, P. H. *Nature* **2003**, *424*, 1029. (b) Barth, J. V. *Annu. Rev. Phys. Chem.* **2007**, *58*, 357. (c) Stepanow, S.; Lingenfelder, M.; Dmitriev, A.; Spillmann, H.; Delvigne, E.; Lin, N.; Deng, X.; Cai, C.; Barth, J. V.; Kern, K. *Nat. Mater.* **2004**, *3*, 229.

(2) (a) Weigelt, S.; Busse, C.; Bombis, C.; Knudsen, M. M.; Gothelf, K. V.; Laegsgaard, E.; Besenbacher, F.; Linderoth, T. R. *Angew. Chem., Int. Ed.* **2008**, *47*, 4406. (b) Zwaneveld, N. A. A.; Pawlak, R.; Abel, M.; Catalin, D.; Gigmes, D.; Bertin, D.; Porte, L. *J. Am. Chem. Soc.* **2008**, *130*, 6678.

(3) (a) Matena, M.; Riehm, T.; Stöhr, M.; Jung, T. A.; Gade, L. H. *Angew. Chem., Int. Ed.* **2008**, *47*, 2414. (b) Weigelt, S.; Schnadt, J.; Tuxen, A. K.; Masini, F.; Bombis, C.; Busse, C.; Isvoranu, C.; Atman, E.; Laegsgaard, E.; Besenbacher, F.; Linderoth, T. R. *J. Am. Chem. Soc.* **2008**, *130*, 5388. (c) Grill, L.; Dyer, M.; Lafferentz, L.; Persson, M.; Peters, M. V.; Hecht, S. *Nat. Nanotechnol.* **2007**, *2*, 687. (d) In't Veld, M.; Iavicoli, P.; Haq, S.; Amabilino, D. B.; Raval, R. *Chem. Commun.* **2008**, 1536. (e) Gourdon, A. *Angew. Chem., Int. Ed.* **2008**, *47*, 6950.

(4) Weigelt, S.; Busse, C.; Bombis, C.; Knudsen, M. M.; Gothelf, K. V.; Strunskus, T.; Wöll, C.; Dahlbom, M.; Hammer, B.; Laegsgaard, E.; Besenbacher, F.; Linderoth, T. R. *Angew. Chem., Int. Ed.* **2007**, *46*, 9227.

(5) (a) Ding, M. *Prog. Polym. Sci.* **2007**, *32*, 623. (b) Halasa, E. *Polimery* **2005**, *69*, 179.

(6) (a) Jou, J. H.; Cheng, C. L.; Jou, E. C. Y.; Yang, A. C. M. *J. Polym. Sci., B* **1996**, *34*, 2239. (b) Salem, J. R.; Sequeda, F. O.; Duran, J.; Lee, W. Y.; Yang, R. M. *J. Vac. Sci. Technol., A* **1986**, *4*, 369.

(7) Meyer, W.; Grunze, M.; Lamb, R.; Ortega-Vilami, A.; Schrepp, W.; Braun, W. *Surf. Sci.* **1992**, *273*, 205.

(8) Ghosh, M. K., Mittal, K. L. *Polyimides: Fundamentals and Applications;* Taylor & Francis: London, 1996.

(9) STM-images have been analyzed and processed using WSxM: Horcas, I.; Fernandez, R.; Gomez-Rodriguez, J. M.; Colchero, J.; Gomez-Herrero, J.; Baro, A. M. *Rev. Sci. Instrum.* **2007**, *78*, 013705.

(10) Ruffieux, P.; Gröning, O.; Fasel, R.; Kastler, M.; Wasserfallen, D.; Müllen, K.; Gröning, P. *J. Phys. Chem., B* **2006**, *110*, 11253.

(11) Dewar, M. J. S.; Zoebisch, E. G.; Healy, E. F.; Stewart, J. J. P. *J. Am. Chem. Soc.* **1985**, *107*, 3902.

JA805342N

Supporting information for

Fabrication of surface-supported low-dimensional polyimide networks

Matthias Treier, Neville V. Richardson, Roman Fasel

Amic acid reaction intermediate

After annealing in the temperature range between 470K and 540K, few examples of species ascribed to the amic acid reaction intermediate can be observed, in particular around the periphery of hydrogen-bonded domains (Figure 35). However, no pure phases of the reaction intermediate are observed, which always co-exist with hydrogen bonded structures and/or fully reacted polyimides. The characteristic feature of the amic acid structures is a protrusion located at the reaction site between the two molecules.

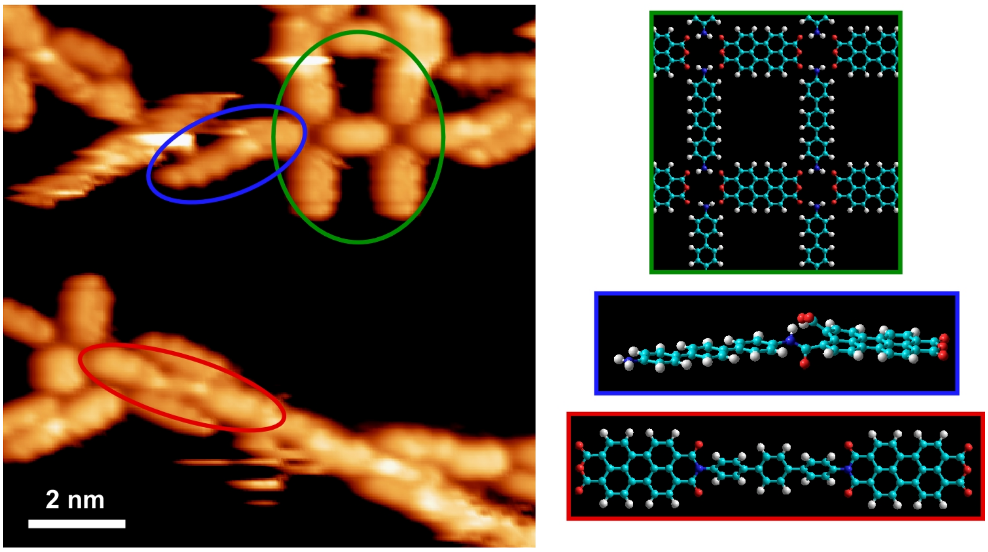

Figure 35: STM image (+0.5V, 20pA) of submonolayer of DATP and PTCDA after annealing to 540K. Remnants of the rectangular hydrogen bonded structure (green), imide products (red) and potential amic acid reaction intermediates (blue) are observed simultaneously. Further views of the amic acid model (blue) are shown in Figure 35.

In the gas phase, the amic acid has a strongly non-planar geometry as found by relaxing its structure at the AM1 level of theory [111] (Figure 36a). On the surface, it can however be expected that the geometry is constrained to a much more planar one. We have modelled an amic acid in the adsorbed state (Figure 36b) and computed the corresponding STM image using extended Hückel simulations. As a model a planar DATP and PTCDA backbone have been linked to form an amic acid and only the atoms from the amine/anhydride group involved in amic acid formation have been relaxed using the AMBER force-field [218]. The angle between the molecular axes has been kept fixed at 30° which corresponds to the experimentally observed value. As can be seen in the side view in Figure 36b, the resulting structure is not planar, with oxygen atoms pointing away from the plane defined by the molecular backbones in both directions. It should be noted that for reasons of steric interference, it is not possible to render this amic acid structure completely flat without a large increase in strain energy. The simulated STM image in Figure 36c shows that a protrusion located over the upwards-pointing carbonyl oxygen similar to the experimental observation (see blue structure in Figure 35) is obtained. The overall agreement between the simulated and experimental STM image shows that the blue structures in Figure 35 can indeed be explained as amic acid reaction intermediates.

A simulated STM image for a polyimide unit consisting of two PTCDA and a linking DATP is shown in Figure 36e. The simulated image is in excellent agreement with the experimental observation (see red structure in Figure 35).

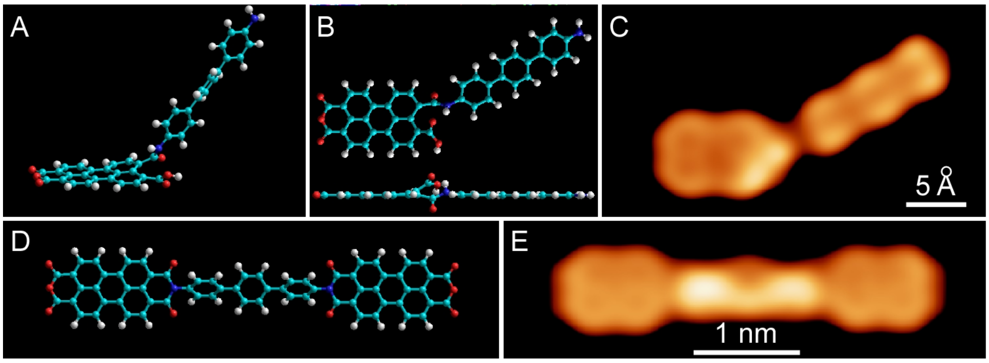

Figure 36: (A) Geometric structure of the amic acid relaxed with AM1 in the gas phase. (B) Top- and side-view for model of surface-confined amic acid. (C) Simulated STM image for the amic acid shown in (B). Structure (D) and simulated STM image (E) of a PTCDI-DATP-PTCDA imide unit relaxed with AM1 in the gas phase.

Hydrogen bonded structure of non-reacted TAPT and PTCDA

Co-deposition of TAPT and PTCDA on Au(111) leads to a unique superstructure with a unit cell containing 7 PTCDA and 4 TAPT, stabilized by hydrogen bonds (Figure 37). The structure shown in Figure 37 has been readily observed at 77K after depositing the two species with the sample held at room temperature without annealing the sample before transferring it to the STM.

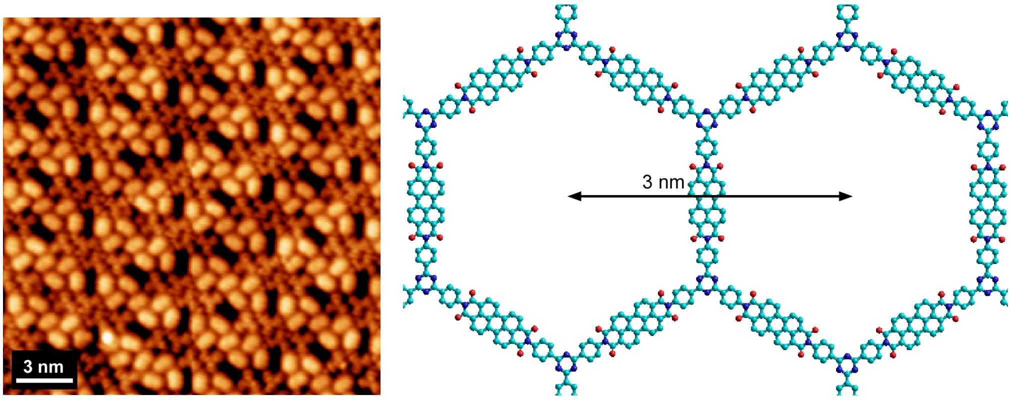

Figure 37: (left) STM image (-1.5V, 10pA) of hydrogen bonded superstructure of TAPT and PTCDA. (right) Theoretically predicted covalent polyimide network formed between TAPT and PTCDA with a pore-to-pore distance of 3nm.

6.3 Molecular Imaging of Polyimide Formation

Matthias Treier[1], Roman Fasel[1], Neil R. Champness[2], Stephen Argent[2],
Neville V. Richardson[3]

*[1] Empa, Swiss Federal Laboratories for Materials Testing and Research,
nanotech@surfaces laboratory, 3602 Thun and 8600 Dübendorf, Switzerland*
*[2] School of Chemistry, University of Nottingham, University Park, Nottingham NG7
2RD, United Kingdom*
*[3] EaStCHEM, School of Chemistry, University of St. Andrews, St. Andrews KY16 9ST,
United Kingdom*

Physical Chemistry Chemical Physics **11**, 1209-1214 (2009)

Abstract

At temperatures in the range of 300K to 700K and at coverages up to one monolayer on a Au(111) surface, the reactions of 3,4,9,10-perylenetetracarboxylic-dianhydride with 4,4’-diamino-p-terphenyl and with 2,4,6-tris(4-aminophenyl)-1,3,5-triazine have been followed by low temperature UHV-STM. Well-ordered, H-bonded structures are observed at temperatures to 470K, while above 550K reaction is initiated with evidence of amic acid intermediates. At higher temperatures, full imidisation leads to covalently linked, surface polyimide networks. There is evidence of the gold reconstruction playing a role in the early stages of imidisation and signs of limited order in the final polyimide. With the diamine as precursor 1D interconnectivity results, while with the triamine as partner, full 2D connectivity is possible. In contrast to the situation in the bulk, the intermediate amic acid seems to be less stable and iso-imides are common in the final networks, as witnessed by the conformation of the product and the prevalence of triangular features in the case of the polyimide formed from the triamine precursor.

There has been a recent surge of interest in the formation and characterisation of two dimensional, covalent organic networks based on a variety of thermally induced chemical reactions at surfaces [213-215, 219]. The aim of these studies has been to develop covalent polymeric networks in the coverage range to one monolayer as structures potentially more stable than those based on H-bonded or metal organic frameworks for use in bottom up device technologies, sensors and as substrates with controlled adhesive, dielectric or hydrophobic properties. Successful studies have exploited boronic acids in self-condensation or condensation with a molecule containing multiple diol functionalities [214], the coupling of porphyrins through a C-C linkage via elimination of Br_2 from tetra(4-bromophenyl)porphyrin [215], the coupling of porphyrins via a radical mechanism supported by a copper substrate [219] and oligomerisation of N-heterocyclic carbenes [213]. Weigelt has also demonstrated polymer formation on Au(111) based on imine formation in the reaction between vapour deposited amines and aldehydes [220, 221]. Here, we present results of detailed investigations in which thermally induced imidisation reactions between aromatic anhydrides and aromatic amines leading to polyimides are characterised by UHV-STM. H-bonded networks stable to at least 470K are followed as a function of annealing temperature to full polymer formation at coverages up to one monolayer.

Polyimides (PI) have been widely studied by physicists, chemists, material scientists and engineers for more than two decades. The interest in these polymers arises from their technological importance, based on their high thermal and chemical stability, together with their low k dielectric and other desirable properties [222-227]. Polyimides have found widespread, large volume use as insulators but are also widely employed as low k dielectrics in the device industries and as the substrate of choice for liquid crystal displays [222, 228]. Polyimides are readily formed both in solution and in the solid state by a condensation reaction between a dianhydride and a diamine. The reaction takes place via a stable polyamic acid intermediate. Final imidisation is achieved either by a chemical dehydration process or, more commonly, by thermally induced loss of water. Of course, there is a very wide choice of diamines and dianhydride precursors available to achieve the desired properties in the resulting polymers.

Preparation of thin polyimide films is often required and can be achieved by spin coating the intermediate polyamic acid, by use of Langmuir-Blodgett (LB) [229-231] techniques or by vacuum deposition [232-235] of the diamine and dianhydride precursors. Subsequent characterisation of the thin films with respect to their thickness, mechanical properties, degree of crystallinity, degree of imidisation (as a function of imidisation time/temperature) and incorporation of monomers, in the case of vapour deposited films, has been carried out, in particular, by FTIR [232] but also by several other methods including SEM [232], Raman [236], X-ray diffraction [237], ellipsometry [238], XPS [231] and thermogravimetric analysis [232]. The properties of the polyimide film interface, with the substrate on which it has been deposited, are important for many applications, relating as they do to adhesion and film growth characteristics [223]. There have, however, been rather few studies of PI growth from vapour deposited precursors in the coverage range from sub-monolayer, through monolayer to a few monolayers [232-235]. Some studies have suggested that order found within thin films is reduced at the surface [239, 240] and vibrational spectroscopies have indicated a higher percentage of the iso-imide species arising from a minor side reaction of the precursor molecules [241-243]. Annealing or the use of higher imidisation temperatures reduces the amount of iso-imide, at least within the film. Curing temperatures above 250^{o}C are also claimed to be capable of converting any residual iso-imide into the corresponding imide [242], although with increasing basicity of the diamine precursor, the thermal stability of the polyiso-imide increases [243].

The quality, roughness, alignment and order at the film surface has also been characterised by AFM [232, 244] and occasionally by STM. Previous STM studies of polyimide films are limited to early, relatively low resolution studies of LB deposited films on gold, silicon or graphite single crystal surfaces revealing aligned PI strands along high symmetry directions with spacings along and between the chains consistent with the molecular structure of the PI [229, 245]. Surprisingly, therefore, there appears to have been no previous STM studies of the very earliest stages of precursor interactions or imidisation in the sub-monolayer regime.

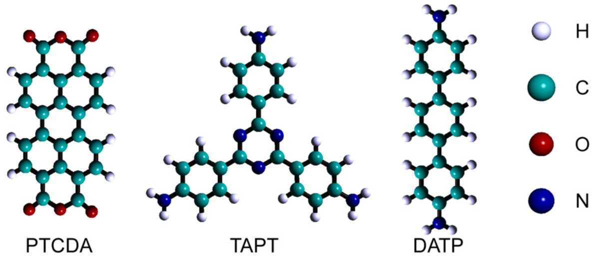

Figure 38: Precursor molecules used in surface imidisation studies. 3,4,9,10-perylenetetracarboxylic-dianhydride (PTCDA), 4,4’-diamino-p-terphenyl (DATP) and 2,4,6-tris(4-aminophenyl)-1,3,5-triazine (TAPT).

In this paper, we present the results of sub-molecular resolution, UHV-STM investigations of the complete reaction between two pairs of polyimide precursors each vapour deposited to sub-monolayer coverage on a clean, reconstructed Au(111) in ultra-high vacuum (UHV), as a function of the annealing temperature responsible for the imidisation step leading to surfaces with polymer coverages up to one monolayer. Figure 38 shows the precursor combinations which have been studied: 3,4,9,10-perylenetetracarboxylic-dianhydride (PTCDA), with 4,4’-diamino-p-terphenyl (DATP) and PTCDA with 2,4,6-tris(4-aminophenyl)-1,3,5-triazine (TAPT).

PTCDA is a planar molecule, whose adsorption on several different surfaces has been widely studied as a prototypical molecular semiconductor. On Au(111) in the coverage range to one monolayer, PTCDA adopts an orientation, in which the essentially undistorted molecular plane lies parallel to the substrate surface, and forms two distinct, well-ordered structures [186]. These have been previously well-characterised and both were observed during the present study. DATP has a linear arrangement of three phenyl rings but, as an isolated species, is not expected to be fully planar because of some steric hindrance at the *ortho* positions of adjacent rings. A DFT (6-311g basis set, B3LYP functional) calculation indicates that the terminal phenyl rings with their associated amino groups are co-planar but the central phenyl ring prefers to be twisted out of this plane by approximately 37°. The barrier to achieving planarity however is only 17 kJ mol^{-1} and a higher adsorption energy for a planar structure on Au(111) may be sufficient to reverse this preference. A similar argument is likely to apply to TAPT molecules, which are also expected to be non-planar as isolated species due to a twist of the amino substituted phenyl rings with respect to the central triazine ring but nevertheless adsorption on Au(111) may well favour a planar geometry. Bonding of all three molecules to the Au(111) surface is likely to have a strong dispersion component and the barriers to diffusion are likely to be very small.

A limited study of mellitic anhydride/DATP was also carried out successfully (not reported here) but an attempt to carry out the reaction between PTCDA and melamine was unsuccessful, which is ascribed to desorption of the melamine at temperatures well below that required for onset of the reaction. H-bonded networks of melamine and PTCDA have however been reported on Ag/Si(111) surfaces [196].

The reaction leading from amine and anhydride precursors through a stable amic acid and related intermediates to the imide and iso-imide products is shown in Scheme 1.

Experimental

STM experiments were performed in an ultra high vacuum system (base pressure $<2\cdot10^{-10}$mbar) using an Omicron low-temperature STM operated at 77K. The Au(111) crystal was cleaned by cycles of sputtering and subsequent annealing to 700K prior to adsorbate deposition. 4,4'-diamino-p-terphenyl (DATP, ABCR, 95%), 2,4,6-tris(4-aminophenyl)-1,3,5-triazine (TAPT) and 3,4,9,10-perylenetetracarboxylic-dianhydride (PTCDA, Fluka, 97%) were deposited from resistively heated quartz crucibles held at 400K, 500K and 510K respectively resulting in deposition rates of ~0.2 ML/min. During deposition, the Au(111)sample was kept at room temperature. To initiate the formation of polyimide, the sample was annealed to 570K for 15 minutes before transfer to the STM. All STM images were collected at a sample temperature of 77K and the quoted bias is that applied to the sample.

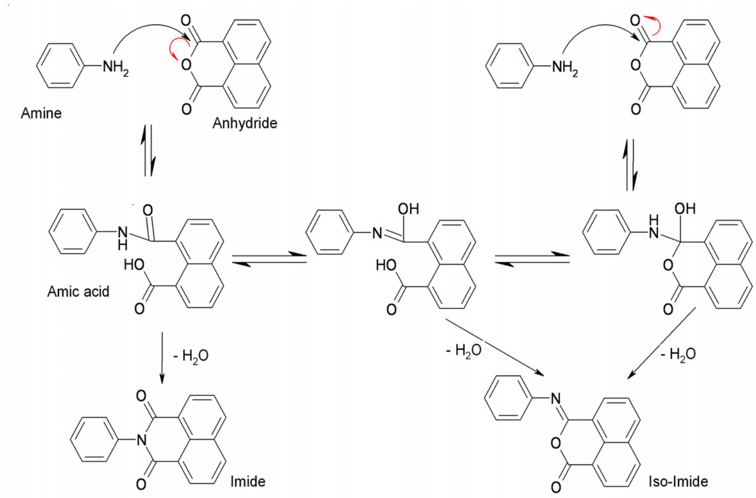

Scheme 1: Reaction of an anhydride with an amine leading to imide and iso-imide products via amic acid and related intermediates.

Synthesis of 2,4,6-Tris(4-aminophenyl)-1,3,5-triazine

2,4,6-Tris(4-aminophenyl)-1,3,5-triazine (TAPT) was prepared using small modifications to the literature procedure [246]. Under an Ar atmosphere a purple solution of $Pd(dba)_2$ (104 mg, 0.18 mmol) and $P(^tBu)_3$ (0.2 cm^3, 1.0 M in hexane, 0.18 mmol) in dry toluene (3 cm^3) was allowed to stand for 30 min before being added to a suspension of 2,4,6-tris(4-bromophenyl)-1,3,5-triazine [247]. (300 mg, 0.55 mmol) in dry toluene (10 cm^3). Lithium bis(trimethylsilyl)amide (3.2 cm^3, 1.0 M in hexane, 3.2 mmol) was added to the stirred reaction mixture which immediately turned dark brown. The reaction mixture was heated at 80°C for 16 hours during which time the colour lightened to a pale brown. The reaction mixture was cooled, quenched with HCl (1.0 M, 5 cm^3), diluted with water (10 cm^3), filtered to remove the precipitated lithium bromide and washed with Et_2O (2 x 20 cm^3). NaOH (1.0 M, 10 cm^3) was added to the aqueous phase resulting in a pale yellow solution which was concentrated to yield the product as a pale yellow solid (101 mg, 52%) which was collected by filtration and washed with water and methanol. ^{1}H-NMR (DMSO-D_6, 270 MHz): 8.37 (6H, d, *J* 8.6), 6.71 (6H, d, *J* 8.6), 5.95 (6H, s); EI-MS: *m/z* 354 [M^+].

Results and discussion

PTCDA/DATP reaction

PTCDA and DATP were deposited sequentially, each to approximately 0.3ML coverage, on the clean Au(111) surface held at room temperature, prior to STM imaging. Well ordered, H-bonded structures were obtained by this procedure: Figure 39a shows two different H-bonded structures. In the upper left part of this figure, the local PTCDA/DATP stoichiometry is 2:1, while in the lower right, it is 1:1. Each molecule is readily identified by its size and shape at different tunnelling bias voltages. Further discussion of the H-bonded structures found in this study is presented elsewhere. At this stage, it is sufficient to note that the molecules lie essentially flat on the surface and are sufficiently mobile, even at 77K, to prevent stable images of isolated monomers being obtained. The H-bonded structures are aligned in three equivalent, rotational domains on the (111) surface, with the long axis of the PTCDA parallel to the <211> directions and that of the DATP parallel to the close-packed <110> directions as seen, for example, in Figure 39b for the structure at 1:1 stoichiometry. The networks are readily imaged across a range of biases and are stable to *ca* 470K. This thermal stability, with little evidence of reaction between the two species, is remarkable given the established consensus that deposition of the precursors during thin film growth leads immediately at room temperature to the polyamic acid and that imidisation, while incomplete, has nevertheless commenced even around 400K. Clearly adsorption at the surface inhibits the polyamic acid formation raising the barrier by at least 50kJ mol^{-1}. Indeed it seems to be the case that only few examples of species, which might be identified by STM as an amic acid or related intermediate, can be observed and these tend to be found only for annealing temperatures at which the dominant structures are H-bonded. The white circles in Figure 39b indicate such intermediates. At this annealing temperature they represent 5-10% of potential reaction sites and are located primarily around the periphery of rotational domains. Figure 39c shows one such species, characteristically identified by the bright feature at the reaction site with a comparison of the line profiles of reacted and H-bonded species in Figure 39d. The implication from these observations is that the rate-determining step for reaction between the surface adsorbed molecules is not imidisation, as in the bulk material, but rather the formation of the intermediate, which then proceeds rapidly to the imide or iso-imide, *vide infra*. In a separate publication, we present DFT calculations on a comparison of gas-phase and surface imidisation processes focusing on the characterisation of the intermediate and modifications to the energy landscape introduced by adsorption and by a reaction constrained to two dimensions.

A sub-monolayer of precursors annealed to temperatures above which the H-bonded structures are stable, begins to show evidence of covalent bond formation. Figure 39e shows the results of annealing such a layer to 540K. While remnants of the H-bonded network can be recognised, new chain like features of alternating PTCDA and DATP are also present. Figure 39e also shows that the underlying Au(111) reconstruction has some influence on this process. Molecules show a preference to occupy the *fcc* regions and extended molecular networks, both H-bonded and covalently bonded, follow these *fcc* regions even around the elbows, which remain visible in the images. Finally, when annealing is taken to yet higher temperatures (>570K) complete imidisation takes place and the surface consists of extended chains of alternating species, which we take as evidence of polymer formation, as seen in

Figure 40a. Note that DATP molecules adsorbed on a Au(111) surface in the absence of PTCDA are not stable in UHB at 600K. The underlying gold reconstruction remains visible and apparently unperturbed. There is considerable free space exposed on the surface and small polymer fragments seem to be held together by H bonding. We presume that the formation of longer chains is somewhat limited by the increasingly low diffusion probability as the chain lengths increase. Nevertheless, the polymeric structures formed in this way are highly stable and begin to show signs of decomposition only at temperatures above *ca* 700K. A particularly notable feature is that the polymer chains have both straight linkages and bends at the PTCDA/DATP junctions (Figure 41b). We assign the straight junction to the normal imide product and the bent junction to the iso-imide.

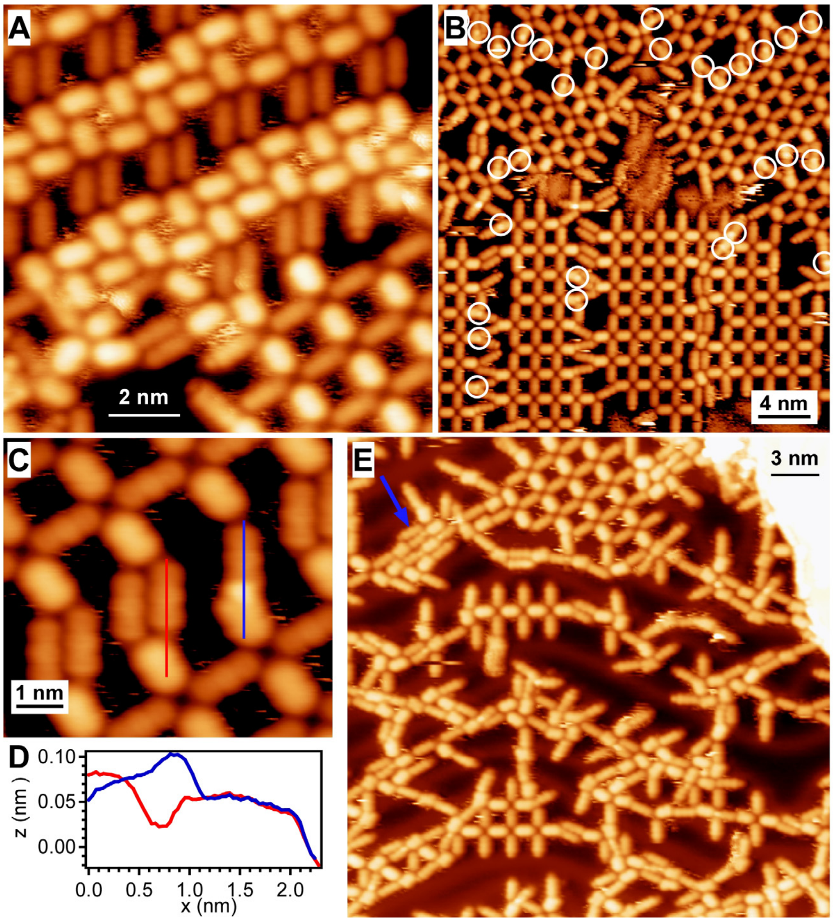

Figure 39: A) STM image (-1.0V; 25pA) of hydrogen bonded structures following deposition of PTCDA and DATP onto Au(111) held at room temperature. PTCDA molecules are the brighter features at this bias voltage. B) STM image (-1.8V; 20pA) showing the three rotational domains of the PTCDA/DATP H-bonded structure at a stoichiometry of 1:1. White open circles denote sites where reaction to the amic acid intermediate has occurred. C) is a magnified image (-1.8V; 20pA) showing the bright central feature associated with the PTCDA/DATP reaction intermediate compared with that of the H-bonded interaction and D) shows the corresponding line profiles. E) STM image (-1.0V; 20pA) indicating the onset of reaction in the region indicated by the arrow. The underlying Au(111) reconstruction is retained and molecules both reacted and unreacted favour occupancy of the *fcc* regions.

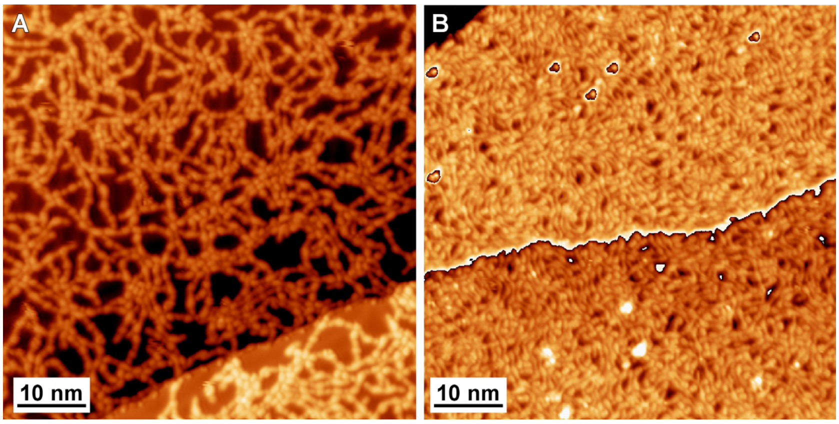

Figure 40: A) STM image (-0.8V; 10pA) of the Au(111) surface following complete imidisation of a sub-monolayer coverage of PTCDA and DATP. B) STM image (-1.2V; 10pA) of high density, monolayer coverage of PTCDA/DATP polyimide. Contrast has been applied to each terrace individually.

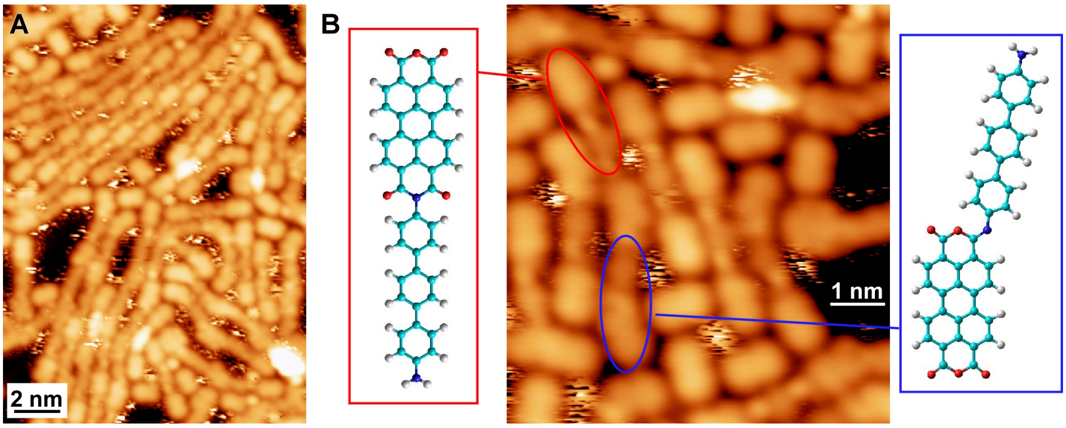

Figure 41: STM images (-1.8V; 50pA) of the PTCDA/DATP polymer A) small ordered region and B) evidence for both straight and bent junctions at the reaction sites assigned to imide and iso-imide reaction products.

We have developed two strategies for producing surfaces with a more complete coverage by the polymer. In addition these strategies produce longer chains and somewhat more order within the polymer monolayer as shown in Figure 41a. The periodicity along the chains is 2.5nm, which compares well with the calculated value of 2.6nm. In those regions, where some order is found, the separation of PI strands is *ca* 0.75nm. Multiple deposition and annealing steps can be employed or alternatively deposition can be carried out at higher temperature. Specifically, if the surface is pre-dosed with PTCDA, the precursor with the higher desorption energy, then DATP is dosed at 600 K, which significantly is above its UHV desorption temperature of *ca* 400 K, a well defined polymer monolayer results. Figure 40b shows such a surface. The DATP molecules presumably have a sufficient lifetime on the surface to diffuse, find a free PTCDA termination and react. However, it is worth noting that DATP doses in these experiments exceeded the equivalent of 5ML indicating a reaction yield well below 100%.

PTCDA/TAPT reaction

The choice of the bifunctional molecules PTCDA and DATP as precursors for the imidisation reaction as described above necessarily results in a network based on a linear polymer. In order to achieve a two dimensionally interlinked polymeric network, similar procedures were followed for the PTCDA/TAPT combination. This amine precursor has three amine groups and, if a 3:2 stoichiometry can be achieved, then a large, fully 2D interconnected network should be achievable. Figure 42 shows such a network following a single deposition and annealing stage. Once again an alternating molecular sequence is observed but as anticipated TAPT provides a three-way link to the PTCDA molecules.

Closed triangular features are common and defects, such as extended closed loops or incomplete network formation, are characterised by TAPT molecules attached only to two rather than three PTCDA molecules. Further investigations are necessary to determine whether this particular deposition created a stoichiometry biased towards the amine. However, a remarkable H-bonded network for this precursor combination, also stable to well above room temperature, showed a highly ordered structure at a stoichiometry of PTCDA:TAPT of 7:4.

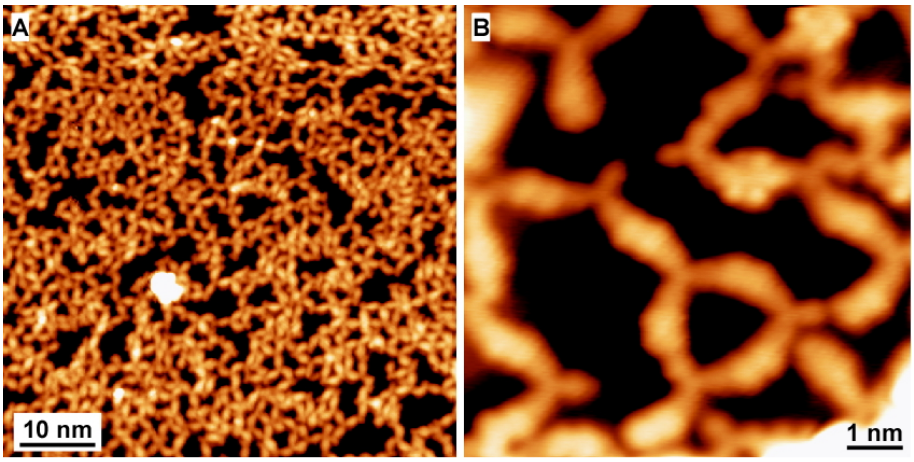

Figure 42: STM images of the polyimide formed by reaction of PTCDA with TAPT on a Au(111) surface after room temperature deposition and annealing to 600K. A) large area (-1.0V; 20pA) and B) small area (-0.8V; 20pA) showing distinctive triangular feature.

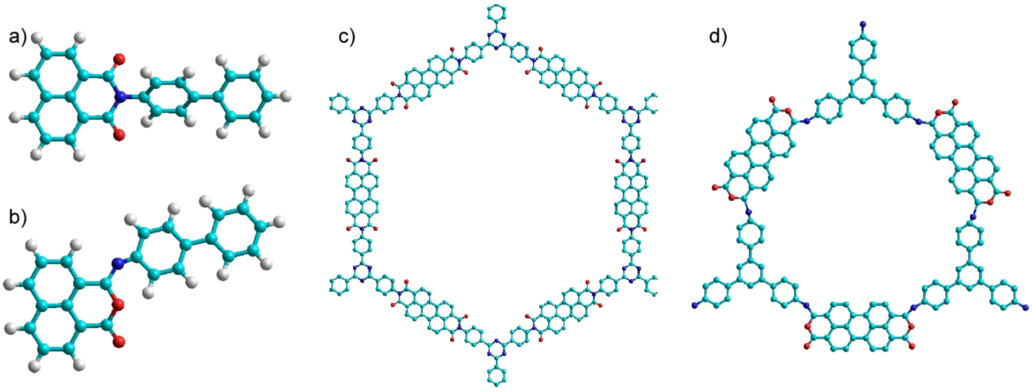

Figure 43: Comparison of the preferred conformation of the a) linear imide or b) bent iso-imide formed by reaction between naphthalene dicarboxylic anhydride and 4-aminobiphenyl. c) Hexagonal and d) triangular closed structures predicted for the reaction of PTCDA and TAPT. The former is based on the imide as reaction product and the latter on the iso-imide.

Imide or iso-imide?

Consideration of the alternative imide or iso-imide products, simplified as N-(4-amino-p-biphenyl)-1,8-naphthalimide and corresponding iso-imide, **a** and **b** respectively of Figure 43, indicates that they should be readily distinguishable by their STM images. The out-of-plane twist of the first phenyl ring in the case of the imide, while that of the iso-imide remains coplanar with the PTCDI, can be clearly seen in the high resolution STM image of Figure 41b. Also, the angle between the PTCDA long axis and the phenyl ring axis of the amine is 0° in the case of the imide but ca 15° for the iso-imide. These two orientations can be recognised in the images of the PTCDA-DATP polyimide and more readily in the triangular features of PTCDA-TAPT. Creation of a closed ring, using imide linkages for PTCDA-DATP, would be expected to lead to the hexagonal arrangement (Figure 43c), whereas the observed triangular structure (Figure 43d) requires iso-imide links. The reaction of an aromatic amine with an aromatic anhydride proceeds by nucleophilic attack of the amine nitrogen atom on one of the carbonyl carbon atoms and, following proton transfer, leads to an amic acid. This is generally considered, both in solution and in vapour deposited films, to be the stable intermediate at room temperature. Films can also be formed by spin coating the polyamic acid or by LB techniques using a polyamic acid, appropriately functionalised as, for example, an ester with a long alkyl chain. The alternative intermediates shown in Scheme 1 are unlikely to be significant in solution but in the solid state and, in particular, constrained in the close vicinity of a surface, the intermediate **b** of Scheme 1 maybe both kinetically preferred, because of the relatively simple transfer of the proton from nitrogen to the adjacent carbonyl oxygen atom, and thermodynamically because this intermediate requires rather little distortion to a "planar" structure compatible with strong adsorption on the gold surface compared with the amic acid, intermediate **a** of Scheme 1, which is more sterically hindered and prefers a non-planar geometry. There are two consequences: firstly, the amic acid is destabilised relative to the bulk or solution reaction and therefore is not observed as a stable intermediate following deposition at low coverage and heating even to 470K. Instead the H-bonded structures are retained and eventual reaction takes place directly to an imidised product. Secondly, the greater stability of the intermediate **b** of scheme 1 drives the system towards the iso-imide rather than the imide compared to the solution and bulk reactions. It is also the case that the iso-imide is planar in the vicinity of the reaction centre, whereas the imide is distorted by a twist of the phenyl ring attached directly to the nitrogen atom relative to the PTCDA plane as indicated in Figure 43. This may also increase the stability of the iso-imide as the final reaction product relative to the imide and provide an explanation of the persistence of the iso-imide on heating to 700K, whereas in polyimide thin films this procedure results in a conversion of iso-imide into the more stable imide.

Conclusions

UHV-STM imaging at 77K has been exploited for the first time to follow the formation of polyimides by the imidisation reaction between precursors PTCDA/DATP and PTCDA/TAPT co-adsorbed at combined coverages up to one monolayer. Remarkably stable, well-ordered H-bonded networks are formed on deposition at room temperature and these remain stable to *ca* 500K. At higher temperatures imidisation is initiated but there is little evidence of the presence of a stable amic acid intermediate. Above 600K complete imidisation takes place and dense monolayers can be created. For both polymers, the anhydride/amine junction in the reaction product is frequently bent, a fact which we ascribe to the presence of iso-imide products. Preference for the iso-imide in the case of the PTCDA/TAPT polyimide gives rise to closed triangular structures in the polymer monolayer. The absence of a stable amic acid intermediate and the stability of iso-imide products, we relate to changes in the reaction mechanism arising from modifications to the energy landscape caused by adsorption on the Au(111) surface.

6.4 Further aspects and outlook

6.4.1 On-surface synthesis of polymeric networks

Three main motivations have led to the very recent – first publications date back less than one year at the time of writing of this thesis – increase in STM studies [212-215, 219-221, 248] of (sub-)monolayer thick polymeric films on single crystal surfaces: First, as evidenced by these studies, chemistry in two dimensions can be markedly different from classical solution-based “textbook” chemistry. While studies on catalytic reactions of small molecules have been performed successfully for decades with non STM-related techniques [145, 249][5], the detailed insight into the surface-confined reactions of large organic molecules is a new field and will certainly be of interest for scientists from various fields for the future. Second, the ability to be able to study larger adsorbates by on-substrate synthesis also opens the door to a completely new field of organic adsorbate systems, removing the upper size limit – imposed by MBE – for adsorbates. Instead of performing the last synthetic step(s) of a large organic molecule in a chemical environment, the (small) reactants are deposited on a single crystal surface, where they react to form the final product. Molecular beam epitaxy is inherently limited to organic molecules that are thermally stable up to a temperature where a sufficiently high vapour pressure is reached in order to allow for an efficient deposition. Several molecules used during this thesis are at the limit of what can still be sublimated intactly. As an example, OBC is probably among the largest polycyclic aromatic molecules that have been vacuum sublimated. Electrospray deposition [250-252] and laser ablation techniques [253] have been used for UHV-deposition of larger molecules but these techniques are limited by the low throughput and the contamination of the sample with solvent. Another alternative deposition route is by brush contact deposition [254, 255], which does however offer very limited control over coverage. A third motivation for the field of two-dimensional chemical synthesis is the possible use of surface-supported polymeric networks as thermally and chemically stable templates. A chemically tailored, surface-supported covalent network (e.g. the one presented in Figure 36) represents an ideal way of nano-templating a crystalline substrate from the bottom-up. Depending on size and symmetry of the covalent network, nano-units of a subsequently deposited molecular/metallic adsorbate – which selectively fills the voids of the polymeric framework – can be obtained. Templated surfaces of this kind might be useful in the production of magnetic nano-islands or nanostructured chemical sensor arrays, hence bearing a large technological potential. However, networks with a well-defined shape and size-distribution of their pores are mandatory for such applications, a requirement which has not been met to date.

Based on the results from our work on polyimides and the presently available literature on covalent surface-supported polymeric networks [248], the requirements for an ideal reaction for template synthesis can be summarized as follows:

- ***One-step reaction*;** The geometry of an intermediate structure (e.g. the amic acid in the polyimide synthesis) can differ considerably from the final product, favouring the formation of “wrong” connections (e.g. small hexagonal pores in TAPT-PTCDA system). Additionally, the adsorption energy of an intermediate product may – due to strain energy associated with conformational adaptation to the surface – be lowered such that the desorption temperature of the polymeric intermediate is below the final reaction temperature. Also, conformational constraints of the reaction intermediate may prevent a completion of the final reaction step or favour an alternative product.
- ***Single reaction product*;** Multiple reaction products (such as the imide and iso-imide) make it impossible to achieve a theoretically predicted structure.
- ***Temperature stability of final product;*** This is a key property to allow for annealing-induced ordering of a subsequently deposited species and/or desorption of non-reacted adsorbates.
- ***Reaction temperature*** well below annealing temperature of substrate, to prevent substrate restructuring during annealing. Also, the reaction temperature should be near the temperature

---

[5] A detailed review on the current state of the art of surface catalysis can be found in a recent issue of *Chemical Society Reviews* (Vol. 37, Issue 10, 2008).

needed for onset of diffusion of the reactants on the substrate. This offers control over the kinetics during polymer synthesis as shown by Weigelt [220].

- ***Reversibility*;** This would allow to ‘cure’ errors in the resulting network structures. However, the reversibility should ideally only be possible for ‘wrong’ connections since if it were also reversible (at the same reaction rate) for ‘correct’ connections, curing of the network would be impossible. Such a difference in reversibility might be favoured by a higher inherent strain of ‘wrong’ network connections. For example, if the theoretically predicted structure should be hexagonal, then a pentagonal/heptagonal pore would be subjected to a larger strain, which lowers the energy barrier for the reverse reaction for these pores but not for the hexagonal unstrained ones. To activate the reverse reaction it might be necessary to dose molecules that had been shed during the reaction (e.g. H_2O in the case of imidization) onto the sample. However, reactions which are reversible in solution might not be reversible on a surface, since partial pressures that can be achieved by dosing a molecule onto a sample under UHV conditions are several orders of magnitude smaller compared to the ones in solution.
- ***Tuneability of network*;** This can be achieved if the reactants are easily synthesized and exist in a large variety allowing for a variation of size and symmetry of the polymeric network.
- ***Product chemically inert*** (with respect to metal and organic adsorbates); This is essential for the use of polymeric network as templates.

In combination with optimized preparation protocols – involving e.g. sequential annealing/deposition of small quantities of the reactants – the abovementioned points should serve as evaluation guidelines for chemical reactions that might be useful for the synthesis of highly ordered polymeric networks in two dimensions.

6.4.2 Bottom-up fabrication of chemically tailored graphene nanostructures

On-surface synthesis as a way to circumvent problems with other deposition techniques may also be of relevance for research on graphene [256] nanostructures, an area of research which has seen an enormous increase of interest in the last few years. While the electronic, magnetic and optical properties [257] of graphene are unique and potentially useful in future devices, there is at the present stage no easy-to-handle method for large-scale processing and tailoring of individual sheets of graphene. On the other hand, a large range of chemically tailored nanographene flakes can be synthesized by chemical routes [130]. However, highly efficient intramolecular π-π stacking between these planar nanographenes renders them practically insoluble in commonly used organic solvents [130]. The strong π-π stacking also raises the sublimation temperature above the temperature for thermal decomposition, making it impossible to bring these structures onto a surface by evaporation[6]. This problem has been circumvented by using laser ablation methods [253] which is however only efficient for laboratory purposes and not a solution for possible technical implementations. Alternatively, graphene flakes may be rendered soluble by adding appropriate side chains at the edges [130] allowing a deposition from solution. However, it is known that the geometric shape (and possibly also the functionalization) of the edges directly influences the electronic properties of graphene [258, 259]. As for polymeric networks, the on-surface synthesis route would be a powerful alternative for the bottom-up creation of nanographene structures. On surface-synthesis of planar PAH has been studied to some extent prior to the ‘graphene-era’ [260, 261], however, no detailed STM investigations of these reactions have been performed.

A first successful proof-of-principle study along these synthesis lines has been performed on cyclohexaphenylene [262] (CHP; Figure 44d bottom). Steric hindrance between the central hydrogen atoms renders this PAH strongly nonplanar, decreasing π-π stacking interactions. CHP can be planarized to the triangular nanographene Tribenzo[a,g,m]coronene (Figure 44g bottom) by oxidative cyclodehydrogenation [130] involving a so-called intramolecular Scholl reaction [263].

---

[6] Empirically, the upper size limit for planar polycyclic aromatic hydrocarbons that can be evaporated is found to be set at about 15 fused aromatic rings, such as e.g. dibenzo[hi,uv]phenanthro[3,4,5,6-b,c,d,e,f]ovalene.

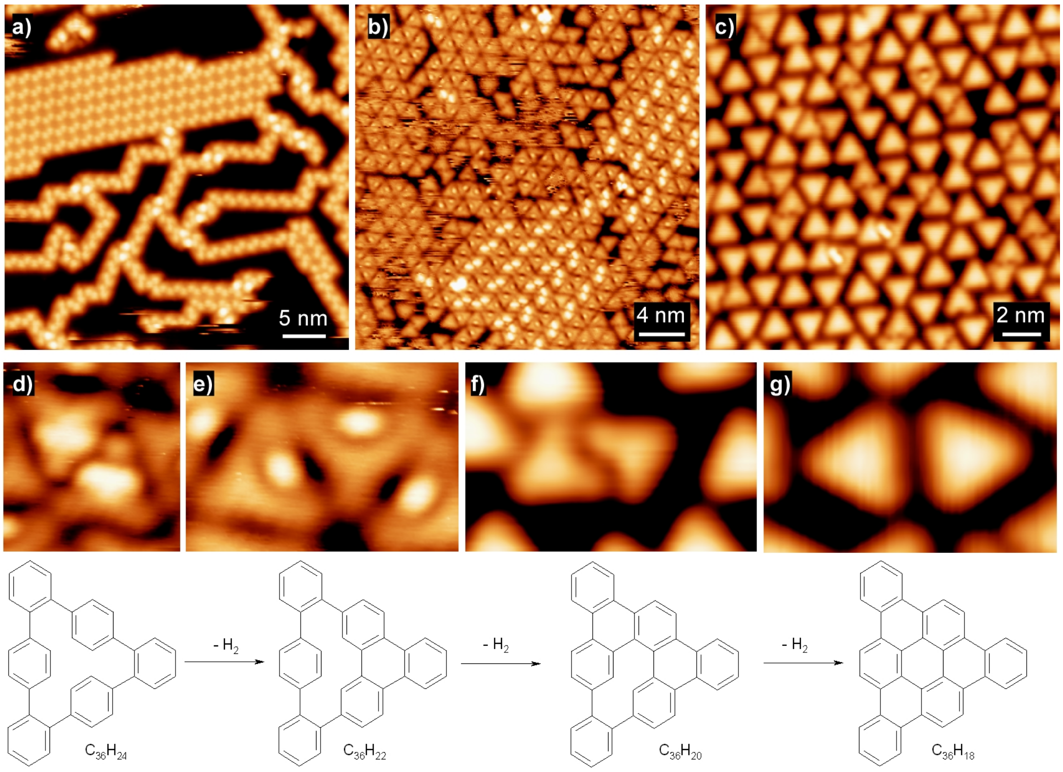

Figure 44: STM study of CHP. (a) Self-assembled structures after deposition at RT. (b) Co-existing CHP, intermediates and final product after annealing at 450 K. (c) Sample annealed at 470 K showing mainly the final triangular PAH. (d) to (g) STM images (top) and geometrical structures (bottom) of stepwise cyclodehydrogenated CHP.

As shown in Figure 44, the reaction can also be thermally initiated on Cu(111). As illustrated in Figsures 44d-g, the reaction does not proceed in one step but involves two stable reaction intermediates. Interestingly, the temperatures needed for thermally activated on-surface cyclodehydrogenation (~470 K) are well below corresponding values for other thermal cyclodehydrogenation routes (~1250 K) [264], suggesting that the substrate acts as a catalyst. The first intermediate product is shown in Figure 44e. It is obtained after one C-C coupling reaction, while the phenyl ring opposite to this bond has not reacted yet. Due to steric hindrance, this non-reacted phenyl ring is forced out of the plane of the locally planarized molecule which is imaged as a clearly distinguishable protrusion over one molecular side in STM. At the present stage, the second intermediate cannot be clearly assigned to a chemical structure. A possible chemical structure is shown in the bottom row of Figure 44f. Alternative structures involve sp^3-bonded carbon at the reaction sites, i.e. that hydrogen has not been shed at this reaction stage. These reaction intermediates self-assemble into pairs as shown in Figure 44f. While this intermediate product already has an overall triangular shape, only two sides are straight while the sides with which the pairs are facing each other appear to be bent inwards. An ongoing theoretical study of the reaction will clarify the structures of these reaction intermediates [265].

The stepwise planarization of CHP can also be evidenced by XPD. The anisotropy of the C1s diffraction pattern shows a marked increase as a function of annealing temperature (Figure 45). The final pattern is nearly identical to the corresponding pattern measured for HBC (Figure 45e) exemplifying the planarity of the final product. XPD hence offers a way to qualitatively analyze the planarity of surface-synthesized graphene-like structures, as illustrated at this example.

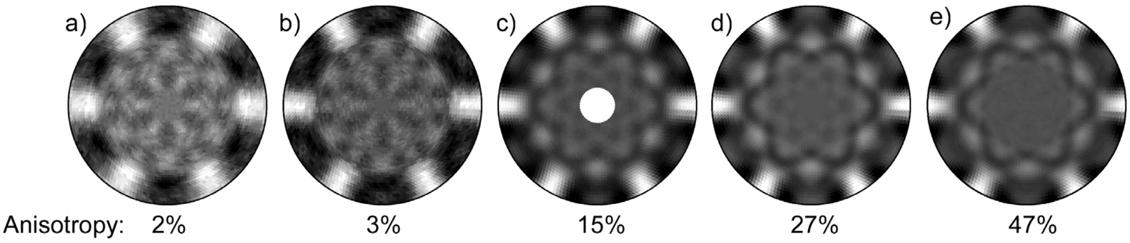

Figure 45: C1s-XPD of CHP after annealing at different temperatures (a) to (d), illustrating the increase of anisotropy with stepwise planarization. Approximate annealing temperatures: (a) RT (no annealing) (b) 400 K (c) 470 K (d) 570 K. (e) C1s-XPD of planar HBC shown for comparison. A photon energy of 920eV has been used for all samples.

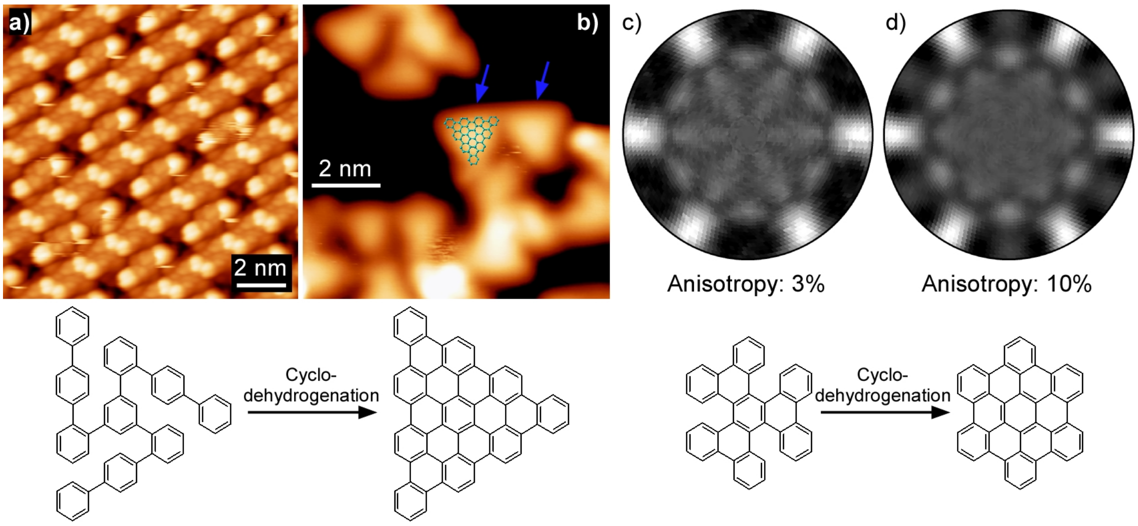

Figure 46: Cyclodehydrogenation of nanographene precursors on Cu(111). (a) Self-assembled, densely-packed monolayer of TPBPB after deposition at RT (b) After annealing to 570 K tnHBC is observed. Blue arrows denote triangular flakes ascribed to the final reaction product. (c) C1s-XPD (photon energy 920 eV) of HBTP after deposition at RT and after annealing at RT (d). The marked increase in anisotropy is ascribed to a partial planarization of the molecule upon annealing to 550 K.

The surface-supported cyclodehydrogenation of CHP has offered unpreceeded insight into the Scholl reaction and paved the way for on-surface synthesis of nano-graphene from chemically tailored precursors. Figures 46 a&b show the applicability of this concept to an even larger PAH. It is important to note, that the final planar triangular nanographene benzo[o]bistriphenyleno[2,1,12,11-efghi:2',1',12',11'-uvabc]ovalene (tnHBC) [266] cannot be deposited intactly by MBE, while the surface-supported cyclydehydrogenation of its precursor – 1,3,5-tris(2'-(4''-phenyl)biphenyl)benzene [266] (TPBPB) – allows for the deposition of this substance on Cu(111). However, as can be seen in Figure 46b, there appear to be alternative reaction products and also intermolecular reactions might have occurred during annealing. Compared to CHP, the cyclodehydrogenation reaction yield is much lower for this polyphenyl. This can be rationalized by the cyclic framework of CHP which conformationally constrains the individual phenyl rings while in TPBPB each phenyl ring has more conformational degrees of freedom, resulting in a larger number of possible inter- and intramolecular Scholl reactions. It should be noted that the intermolecular π-stacking of the polyphenyl precursors (CHP and TPBPB) is much lower than for their planarized counterparts[7]. This considerably increases the solubility of the non-cyclodehydrogenated precursors, making them more processeable. Even very large polyphenyl molecules (e.g. extended linear polyphenyl ribbons) can be dispersed in

---

[7] The lowering of the packing energy results in a reduction of the temperature needed for sublimation. While TPBPB can be sublimated from resistively heated quartz crucibles held at 500K in UHV, the decomposition tempertature of tnHBC (>700K) is lower than its sublimation temperature.

dichloroethane, allowing for a surface deposition through drop casting or spin coating techniques. Subsequent thermally induced surface-supported cyclodehydrogenation may be a possible way towards chemically-tailored easy-to-handle nanographene ribbons.

The surface-supported synthesis of HBC by cyclodehydrogenation of hexabenzotriphenylene (HBTP) [161] has also been studied by C1s-XPD (Figures 46 c&d). A clear increase of anisotropy upon annealing to 550 K and a close resemblance between the resulting C1s-XPD (Figure 45d) and the corresponding pattern produced by HBC (Figure 45e) is evidenced, suggesting that planarization of HBTP is also possible on Cu(111). In this case, the driving force for the Scholl reaction is the strain energy of the bay region.

These two additional examples of surface-supported cyclodehydrogenation show that the intramolecular Scholl-reaction will work on Cu(111) for a wide variety of PAH, not crucially depending on the exact geometrical properties of the reactant. Additionally, intermolecular Scholl reactions of small PAHs precursors might be used for the bottom-up creation of surface-supported graphene structures.

7 Ordering of encaged units

7.1 Introduction

As shown in the previous chapters, adsorbates can form structures in two-dimensions that show order of different types, such as long-range ordered supramolecular structures (Chapters 4 and 5), local order with respect to the substrate (Chapter 3) or partial local order of supramolecular units (Chapter 6).

In this chapter a completely different type of ordering, affecting endohedral (encaged) units is demonstrated in two dimensions. It is shown, that apart from intermolecular order, intramolecular ordering can also be achieved by self-assembly in two dimensions (Figure 46).

The inter- and intramolecular ordering of monolayers of the trimetallic nitride endohedral fullerene $Dy_3N@C_{80}$ on Cu(111) is analyzed by a combined STM and XPD study. As already shown in Chapter 3, these techniques yield complementary information, allowing for a complete determination of the intermolecular ordering (STM) and orientation of the fullerene cage and ordering of the endohedral nitrogen atom (XPD). Resonant X-ray photoelectron diffraction is used to gain information on the ordering of the endohedral dysprosium atoms which are shown to be ordered within the cage.

With the availability of an increasing variety of endohedral clusters – in cages of different size and symmetry [267] – ranging from single-atom [268], metal-nitride [269, 270] to metal-carbide clusters [271, 272], it might be possible to tune the ordering of endohedral units in two dimensions (Figure 47) by changing the structure of the cage – which affects intermolecular and cage-substrate interactions – or the endohedral unit itself, which alters the interaction of the latter with the cage and hence the interaction of the endohedral unit with the substrate that is mediated by the cage. Ordered arrays of endohedral units might be used in memory storage devices, provided that the endohedral units can be switched between different stable configurations by an external stimulus such as an applied electric or magnetic field.

Placing encaged units on a substrate is not only possible for endohedral fullerenes, the same approach might also be used for systems built on the basis of concepts derived from molecular encapsulation [273].

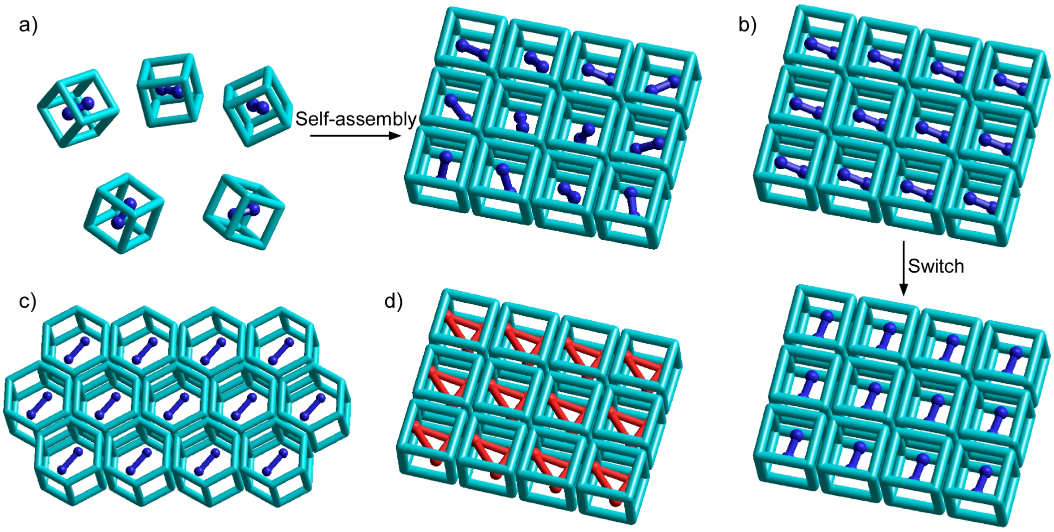

Figure 47: Ordering of encaged units through self-assembly into structures with ordered cages and disordered (a) or ordered (b) endohedral units. Arrays of ordered endohedral units might be switched by an external stimulus (b), exemplifying their potential use in data storage media. Ordering of the encaged units can be tuned through modifications of the cage (c) or the endohedral units itself (d).

7.2 Looking inside an endofullerene: Inter- and intramolecular ordering of Dy3N@C80 on Cu(111)

M. Treier[1]*, P. Ruffieux*[1]*, L. Dunsch*[2]*, T. Greber*[3]*, R. Fasel*[1]

[1] EMPA, Swiss Federal Laboratories for Materials Testing and Research, nanotech@surfaces laboratory, CH-3602 Thun, Switzerland

[2] Leibniz Institute for Solid State and Materials Research, Dresden, Germany

[3] Physics Institute, University of Zurich, 8057 Zurich, Switzerland

to be submitted

Abstract

The adsorption behavior of the trimetallic nitride endohedral fullerene $Dy_3N@C_{80}$ on Cu(111) has been studied by scanning tunneling microscopy (STM) and both resonant and standard X-ray photoelectron diffraction (XPD). By a combination of the two techniques, the inter- (STM) and intramolecular (XPD) ordering has been determined. $Dy_3N@C_{80}$ is found to form ordered islands consisting of domains of equally oriented molecules. As for C_{60} on the same substrate, the cage is facing with a 6-membered ring towards the surface which is however tilted for C_{80}. The endohedral nitrogen atom remains at a position close to the geometrical center of the cage. Resonant XPD shows that the Dy atoms within the cage are ordered.

Metal-containing endohedral fullerenes have attracted great interest over the last decade due to their unique electronic properties associated with the charge transfer from the endohedral metal complex to the carbon cage. Endofullerenes exhibit a variety of other novel properties such as peculiar redox- and electrochemical behavior, luminescence and nonlinear optical response [268]. Furthermore, endofullerenes represent an interesting class of materials since they offer the possibility to study and possibly manipulate small clusters of endohedral atoms which might for example be used in future memory storage devices. Due to the comparably high production yields that can be achieved, research on trimetallic nitride (TNT) endohedral fullerenes [269] has increased in recent years [269, 274-277]. TNT endohedral fullerenes have been shown to posses an endohedral ordering in condensed phases such as co-crystals [276, 278]. They have also been shown to posses unique magnetic properties [277, 279], motivating their application in future memory storage devices. For such applications, ordered arrays of endohedral units are however required, with the possibility to order the endohedral units to store information. The ordering of TNT endofullerenes on surfaces has been analyzed previously by Scanning tunneling microscopy (STM) [280-282]. However, these studies have not addressed the issue of endohedral ordering in the adsorbed state since this information is not accessible by STM studies alone. On the other hand, the endohedral ordering of single-atom endohedral metallofullerenes has been studied by X-ray standing wave techniques [283, 284], without however addressing the ordering of the cage.

In this letter we present a detailed study of the adsorption behavior of (sub-)monolayers of the trimetallic nitride endohedral fullerene $Dy_3N@C_{80}$ [275] on Cu(111). We show that the combination of STM and both standard and resonant X-ray photoelectron diffraction (XPD) allows for a determination of the inter- and intramolecular ordering. We find that $Dy_3N@C_{80}$ forms an ordered superstructure on this template, with both the cage and the endohedral unit being ordered with respect to the substrate.

Angle-scanned X-ray photoelectron diffraction experiments were performed at the NearNode-endstation of the X11MA-SIM beamline at the Swiss Light Source. Low temperature STM (LT-STM) measurements were conducted using an Omicron LT-STM. Both systems were operated at ultra high vacuum conditions with base pressure below 2×10^{-10} mbar. The substrate has been cleaned by standard Ar^+-ion sputtering / annealing cycles prior to deposition of the endofullerenes which have been deposited from resistively heated quartz / diamond-like carbon coated steel crucibles held at about 770K onto the sample which was held at room temperature. XPD has been performed at room temperature while STM data was acquired at 77K.

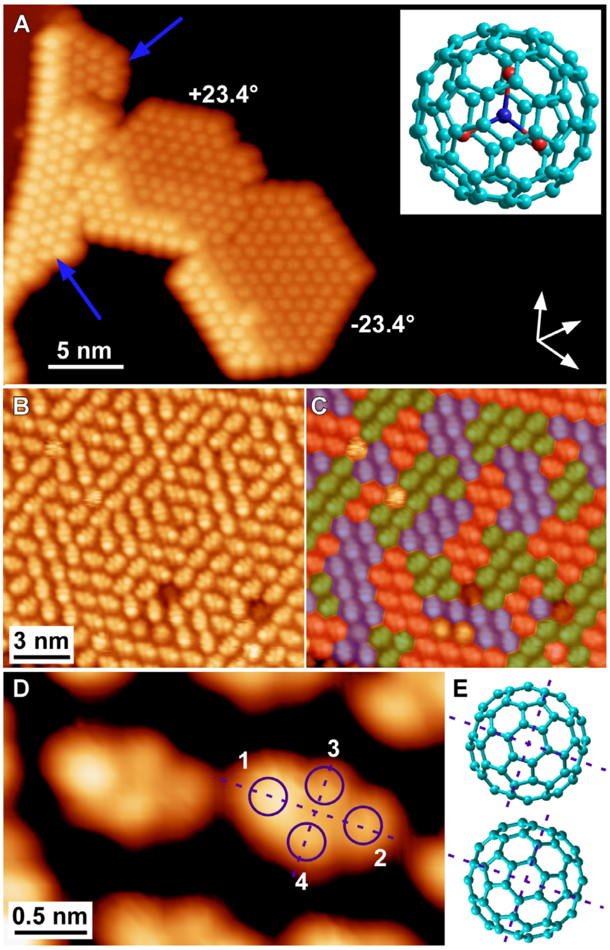

Figure 48: STM images of $Dy_3N@C_{80}$ on Cu(111). (A) Overview image showing the local correlation between the step edge direction and the overlayer structure. Blue arrows point to small patches of adsorbates which adopt a superstructure different from the dominating $\sqrt{19}$ superstructure. (B) Intramolecular contrast resolved STM image of a +23.4° island showing the formation of small domains of equally oriented molecules within an island. (C) Visualization of domains; colored STM image of the area shown in (B). (D) High resolution STM image of two molecules, showing intramolecular contrast. Four protrusions per molecule can be identified. (E) Suggested model of C_{80} cage compatible with the symmetry of the intramolecular features from (D). Dashed lines correspond to the symmetry elements from (D). (Scanning parameters: (A) 80pA, -1.8V (B,C,D) 0.3nA, -0.1V).

STM measurements [192] of submonolayers of $Dy_3N@C_{80}$ on Cu(111) show that islands of the adsorbate grow out from step edges on both the lower and upper terrace adjacent to the step. Locally, the orientation of the superstructures follows the orientation of the step edges as shown in Figure 48a. However, low energy electron diffraction shows that at higher coverage (close to a complete monolayer), a $(\sqrt{19}\times\sqrt{19})R\pm23.4°$ dominates with no other superstructures spanning over dimensions to be visible in LEED. The nearest neighbor distances in the other superstructures are – within the measurement error of STM - equal to the ones of 1.1 nm within the long-range ordered superstructure. High resolution STM images show that within islands of the $\sqrt{19}$ superstructure, three rotational equivalent molecular orientations are found. Equally oriented molecules form small domains of typically 5-15 molecules within larger islands as shown in Figures 48b&c. A statistical analysis of 1256 adsorbates showed that 53% of the nearest neighbors of a given molecule have the same orientation while the rest is oriented in either of the two other orientations. Adsorbates on the border of islands and on step edges have not been included in the analysis.

A high resolution image, with discernable intramolecular structure is shown in Figure 48d. Four protrusions can be discerned per molecule. While the protrusions labeled 3 and 4 approximately have the same apparent height, this is not the case for protrusions 1 and 2, with protrusion 1 appearing 0.2-0.3Å higher. The particular intramolecular contrast cannot be readily related to a molecular orbital or elements of the cage. However, it is possible to derive potential adsorption orientations of the cage based on symmetry considerations. The molecule appears to be symmetric with respect to the dashed lines passing through maxima 1 and 2 (Figure 48d) while the difference in apparent height can be ascribed to a rotation of the cage around the axis represented by the dashed line passing through maxima 3 and 4. Such a rotation would correspond to a tilt of the cage with respect to a highly symmetric adsorption geometry. Two adsorption geometries compatible with these symmetry considerations are given in Figure 48e with the cage facing toward the surface with a 6-membered ring in both cases. Since electronic and geometric effects cannot be clearly separated by STM, a quantitative analysis of this tilt and unambiguous determination of the adsorption geometry is not possible by STM alone. We have therefore complemented the STM results by an XPD study, a combination of techniques which has previously shown to accurately allow determination of the three-dimensional orientation of large organic adsorbates [285].

N1s- and C1s-XPD patterns are shown in Figures 49a&b. Due to the single photoelectron emitter per molecule, the N1s photoelectron diffraction pattern (Figure 49a) is highly anisotropic (~20%) and therefore it is possible to measure clearly distinguishable diffraction features even at this very low nitrogen concentration of only about ~1 atom/nm^2 within the $Dy_3N@C_{80}$ monolayer. The C1s-XPD pattern (Figure 49b) of a monolayer of $Dy_3N@C_{80}$ bears some resemblance to the corresponding pattern produced by a monolayer of C_{60} on the same substrate [*80*]. However, the pattern produced by the C_{80} cage is rotated azimuthally by 30° compared to the case of C_{60}, directly indicting that the adsorption orientations must be different for this type of fullerenes. The large number of inequivalent emitter-scatterer directions is directly reflected in the broad shape of the maxima.

Single scattering cluster (SSC) simulations [*75*] have been used to find the molecular orientation yielding the best agreement with experiment and hence the lowest reliability factor (*R*-factor) [102]. Backscattering from substrate atoms has not been considered since the backscattering yield is very low within the kinetic energy range used for this work (> 400 eV). Partial wave phase shifts have been computed within a muffin-tin formalism [*48*].

From the C1s-XPD, it is found that similar to C_{60}, the C_{80} cage is facing towards the surface with a 6-membered ring. However, in the present case, the exact orientation of the 6-membered ring in C_{80} differs from the one determined for C_{60}. As mentioned in the previous section, STM stipulates an out-of-plane rotation of the cage which is confirmed by XPD. Figure 49g shows an *R*-factor map as a function of cage rotation around the surface normal and out-of-plane tilt. The orientational angles of the cage (Figures 49e&f) are defined as follows. A cage sitting on a 6-membered ring is used as a starting point. The C-C bonds of the 6-membered ring are aligned with the substrate <1 1 0> directions. The cage is then first tilted by an angle ψ (which is the angle between the plane of the bottommost 6-membered ring and the substrate plane as illustrated in Figure 49e) and then rotated around the substrate (111) axis by an angle ϕ (Figure 49f). The best fit with experiment is obtained for a tilt angle ψ of the 6-membered ring of 3°±5° with respect to the (111) plane of the substrate and an azimuthal angle $\phi = 4°\pm4°$ which compares well with the STM result from which ϕ can be estimated to about 6°±6°. Only the cage orientation shown in the bottom part of Figure 47e is compatible with XPD. Based on this cage orientation, nearest neighbors within the $\sqrt{19}$ superstructure are found to approximately be facing each other with 5-6bonds (along the 'long' axis of the molecule in Figure 48d) and 566-edges (along the directions 60° to this axis) respectively. The alternative model derived from STM (upper part of Figure 48e) can be excluded. It should be noted that the *R*-factor has a shallow minimum around this position which is reflected in the relatively large error associated with the cage orientation. The cage orientation has also been determined independently based on the N1s-XPD and the same orientational angles were found to give the lowest *R*-factor, suggesting that the actual error is smaller than the value quoted above. The position of the endohedral nitrogen atom in the direction orthogonal to the surface has been determined by SSC. It is found that the nitrogen atom remains at a position close to the centre of the C_{80}-cage also in the adsorbed state. The variation in *R*-factor as a function of nitrogen position is shown in Figure 48h. It is clearly seen, that a pronounced minimum is found for a position of the nitrogen atom at 0.1±0.2Å below the geometrical centre of the cage[8]. As can be seen by comparing Figures 49a&c and 49b&d respectively, the agreement between simulated and measured diffraction patterns is excellent for both N1s and C1s patterns.

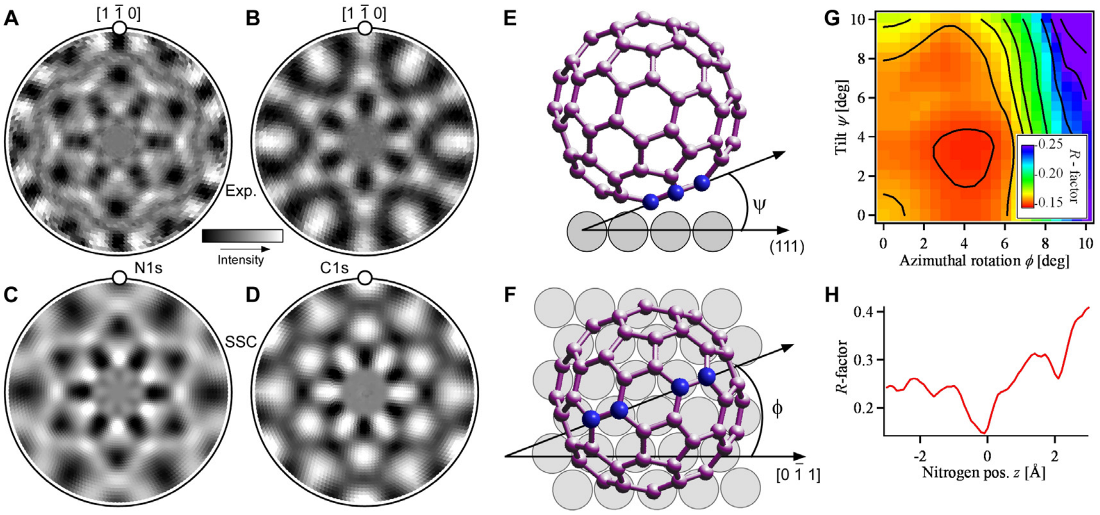

Figure 49: Synchrotron radiation (880eV) XPD study of 1ML of $Dy_3N@C_{80}$ on Cu(111). (A) Experimental N1s-XPD (B) Experimental C1s-XPD (C) Best-fit N1s-SSC (D) Best-fit C1s-SSC (E&F) Definition of angles for orientation of cage used in (G). Blue atoms highlight the units of the cage that are used to define the axis for the angular rotations. (G) *R*-factor as a function of cage orientation. (H) *R*-factor as a function of nitrogen position (with respect to the centre of the cage).

While C1s and N1s photoelectron diffraction pattern of excellent quality could be measured by standard synchrotron-radiation angle-scanned XPD, a strongly anisotropic background and low peak intensity prevented a similar recording of Dy4d patterns. The large number of final states leads to a broadening of the Dy4d peak resulting in a low peak-to-background ratio. In conjunction with the strongly anisotropic secondary electron background (due to the close-lying Cu3s photoelectron peak) this prevents a clear assignment of diffraction features to Dy4d photoelectrons. In order to increase the peak-to-background ratio resonant x-ray photoelectron diffraction (rXPD) [*96, 97*] has been used. At a photon energy of 1291.5eV, Dy-LMM-Auger electron emission is strongly enhanced (Figure 50a). The peak-to-background ratio can this way be improved by more than one order of magnitude, hence considerably improving the counting statistics.

Figure 50b shows a rXPD pattern recorded at a photon energy of 1291.5eV on the strongest Auger feature (central dashed line in Figure 50a). For the determination of the Auger electron intensity, a spectral background has been subtracted in a way to minimize the threefold symmetry of the pattern (three-fold symmetric contributions are due to inelastic photoelectrons from the bulk) and maximizing the six-fold symmetric part (which is due to the adsorbate signal) at the same time (method described in Chapter 2.5.2). Since the pattern does exhibit a clear anisotropy of 4%, this already confirms an ordering of the endohedral unit in the adsorbed state. A fast, continuous rotational motion of the endohedral board – which has been suggested for the trimetallic nitride endofullerene $Sc_3N@C_{80}$ [286] – can thus be excluded for the adsorbed molecule at room temperature.

---

[8] It should be noted that no prominent diffraction features associated with the endohedral dysprosium atoms are visible in the N1s-difraction pattern which is dominated by contributions from the carbon cage. In the SSC simulations, scattering from Dy atoms has not been taken into account.

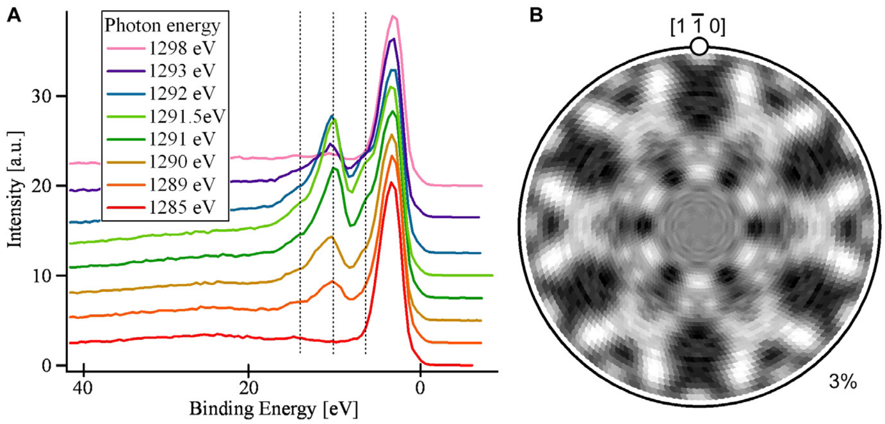

Figure 50: rXPD of Dy-MNN Auger lines. (A) Resonant enhancement of Auger lines (dotted lines) as a function of photon energy. (B) Dy-MNN-rXPD of 1ML $Dy_3N@C_{80}$ on Cu(111), recorded at a photon energy of 1291.5eV. The quoted percentage corresponds to the anisotropy of the pattern.

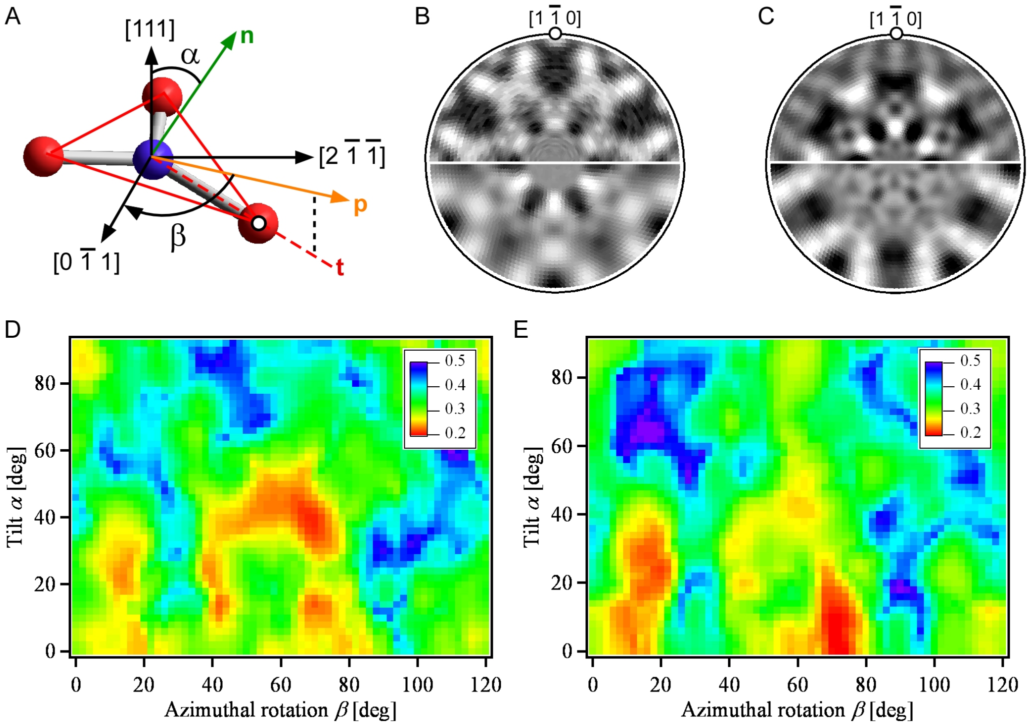

Figure 51: SSC simulations for rXPD of Dy-MNN Auger lines. (A) Definition of orientational angles of the endohedral Dy_3N unit used in the R-factor analysis. **n** (green line) is the orthogonal to the plane spanned by the Dy_3N unit (red triangle). **p** (orange line) is the projection of the red dashed line (N-Dy bond) onto the (111) plane. (B) Experimental Dy-MNN rXPD (upper half) and simulated pattern based on the orientation of the endohedral unit from XRD. (C) Best-fit SSC for a planar (upper half) resp. pyramidal (lower half) endohedral unit. (D) (E) *R*-factor maps as a function of α and β for planar (D) and pyramidal (E) endohedral unit.

To investigate on the orientation of the endohedral Dy_3N unit, the experimental Dy-rXPD pattern has been compared to SSC simulations. SSC simulations have been performed assuming an s-wave character of the outgoing photoelectron wave which is a good approximation at this high kinetic energy of about 1280eV [287, 288][9]. Figure 51b shows a simulated SSC pattern based on the dominating geometry of the endohedral unit as determined from the co-crystal where N-Dy bonds are pointing towards the center of 6-membered rings of the cage. It has been assumed that the endohedral

---

[9] No significant changes in shape of the simulated diffraction pattern have been observed for p- or d-waves.

unit is fixed to the cage and individual SSC patterns corresponding to adsorption on each of the 6-membered rings of the cage have been summed up for the pattern shown in the figure. This leads to a pattern which is clearly anti-correlated to the experimental pattern in the outer part of the pattern implying that this adsorption configuration can be excluded.

For further simulations, both planar and pyramidal endohedral units have been used. A slight deviation from planarity has been suggested in the literature [278], however, the deviation from planarity is smaller (<0.1 Å) than for other trimetallic nitride endohedral fullerenes [276] and beyond the precision of XPD. The orientation of the cage as determined from C1s-XPD and the nitrogen position from N1s-XPD have been kept fixed during refinement of the orientation of the endohedral unit. The orientational angles of the endohedral unit as optimized in the SSC simulations are shown in Figure 51a. A Dy_3N which has one N-Dy bond (respectively its projection **p** onto the (111) surface of the substrate in the case of the pyramidal unit) along the substrates [-2 1 1] axis (i.e. red axis **t** along [-2 1 1] in Figure S1a) is used as a starting cluster. This unit is then rotated by an angle β around the surface normal and then tilted by an angle α by rotating the unit around the [1 -1 0] axis.

Figure 51 summarizes the results from the SSC simulations. Neither the assumption of a completely planar nor a slightly pyramidal (Dysprosium atoms 0.5 Å below the Nitrogen atom) unit results in a satisfying agreement of the simulated pattern with experiment when the orientation of the endohedral unit (Figure 51a) is left as a free parameter. Taking into account the large error associated with the orientation of the carbon cage (and the intrinsic measurement error due to substrate orientation determination) and the large number of configurational parameters[10] for the endohedral unit, it has to be concluded that it is not possible to reliably determine the orientation of the endohedral unit by means of SSC simulations. As can be seen by comparing the *R*-factor maps in Figures 50d&e, a small variation in planarity can considerably change the orientational parameters for the endohedral unit. While the azimuthal orientation β is only weakly affect in this case, the tilt angle α changes from 38° (planar) to 8° (pyramidal unit), exemplifying, that the geometry cannot be determined in a self-consistent way . The lowest *R*-factor in the pyramidal case is only 6% smaller than the corresponding value for the planar unit, with both *R*-factors being more than 30% larger compared to the best-fit *R*-factors for the C1s and N1s patterns. Neither of the two cases is in very good agreement with the experimental pattern with each of the simulations only satisfyingly reproducing part of the features from experiment. Neither of the two geometries corresponding to these simulations can therefore be expected to correspond to the true geometry of this endohedral fullerene in the adsorbed state. It should be noted that due to the non-alignment between the mirror plane of the cage with the [0 -1 1] substrate direction, each orientation of the endohedral unit is twelve-fold degenerate. It should further be noted that a potential pyramidalization of the endohedral unit should be accompanied by a deformation of the cage which can however not be reliably determined from the SSC analysis form the C1s diffraction data[11]. Since there are also several co-existing orientations of the endohedral unit found in the co-crystal [278] it can be assumed that this will also be the case for adsorption on Cu(111) further increasing the configuration space for the endohedral unit.

The agreement with experiment cannot be improved significantly by rotating the endohedral unit around the t-axis (Figure 51a). The large number of parameters that are potentially altered upon adsorption – and would therefore have to be optimized in an SSC analysis – hence makes it impossible to completely determine the orientation of the endohedral unit by SSC. The present adsorption system hence appears to be beyond the maximum limit of what can still be reliably determined by an XPD-SSC combination. It might be possible to obtain further information on the ordering of the endohedral unit by a closer inspection of the outermost diffraction features in the N1s-XPD which are less well reproduced than the rest of the pattern by an SSC simulations based on scattering from cage atoms only. However, the problem of the large parameter space for the endohedral unit prevails which also means that using MSC simulations is not expected to overcome the inherent limitation in this system. For the same reason it will also be difficult to reliably determine the orientation of the endohedral unit

---

[10] Configurational parameters are: Euler angles of the endohedral unit, deviations from planarity, variation in bond length (both N-Dy and C-Dy), displacement of endohedral unit with respect to the center of the cage, deformation of the cage (due to C-Dy bonds) etc.

[11] The broad minimum found for the cage orientation (Figure 48f) suggests that the simultaneous optimization of yet another parameter (describing a possible cage deformation) cannot be expected to yield quantitatively meaningful results.

by DFT due to the large size of the system that would have to be studied and the low number of restrictions that could be placed onto that system, rendering the calculations computationally very costly, especially since several (almost) iso-energetic minima would have to be determined. It can however be concluded from the present data that the endohedral unit shows some order within the cage with the complete geometry of the endohedral unit remaining to be determined by other methods. It has also become clear that there should be more than only one possible orientation of the endohedral unit.

With the large variety of currently available multi-atom endohedral fullerenes [270], the adsorption of such endohedral fullerenes on single crystal surfaces provides a means to create ordered arrays of endohedral, decoupled clusters which can then be characterized and – as a possibility for future experiments –oriented by application of external fields.

In summary, we have shown that the endohedral fullerene $Dy_3N@C_{80}$ adsorbs on Cu(111) in a way that at monolayer coverage, both the cage and the endohedral unit are ordered. Within islands, domains of equally oriented molecules are found. The C_{80} cage faces towards the surface with a 6-memebered ring whose plane is slightly tilted with respect to the substrate. The nitrogen remains at the center of the cage with the dysprosium atoms being ordered within the cage.

8 Conclusions and outlook

It has been the focus of this thesis to explore new conceptual approaches towards the production of ordered organic nanostructures from the bottom-up on single crystal metal surfaces. In this chapter the main results are summarized and implications for future work and usability of these approaches are briefly outlined.

Growing nanostructures at specific sites on a substrate is a key requirement for their use in functional devices. A first step towards this goal has been demonstrated using a templated substrate, where the first adsorbates selectively decorate specific sites from which larger structures might be grown. The site-selective anchoring of a prototypical building block on a naturally templated substrate has been shown at the example of HBC adsorbed on Au(11 12 12). A tilted adsorption configuration across kinks and steps is found for this nanographene molecule.

As a second new approach, the use of aromatic interaction in the rational design of supramolecular architectures has been shown. The self-assembly of the nonplanar PAH cHBC on Cu(111) is governed by lateral aromatic interactions with the overlap between the π-orbitals of nearest neighbours bearing potential for supramolecular electronics applications.

On-surface covalent interlinking of molecular building-blocks as a further design principle for supramolecular architectures has been established at the example of imidization. The condensation reaction between amines and anhydrides, resulting in extended polyimide oligomers is found to proceed also if the two reactants are confined to two dimensions on the Au(111) surface. However, the amic acid reaction intermediate is only formed at temperatures considerably higher compared to the equivalent reaction in solution. While it was not possible to form regular covalent networks based on this approach, the geometric properties of the polymeric structures could be tuned by modifying the geometry of the reactants.

A novel conceptual approach to the formation of organic semiconductor nanostructures has been established which is based on a subtle energy balance between homo- and heteromolecular interactions of suitably designed co-adsorbates. A range of low-dimensional nanostructures of the organic semiconductor PTCDA can be created by using different amine-functionalized co-adsorbates that act as hydrogen bonding spacer molecules between PTCDA nanostructures.

Finally, the ordering of fullerene C_{80} cages and their enclosed Dy_3N clusters in a $Dy_3N@C_{80}$ superlattice on Cu(111) has been investigated. The inter- and intramolecular ordering of this adsorbate has been determined by a combined STM, XPD and rXPD study. The fullerene is shown to form an ordered superstructure with islands containing small domains of equally oriented molecules. The endohedral ordering has been determined by XPD and rXPD from which a nitrogen position close to the centre of the cage has been found in the adsorbed state. The endohedral Dy_3N unit is shown to respond to the substrate surface by ordering in specific ways.

A side aspect of this thesis was to further establish the combination of XPD and STM as a way to obtain complete information on large organic adsorbates in two dimensions. While these two methods have been successfully combined for structural analysis of overlayers [289-291] and small organic adsorbates [*85*], this combination has – to the best of my knowledge – not been applied for adsorption studies of large organic adsorbates different from C_{60} [292-294]. Complementary methods are however often needed in STM studies of large organic adsorbates [295] due to the inherent deficiency of STM to allow for a determination of the three-dimensional conformation of adsorbates. This has led to combinations with near edge X-ray absorption fine structure [296-298], normal incidence X-ray standing wavefield absorption [299], LEED [154, 300], X-ray diffraction techniques [301, 302], temperature programmed desorption [303-305] or reflection anisotropy infrared spectroscopy [303, 306] to name but a few techniques that yield results that are complementary to STM. It has been shown in this thesis that XPD can be applied to dilute systems, containing a large number of emitter-scatterer directions. Both systems studied with XPD here are near the limit of adsorbate size for which XPD still yields quantitatively useable results. By the use of rXPD, the application limit for this technique has been pushed further to lower coverage and larger adsorbate systems.

To create a wider variety of self-assembled structures (respectively functional devices), future approaches will have to rely on the combination of different classes of binding motifs. Supramolecular architectures have been shown to depend on the subtle balance between different competing interactions such as hydrogen bonds and metal coordination [159]. However, to date there seems to be no rationally designed supramolecular architecture in two dimensions where combinations of several fundamentally different (non)covalent interactions have been used. The alignment, stabilized by hydrogen bonds, of polyimide strands (Chapter 6) shows however, that different types of interactions might lead to ordered structures even if one of the interactions (in this case the covalent bond) is much stronger than the one in the other direction (hydrogen bond).

Apart from exploiting combinations of different concepts to steer the self-assembly of adsorbates, future supramolecular structures will also be expected to posses an inherent functionality, i.e. going beyond the ‘simple’ formation of networks. A first network with functionalized pores has already been reported [307]. The use of aromatic coupling motifs is promising in bestowing functionality to a network due to the potential charge carrier pathways that are created by the lateral overlap in π-orbitals.

The future of surface-supported self-assembly will also go beyond the nowadays routinely achieved ordered two dimensional structures towards rationally designed hierarchically assembled thin films. First attempts towards a stepwise self-assembly in the third dimensions have already been reported [308]. In chemical environments, 3D self-assembly has been studied for decades and is at the heart of supramolecular chemistry. For the assembly in the third dimension, the strategies from the two-dimensional case might simply be extended combining them with strategies from crystal engineering. Host-guest interactions between subsequent layers [309] have already been shown to work on surfaces which can be regarded as a first step away from true 2D structures. Aromatic interactions with their preference for π-π stacking are ideal for engineering structures in the third dimension as has been shown by the formation of supramolecular columns of HBC on the (111) surfaces of Cu and Au [310]. Apart from true π-π stacking, other aromatic interactions such as the coupling motifs presented in this thesis might also be used in the direction orthogonal to the substrate surface.

Until the ultimate goal of nanotechnology – the facile, cheap, reproducible production of functional nanostructures from the bottom up – will be reached (provided this will ever be the case), intensive research efforts will be needed. The concepts to direct the self-assembly of organic adsorbates outlined in this thesis are expected to be found useful in the context of such future work.

References

1. P. Buffat, J. P. Borel, *Physical Review A* **13**, 2287 (1976).
2. M. Schmidt, R. Kusche, B. von Issendorff, H. Haberland, *Nature* **393**, 238 (1998).
3. Y. Wang, N. Herron, *J. Phys. Chem.* **95**, 525 (1991).
4. J. P. Bucher, D. C. Douglass, L. A. Bloomfield, *Phys. Rev. Lett.* **66**, 3052 (1991).
5. R. P. Feynman, *J. Microelectromech. Syst.* **1**, (1992).
6. www.itrs.net
7. G. M. Whitesides, J. P. Mathias, C. T. Seto, *Science* **254**, 1312 (1991).
8. G. M. Whitesides, B. Grzybowski, *Science* **295**, 2418 (2002).
9. S. R. Forrest, *Nature* **428**, 911 (2004).
10. C. Joachim, J. K. Gimzewski, A. Aviram, *Nature* **408**, 541 (2000).
11. N. Weibel, S. Grunder, M. Mayor, *Organic & Biomolecular Chemistry* **5**, 2343 (2007).
12. L. Kouwenhoven, *Science* **275**, 1896 (1997).
13. A. Schenning, E. W. Meijer, *Chem. Commun.*, 3245 (2005).
14. A. P. Kulkarni, C. J. Tonzola, A. Babel, S. A. Jenekhe, *Chem. Mat.* **16**, 4556 (2004).
15. C. D. Dimitrakopoulos, P. R. L. Malenfant, *Adv. Mater.* **14**, 99 (2002).
16. H. Hoppe, N. S. Sariciftci, *J. Mater. Res.* **19**, 1924 (2004).
17. F. Schreiber, *Phys. Status Solidi A-Appl. Res.* **201**, 1037 (2004).
18. F. Schreiber, *Prog. Surf. Sci.* **65**, 151 (2000).
19. W. Pisula, A. Menon, M. Stepputat, I. Lieberwirth, U. Kolb, A. Tracz, H. Sirringhaus, T. Pakula, K. Mullen, *Adv. Mater.* **17**, 684 (2005).
20. H. Sirringhaus, T. Kawase, R. H. Friend, T. Shimoda, M. Inbasekaran, W. Wu, E. P. Woo, *Science* **290**, 2123 (2000).
21. Y. N. Xia, G. M. Whitesides, *Annual Review of Materials Science* **28**, 153 (1998).
22. J. V. Barth, *Annu. Rev. Phys. Chem.* **58**, 375 (2007).
23. G. Binning, H. Rohrer, C. Gerber, E. Weibel, *Phys. Rev. Lett.* **49**, 57 (1982).
24. G. Binning, C. F. Quate, C. Gerber, *Phys. Rev. Lett.* **56**, 930 (1986).
25. J. V. Barth, G. Costantini, K. Kern, *Nature* **437**, 671 (2005).
26. J. A. Theobald, N. S. Oxtoby, M. A. Phillips, N. R. Champness, P. H. Beton, *Nature* **424**, 1029 (2003).
27. M. E. Canas-Ventura, W. Xiao, D. Wasserfallen, K. Mullen, H. Brune, J. V. Barth, R. Fasel, *Angew. Chem.-Int. Edit.* **46**, 1814 (2007).
28. U. Schickum, R. Decker, F. Klappenberger, G. Zoppellaro, S. Klyatskaya, M. Ruben, I. Silanes, A. Arnau, K. Kern, H. Brune, J. V. Barth, *Nano Lett.* **7**, 3813 (2007).
29. S. Stepanow, N. Lin, D. Payer, U. Schlickum, F. Klappenberger, G. Zoppellaro, M. Ruben, H. Brune, J. V. Barth, K. Kern, *Angew. Chem.-Int. Edit.* **46**, 710 (2007).
30. J. M. Lehn, *Angew. Chem.-Int. Edit. Engl.* **29**, 1304 (1990).
31. B. Moulton, M. J. Zaworotko, *Chem. Rev.* **101**, 1629 (2001).
32. I. W. Lyo, P. Avouris, *Science* **253**, 173 (1991).
33. P. H. Beton, A. W. Dunn, P. Moriarty, *Appl. Phys. Lett.* **67**, 1075 (1995).
34. J. A. Stroscio, D. M. Eigler, *Science* **254**, 1319 (1991).
35. P. Vettiger, M. Despont, U. Drechsler, U. Durig, W. Haberle, M. I. Lutwyche, H. E. Rothuizen, R. Stutz, R. Widmer, G. K. Binnig, *IBM Journal of Research and Development* **44**, 323 (2000).
36. F. Besenbacher, *Rep. Prog. Phys.* **59**, 1737 (1996).
37. S. De Feyter, F. C. De Schryver, *Chem. Soc. Rev.* **32**, 139 (2003).

38. K. H. Ernst, in *Supramolecular Chirality*. (Springer-Verlag Berlin, Berlin, 2006), vol. 265, pp. 209-252.
39. S. M. Barlow, R. Raval, *Surf. Sci. Rep.* **50**, 201 (2003).
40. B. C. Stipe, M. A. Rezaei, W. Ho, *Science* **280**, 1732 (1998).
41. J. I. Pascual, J. V. Barth, G. Ceballos, G. Trimarchi, A. De Vita, K. Kern, H. P. Rust, *J. Chem. Phys.* **120**, 11367 (2004).
42. C. Busse, S. Weigelt, L. Petersen, E. Laegsgaard, F. Besenbacher, T. R. Linderoth, A. H. Thomsen, M. Nielsen, K. V. Gothelf, *J. Phys. Chem. B* **111**, 5850 (2007).
43. S. Weigelt, C. Busse, L. Petersen, E. Rauls, B. Hammer, K. V. Gothelf, F. Besenbacher, T. R. Linderoth, *Nat. Mater.* **5**, 112 (2006).
44. M. A. Filler, S. F. Bent, *Prog. Surf. Sci.* **73**, 1 (2003).
45. S. F. Bent, *J. Phys. Chem. B* **106**, 2830 (2002).
46. J. Repp, G. Meyer, F. E. Olsson, M. Persson, *Science* **305**, 493 (2004).
47. J. Repp, G. Meyer, S. M. Stojkovic, A. Gourdon, C. Joachim, *Phys. Rev. Lett.* **94**, 026803 (2005).
48. J. B. Pendry, *Low Energy Electron Diffraction*. (Academic Press, London, 1974).
49. K. Itaya, *Prog. Surf. Sci.* **58**, 121 (1998).
50. J. K. Gimzewski, C. Joachim, *Science* **283**, 1683 (1999).
51. M. R. Mozafari, C. J. Reed, C. Rostron, V. Hasirci, *J. Liposome Res.* **15**, 93 (2005).
52. T. Komeda, *Prog. Surf. Sci.* **78**, 41 (2005).
53. D. A. Bonnell, J. Garra, *Rep. Prog. Phys.* **71**, 27 (2008).
54. S. Grafstrom, *J. Appl. Phys.* **91**, 1717 (2002).
55. J. Bardeen, *Phys. Rev. Lett.* **6**, 57 (1961).
56. J. Tersoff, D. R. Hamann, *Phys. Rev. B* **31**, 805 (1985).
57. J. Tersoff, D. R. Hamann, *Phys. Rev. Lett.* **50**, 1998 (1983).
58. W. A. Hofer, A. S. Foster, A. L. Shluger, *Rev. Mod. Phys.* **75**, 1287 (2003).
59. J. M. Blanco, F. Flores, R. Perez, *Prog. Surf. Sci.* **81**, 403 (2006).
60. N. D. Lang, *Phys. Rev. Lett.* **56**, 1164 (1986).
61. R. Hoffmann, *Rev. Mod. Phys.* **60**, 601 (1988).
62. A. Nilsson, L. G. M. Pettersson, *Chemical Bonding at Surfaces and Interfaces*. A. Nilsson, L. G. M. Pettersson, J. K. Nosrskov, Eds., (Elsevier, Amsterdam, 2008).
63. R. Strohmaier, J. Petersen, B. Gompf, W. Eisenmenger, *Surf. Sci.* **418**, 91 (1998).
64. V. M. Hallmark, S. Chiang, *Surf. Sci.* **329**, 255 (1995).
65. L. Gross, F. Moresco, M. Alemani, H. Tang, A. Gourdon, C. Joachim, K.-H. Rieder, *Chem. Phys. Lett.* **371**, 750 (2003).
66. M. Schunack, F. Rosei, Y. Naitoh, P. Jiang, A. Gourdon, E. Laegsgaard, I. Stensgaard, C. Joachim, F. Besenbacher, *The Journal of Chemical Physics* **117**, 6259 (2002).
67. H. Tang, C. Coudret, T. Maroutian, R. Berndt, *J. Phys. Chem. B* **109**, 24031 (2005).
68. L. Gross, K. H. Rieder, F. Moresco, S. M. Stojkovic, A. Gourdon, C. Joachim, *Nat. Mater.* **4**, 892 (2005).
69. H. R. Hertz, *Annalen der Physik* **267**, 983 (1887).
70. A. Einstein, *Annalen der Physik* **17**, (1905).
71. W. A. D. M. P. Seah, *Surf. Interface Anal.* **1**, 2 (1979).
72. L. DeBroglie, *Recherches sur la théorie des quanta*. PhD-Thesis (Paris, 1924).
73. C. Davisson, L. H. Germer, *Phys. Rev.* **30**, 705 (1927).
74. G. P. Thomson, *Proc. R. soc. Lond. Ser. A-Contain. Pap. Math. Phys. Character* **128**, 649 (1930).
75. C. S. Fadley, in *Synchrotron Radiation Research: Advances in Surface Science,* R. Z. Bachrach, Ed. (Plenum, New York, 1990), vol. 1, pp. 421-518.
76. W. F. Egelhoff, *Crit. Rev. Solid State Mat. Sci.* **16**, 213 (1990).
77. D. P. Woodruff, *Surf. Sci. Rep.* **62**, 1 (2007).

78. D. P. Woodruff, A. M. Bradshaw, *Rep. Prog. Phys.* **57**, 1029 (1994).
79. C. Westphal, *Appl. Phys. A-Mater. Sci. Process.* **76**, 721 (2003).
80. R. Fasel, P. Aebi, R. G. Agostino, D. Naumovic, J. Osterwalder, A. Santaniello, L. Schlapbach, *Phys. Rev. Lett.* **76**, 4733 (1996).
81. R. Fasel, R. G. Agostino, P. Aebi, L. Schlapbach, *Phys. Rev. B* **60**, 4517 (1999).
82. R. Fasel, A. Cossy, K. H. Ernst, F. Baumberger, T. Greber, J. Osterwalder, *J. Chem. Phys.* **115**, 1020 (2001).
83. F. Allegretti, M. Polcik, D. P. Woodruff, *Surf. Sci.* **601**, 3611 (2007).
84. D. I. Sayago, M. Polcik, G. Nisbet, C. L. A. Lamont, D. P. Woodruff, *Surf. Sci.* **590**, 76 (2005).
85. M. Shimomura, D. Ichikawa, Y. Fukuda, T. Abukawa, T. Aoyama, S. Kono, *Phys. Rev. B* **72**, 4 (2005).
86. R. Gunnella, M. Shimomura, F. D'Amico, T. Abukawa, S. Kono, *Phys. Rev. B* **73**, 7 (2006).
87. C. Westphal, *Surf. Sci. Rep.* **50**, 1 (2003).
88. E. V. Shalaeva, M. V. Kuznetsov, *Journal of Structural Chemistry* **44**, 465 (2003).
89. R. Fasel, P. Aebi, *Chimia* **56**, 566 (2002).
90. J. Osterwalder, A. Tamai, W. Auwarter, M. P. Allan, T. Greber, *Chimia* **60**, A795 (2006).
91. C. S. Fadley, *Nucl. Instrum. Methods Phys. Res. Sect. A-Accel. Spectrom. Dect. Assoc. Equip.* **547**, 24 (2005).
92. K. F. Braun, S. W. Hla, *Nano Lett.* **5**, 73 (2005).
93. L. A. Zotti, G. Teobaldi, W. A. Hofer, W. Auwarter, A. Weber-Bargioni, J. V. Barth, *Surf. Sci.* **601**, 2409 (2007).
94. J. A. Miwa, F. Cicoira, S. Bedwani, #x301, phane, J. Lipton-Duffin, D. F. Perepichka, A. Rochefort, F. Rosei, *J. Phys. Chem. C* **112**, 10214 (2008).
95. I. K. Robinson, D. J. Tweet, *Rep. Prog. Phys.* **55**, 599 (1992).
96. P. Kruger, S. Bourgeois, B. Domenichini, H. Magnan, D. Chandesris, P. Le Fevre, A. M. Flank, J. Jupille, L. Floreano, A. Cossaro, A. Verdini, A. Morgante, *Phys. Rev. Lett.* **100**, 055501 (2008).
97. P. Kruger, S. Bourgeois, B. Domenichini, H. Magnan, D. Chandesris, P. Le Fevre, L. Floreano, A. Cossaro, A. Verdini, A. Morgante, *Surf. Sci.* **601**, 3952 (2007).
98. P. Steiner, T. Straub, F. Reinert, R. Zimmermann, S. Hufner, *Surf. Sci.* **291**, 154 (1993).
99. S. Hufner, J. Osterwalder, T. Greber, L. Schlapbach, *Phys. Rev. B* **42**, 7350 (1990).
100. C. Müller, *Spherical harmonics*. Lecture notes in mathematics (Springer, Berlin, 1966), vol. 17.
101. L. Despont, D. Naumovic, F. Clerc, C. Koitzsch, M. G. Garnier, F. J. G. de Abajo, M. A. Van Hove, P. Aebi, *Surf. Sci.* **600**, 380 (2006).
102. R. Fasel, P. Aebi, J. Osterwalder, L. Schlapbach, R. G. Agostino, G. Chiarello, *Phys. Rev. B* **50**, 14516 (1994).
103. F. Bruno, L. Floreano, A. Verdini, D. Cvetko, R. Gotter, A. Morgante, A. Canepa, S. Terreni, *J. Electron Spectrosc. Relat. Phenom.* **127**, 85 (2002).
104. Hyperchem. (Hypercube Inc., 2002).
105. J. Hafner, *J. Comput. Chem.* **29**, 2044 (2008).
106. P. Geerlings, F. De Proft, W. Langenaeker, *Chem. Rev.* **103**, 1793 (2003).
107. W. Kohn, A. D. Becke, R. G. Parr, *J. Phys. Chem.* **100**, 12974 (1996).
108. D. R. Hartree, *Proceedings of the Cambridge Philosophical Society* **24**, 89 (1928).
109. D. R. Hartree, *Proceedings of the Cambridge Philosophical Society* **24**, 111 (1928).
110. V. A. Fock, *Zeitschrift Fur Physik* **61**, (1930).

111. M. J. S. Dewar, E. G. Zoebisch, E. F. Healy, J. J. P. Stewart, *J. Am. Chem. Soc.* **107**, 3902 (1985).
112. R. Hoffmann, *J. Chem. Phys.* **39**, 1397 (1963).
113. E. Hückel, *Zeitschrift Fur Physik* **70**, (1931).
114. J. C. Slater, *Phys. Rev.* **36**, 57 (1930).
115. O. Gröning, R. Fasel. (EMPA, Materials Science and Technology, Thun, 2004).
116. A. Weber-Bargioni, W. Auwarter, F. Klappenberger, J. Reichert, S. Lefrancois, T. Strunskus, C. Woll, A. Schiffrin, Y. Pennec, J. V. Barth, *ChemPhysChem* **9**, 89 (2008).
117. W. Auwarter, A. Weber-Bargioni, A. Riemann, A. Schiffrin, O. Groning, R. Fasel, J. V. Barth, *J. Chem. Phys.* **124**, 6 (2006).
118. M. Parschau, R. Fasel, K. H. Ernst, O. Groning, L. Brandenberger, R. Schillinger, T. Greber, A. R. Seitsonen, Y. T. Wu, J. S. Siegel, *Angew. Chem.-Int. Edit.* **46**, 8258 (2007).
119. D. N. Futaba, J. P. Landry, A. Loui, S. Chiang, *Phys. Rev. B* **65**, 7 (2002).
120. A. Loui, S. Chiang, *Appl. Surf. Sci.* **237**, 559 (2004).
121. T. Schlick, *Molecular Modeling and Simulation: An Interdisciplinary Guide*. (Springer, New York, 2000).
122. J. W. Ponder, D. A. Case, in *Protein Simulations*. (Academic Press Inc, San Diego, 2003), vol. 66, pp. 27-+.
123. A. D. MacKerell, D. Bashford, M. Bellott, R. L. Dunbrack, J. D. Evanseck, M. J. Field, S. Fischer, J. Gao, H. Guo, S. Ha, D. Joseph-McCarthy, L. Kuchnir, K. Kuczera, F. T. K. Lau, C. Mattos, S. Michnick, T. Ngo, D. T. Nguyen, B. Prodhom, W. E. Reiher, B. Roux, M. Schlenkrich, J. C. Smith, R. Stote, J. Straub, M. Watanabe, J. Wiorkiewicz-Kuczera, D. Yin, M. Karplus, *J. Phys. Chem. B* **102**, 3586 (1998).
124. D. A. Pearlman, D. A. Case, J. W. Caldwell, W. S. Ross, T. E. Cheatham, S. Debolt, D. Ferguson, G. Seibel, P. Kollman, *Computer Physics Communications* **91**, 1 (1995).
125. A. T. Macias, A. D. MacKerell, *J. Comput. Chem.* **26**, 1452 (2005).
126. T. J. Mullen, C. Srinivasan, M. J. Shuster, M. W. Horn, A. M. Andrews, P. S. Weiss, *Journal of Nanoparticle Research* **10**, 1231 (2008).
127. V. S. Iyer, K. Yoshimura, V. Enkelmann, R. Epsch, J. P. Rabe, K. Mullen, *Angew. Chem.-Int. Edit.* **37**, 2696 (1998).
128. S. Rousset, V. Repain, G. Baudot, Y. Garreau, J. Lecoeur, *J. Phys.-Condes. Matter* **15**, S3363 (2003).
129. Z. H. Wang, F. Dotz, V. Enkelmann, K. Mullen, *Angew. Chem.-Int. Edit.* **44**, 1247 (2005).
130. J. S. Wu, W. Pisula, K. Mullen, *Chem. Rev.* **107**, 718 (2007).
131. F. Jackel, M. D. Watson, K. Mullen, J. P. Rabe, *Phys. Rev. Lett.* **92**, 188303 (2004).
132. W. D. Xiao, P. Ruffieux, K. Ait-Mansour, O. Groning, K. Palotas, W. A. Hofer, P. Groning, R. Fasel, *J. Phys. Chem. B* **110**, 21394 (2006).
133. J. Kroger, N. Neel, H. Jensen, R. Berndt, R. Rurali, N. Lorente, *J. Phys.-Condes. Matter* **18**, S51 (2006).
134. S. J. Stranick, M. M. Kamna, P. S. Weiss, *Nanotechnology* **7**, 443 (1996).
135. P. Avouris, I. W. Lyo, P. Molinàs-Mata, *Chem. Phys. Lett.* **240**, 423 (1995).
136. R. Smoluchowski, *Phys. Rev.* **60**, 661 (1941).
137. M. Vladimirova, M. Stengel, A. De Vita, A. Baldereschi, M. Bohringer, K. Morgenstern, R. Berndt, W. D. Schneider, *Europhys. Lett.* **56**, 254 (2001).
138. T. Zambelli, P. Jiang, J. Lagoute, S. E. Grillo, S. Gauthier, A. Gourdon, C. Joachim, *Phys. Rev. B* **66**, 075410 (2002).
139. S. X. Xiao, M. Myers, Q. Miao, S. Sanaur, K. L. Pang, M. L. Steigerwald, C. Nuckolls, *Angew. Chem.-Int. Edit.* **44**, 7390 (2005).

140. S. Xiao, C. Nuckolls. (unpublished, 2008).
141. http://astrochemistry.ca.astro.it/database/
142. S. Duhm, A. Gerlach, I. Salzmann, B. Broker, R. L. Johnson, F. Schreiber, N. Koch, *Org. Electron.* **9**, 111 (2008).
143. J. Y. Park, G. M. Sacha, M. Enachescu, D. F. Ogletree, R. A. Ribeiro, P. C. Canfield, C. J. Jenks, P. A. Thiel, J. J. Saenz, M. Salmeron, *Phys. Rev. Lett.* **95**, 136802 (2005).
144. C. Pignedoli. (unpublished 2008).
145. G. Ertl, *Surf. Sci.* **300**, 742 (1994).
146. J. F. Jia, Y. Hasegawa, K. Inoue, W. S. Yang, T. Sakurai, *Appl. Phys. A-Mater. Sci. Process.* **66**, S1125 (1998).
147. J. F. Jia, K. Inoue, Y. Hasegawa, W. S. Yang, T. Sakurai, *Phys. Rev. B* **58**, 1193 (1998).
148. X. Bouju, C. Girard, H. Tang, C. Joachim, L. Pizzagalli, *Phys. Rev. B* **55**, 16498 (1997).
149. J. E. Anthony, *Angew. Chem.-Int. Edit.* **47**, 452 (2008).
150. A. R. Murphy, J. M. J. Frechet, *Chem. Rev.* **107**, 1066 (2007).
151. J. S. Wu, *Curr. Org. Chem.* **11**, 1220 (2007).
152. S. Wu, M. T. Gonzalez, R. Huber, S. Grunder, M. Mayor, C. Schonenberger, M. Calame, *Nat Nano* **3**, 569 (2008).
153. M. C. Blum, E. Cavar, M. Pivetta, F. Patthey, W. D. Schneider, *Angew. Chem.-Int. Edit.* **44**, 5334 (2005).
154. V. A. Langlais, Y. Gauthier, H. Belkhir, O. Maresca, *Phys. Rev. B* **72**, 085444 (2005).
155. G. R. Desiraju, *Accounts Chem. Res.* **35**, 565 (2002).
156. C. A. Hunter, K. R. Lawson, J. Perkins, C. J. Urch, *Journal of the Chemical Society-Perkin Transactions 2*, 651 (2001).
157. C. A. Hunter, *Chem. Soc. Rev.* **23**, 101 (1994).
158. A. Langner, S. L. Tait, N. Lin, C. Rajadurai, M. Ruben, K. Kern, *Proc. Natl. Acad. Sci. U. S. A.* **104**, 17927 (2007).
159. S. Stepanow, N. Lin, J. V. Barth, *J. Phys.-Condes. Matter* **20**, 15 (2008).
160. C. Schmuck, *Angew. Chem.-Int. Edit.* **42**, 2448 (2003).
161. D. Pena, D. Perez, E. Guitian, L. Castedo, *Org. Lett.* **1**, 1555 (1999).
162. L. Barnett, D. M. Ho, K. K. Baldridge, R. A. Pascal, *J. Am. Chem. Soc.* **121**, 727 (1999).
163. M. Grunewald, P. Thomas, *Phys. Status Solidi B-Basic Res.* **94**, 125 (1979).
164. R. A. Marcus, *J. Chem. Phys.* **24**, 966 (1956).
165. R. A. Marcus, *Annu. Rev. Phys. Chem.* **15**, 155 (1964).
166. Y. A. Berlin, G. R. Hutchison, P. Rempala, M. A. Ratner, J. Michl, *J. Phys. Chem. A* **107**, 3970 (2003).
167. A. Einstein, *Annalen der Physik* **17**, 549 (1905).
168. N. S. Hush, *J. Chem. Phys.* **28**, 962 (1958).
169. N. S. Hush, *Transactions of the Faraday Society* **57**, 557 (1961).
170. G. R. Hutchison, M. A. Ratner, T. J. Marks, *J. Am. Chem. Soc.* **127**, 2339 (2005).
171. A. Van Vooren, J. S. Kim, J. Cornil, *ChemPhysChem* **9**, 989 (2008).
172. W. Q. Deng, W. A. Goddard, *J. Phys. Chem. B* **108**, 8614 (2004).
173. J. L. Bredas, J. P. Calbert, D. A. da Silva, J. Cornil, *Proc. Natl. Acad. Sci. U. S. A.* **99**, 5804 (2002).
174. N. Koch, *ChemPhysChem* **8**, 1438 (2007).
175. T. W. Kelley, P. F. Baude, C. Gerlach, D. E. Ender, D. Muyres, M. A. Haase, D. E. Vogel, S. D. Theiss, *Chem. Mat.* **16**, 4413 (2004).
176. H. Klauk, M. Halik, U. Zschieschang, G. Schmid, W. Radlik, W. Weber, *J. Appl. Phys.* **92**, 5259 (2002).

177. O. D. Jurchescu, J. Baas, T. T. M. Palstra, *Appl. Phys. Lett.* **84**, 3061 (2004).
178. R. B. Campbell, J. Trotter, J. M. Robertson, *Acta Crystallographica* **14**, 705 (1961).
179. R. J. Wilson, S. Chiang, *Phys. Rev. Lett.* **58**, 369 (1987).
180. J. C. Swarbrick, J. Ma, J. A. Theobald, N. S. Oxtoby, J. N. O'Shea, N. R. Champness, P. H. Beton, *J. Phys. Chem. B* **109**, 12167 (2005).
181. L. M. A. Perdigao, G. N. Fontes, B. L. Rogers, N. S. Oxtoby, G. Goretzki, N. R. Champness, P. H. Beton, *Phys. Rev. B* **76**, 245402 (2007).
182. M. de Wild, S. Berner, H. Suzuki, H. Yanagi, D. Schlettwein, S. Ivan, A. Baratoff, H. J. Guentherodt, T. A. Jung, *ChemPhysChem* **3**, 881 (2002).
183. E. Barrena, D. G. de Oteyza, H. Dosch, Y. Wakayama, *ChemPhysChem* **8**, 1915 (2007).
184. C. Bobisch, T. Wagner, A. Bannani, R. Moller, *J. Chem. Phys.* **119**, 9804 (2003).
185. W. Chen, H. Li, H. Huang, Y. X. Fu, H. L. Zhang, J. Ma, A. T. S. Wee, *J. Am. Chem. Soc.* **130**, 12285 (2008).
186. I. Chizhov, A. Kahn, G. Scoles, *J. Cryst. Growth* **208**, 449 (2000).
187. F. M. Raymo, *Adv. Mater.* **14**, 401 (2002).
188. R. Temirov, S. Soubatch, A. Luican, F. S. Tautz, *Nature* **444**, 350 (2006).
189. H. Vazquez, F. Flores, R. Oszwaldowski, J. Ortega, R. Perez, A. Kahn, 2004.
190. H. Yamane, D. Yoshimura, E. Kawabe, R. Sumii, K. Kanai, Y. Ouchi, N. Ueno, K. Seki, *Phys. Rev. B* **76**, (2007).
191. G. Pawin, K. L. Wong, K. Y. Kwon, L. Bartels, *Science* **313**, 961 (2006).
192. I. Horcas, R. Fernandez, J. M. Gomez-Rodriguez, J. Colchero, J. Gomez-Herrero, A. M. Baro, *Rev. Sci. Instrum.* **78**, (2007).
193. A. D. Becke, *J. Chem. Phys.* **98**, 5648 (1993).
194. C. T. Lee, W. T. Yang, R. G. Parr, *Phys. Rev. B* **37**, 785 (1988).
195. W. J. Hehre, L. Radom, P. V. Schleyer, P. J., *Ab inito molecular orbital theory*. (Wiley, New York, 1986).
196. J. C. Swarbrick, B. L. Rogers, N. R. Champness, P. H. Beton, *J. Phys. Chem. B* **110**, 6110 (2006).
197. J. Ma, B. L. Rogers, M. J. Humphry, D. J. Ring, G. Goretzki, N. R. Champness, P. H. Beton, *J. Phys. Chem. B* **110**, 12207 (2006).
198. S. Mullegger, I. Salzmann, R. Resel, G. Hlawacek, C. Teichert, A. Winkler, *J. Chem. Phys.* **121**, 2272 (2004).
199. M. Oehzelt, L. Grill, S. Berkebile, G. Koller, F. P. Netzer, M. G. Ramsey, *ChemPhysChem* **8**, 1707 (2007).
200. S. Mannsfeld, M. Toerker, T. Schmitz-Hübsch, F. Sellam, T. Fritz, K. Leo, *Org. Electron.* **2**, 121 (2001).
201. J. Mendez, R. Caillard, G. Otero, N. Nicoara, J. A. Martin-Gago, *Adv. Mater.* **18**, 2048 (2006).
202. www.pwscf.org
203. http://classic.chem.msu.su/gran/gamess/index.html
204. R. Scholz, A. Y. Kobitski, D. R. T. Zahn, M. Schreiber, *Phys. Rev. B* **72**, (2005).
205. S. F. Boys, F. Bernardi, *Molecular Physics* **19**, 553 (1970).
206. M. C. Daza, J. A. Dobado, J. M. Molina, P. Salvador, M. Duran, J. L. Villaveces, *J. Chem. Phys.* **110**, 11806 (1999).
207. H. Spillmann, A. Kiebele, M. Stohr, T. A. Jung, D. Bonifazi, F. Y. Cheng, F. Diederich, *Adv. Mater.* **18**, 275 (2006).
208. S. Stepanow, M. Lingenfelder, A. Dmitriev, H. Spillmann, E. Delvigne, N. Lin, X. B. Deng, C. Z. Cai, J. V. Barth, K. Kern, *Nat. Mater.* **3**, 229 (2004).
209. F. Silly, A. Q. Shaw, K. Porfyrakis, G. A. D. Briggs, M. R. Castell, *Appl. Phys. Lett.* **91**, 3 (2007).

210. F. Silly, A. Q. Shaw, K. Porfyrakis, J. H. Warner, A. A. R. Watt, M. R. Castell, H. Umemoto, T. Akachi, H. Shinohara, G. A. D. Briggs, *Chem. Commun.*, 4616 (2008).
211. R. Madueno, M. T. Raisanen, C. Silien, M. Buck, *Nature* **454**, 618 (2008).
212. S. Weigelt, C. Busse, C. Bombis, M. M. Knudsen, K. V. Gothelf, E. Laegsgaard, F. Besenbacher, T. R. Linderoth, *Angew. Chem.-Int. Edit.* **47**, 4406 (2008).
213. M. Matena, T. Riehm, M. Stohr, T. A. Jung, L. H. Gade, *Angew. Chem.-Int. Edit.* **47**, 2414 (2008).
214. N. A. A. Zwaneveld, R. Pawlak, M. Abel, D. Catalin, D. Gigmes, D. Bertin, L. Porte, *J. Am. Chem. Soc.* **130**, 6678 (2008).
215. L. Grill, M. Dyer, L. Lafferentz, M. Persson, M. V. Peters, S. Hecht, *Nat. Nanotechnol.* **2**, 687 (2007).
216. S. W. Hla, L. Bartels, G. Meyer, K. H. Rieder, *Phys. Rev. Lett.* **85**, 2777 (2000).
217. Y. Okawa, M. Aono, *Nature* **409**, 683 (2001).
218. P. K. Weiner, P. A. Kollman, *J. Comput. Chem.* **2**, 287 (1981).
219. M. I. Veld, P. Iavicoli, S. Haq, D. B. Amabilino, R. Raval, *Chem. Commun.*, 1536 (2008).
220. S. Weigelt, C. Bombis, C. Busse, M. M. Knudsen, K. V. Gothelf, E. Laegsgaard, F. Besenbacher, T. R. Linderoth, *ACS Nano* **2**, 651 (2008).
221. S. Weigelt, C. Busse, C. Bombis, M. M. Knudsen, K. V. Gothelf, T. Strunskus, C. Woll, M. Dahlbom, B. Hammer, E. Laegsgaard, F. Besenbacher, T. R. Linderoth, *Angew. Chem.-Int. Edit.* **46**, 9227 (2007).
222. M. Ree, *Macromolecular Research* **14**, 1 (2006).
223. D. Coulman, J. Edman, *Macromolecular Symposia* **101**, 471 (1996).
224. H. Nawafune, K. Akamatsu, *Journal of the Japan Institute of Metals* **69**, 179 (2005).
225. E. Halasa, *Polimery* **48**, 254 (2003).
226. Y. S. Negi, S. R. Damkale, S. Ansari, *Journal of Macromolecular Science-Polymer Reviews* **C41**, 119 (2001).
227. T. Hasegawa, K. Horie, *Progress in Polymer Science* **26**, 259 (2001).
228. A. S. Mathews, I. Kim, C. S. Ha, *Macromolecular Research*, 114 (2007).
229. S. Yokoyama, M. Keil, H. Sotobayashi, A. M. Bradshaw, M. Kakimoto, Y. Imai, C. L. A. Lamont, *Zeitschrift Fur Physikalische Chemie-International Journal of Research in Physical Chemistry & Chemical Physics* **196**, 43 (1996).
230. T. Rupp, M. Eberhardt, H. Gruler, *Jpn. J. Appl. Phys. Part 1 - Regul. Pap. Short Notes Rev. Pap.* **31**, 3636 (1992).
231. W. Meyer, M. Grunze, R. Lamb, A. Ortegavilamil, W. Schrepp, W. Braun, *Surf. Sci.* **273**, 205 (1992).
232. J. H. Jou, C. L. Cheng, E. C. Y. Jou, A. C. M. Yang, *Journal of Polymer Science Part B-Polymer Physics* **34**, 2239 (1996).
233. N. L. Jeon, R. G. Nuzzo, *Langmuir* **11**, 341 (1995).
234. J. R. Salem, F. O. Sequeda, J. Duran, W. Y. Lee, R. M. Yang, *J. Vac. Sci. Technol. A-Vac. Surf. Films* **4**, 369 (1986).
235. R. N. Lamb, J. Baxter, M. Grunze, C. W. Kong, W. N. Unertl, *Langmuir* **4**, 249 (1988).
236. W. H. Tsai, F. J. Boerio, K. M. Jackson, *Langmuir* **8**, 1443 (1992).
237. T. J. Shin, B. Lee, H. S. Youn, K. B. Lee, M. Ree, *Langmuir* **17**, 7842 (2001).
238. G. D. Hietpas, D. L. Allara, *Journal of Polymer Science Part B-Polymer Physics* **36**, 1247 (1998).
239. M. A. Perez, Y. Ren, R. J. Farris, S. L. Hsu, *Macromolecules* **27**, 6740 (1994).
240. B. J. Factor, T. P. Russell, M. F. Toney, *Macromolecules* **26**, 2847 (1993).

241. I. Karamancheva, V. Stefov, B. Soptrajanov, G. Danev, E. Spasova, J. Assa, *FTIR spectroscopy and FTIR microscopy of vacuum-evaporated polyimide thin films.* (1999), pp. 369-374.
242. A. Mochizuki, T. Teranishi, M. Ueda, *Polymer Journal* **26**, 315 (1994).
243. A. Orzeszko, W. Kosinskabanbula, *European Polymer Journal* **27**, 1107 (1991).
244. Y. Y. Maruo, Y. Andoh, S. Sasaki, *J. Vac. Sci. Technol. A-Vac. Surf. Films* **11**, 2590 (1993).
245. J. A. Derose, R. M. Leblanc, *Surf. Sci. Rep.* **22**, 73 (1995).
246. T. Ishi-i, R. Kuwahara, A. Takata, Y. Jeong, K. Sakurai, S. Mataka, *Chem.-Eur. J.* **12**, 763 (2006).
247. T. Ishi-i, K. Yaguma, T. Thiemann, M. Yashima, K. Ueno, S. Mataka, *Chemistry Letters* **33**, 1244 (2004).
248. A. Gourdon, *Angew. Chem.-Int. Edit.* **47**, 6950 (2008).
249. B. E. Bent, *Chem. Rev.* **96**, 1361 (1996).
250. D. Payer, S. Rauschenbach, N. Malinowski, M. Konuma, C. Virojanadara, U. Starke, C. Dietrich-Buchecker, J. P. Collin, J. P. Sauvage, N. Lin, K. Kern, *J. Am. Chem. Soc.* **129**, 15662 (2007).
251. C. J. Satterley, L. M. A. Perdigao, A. Saywell, G. Magnano, A. Rienzo, L. C. Mayor, V. R. Dhanak, P. H. Beton, J. N. O'Shea, *Nanotechnology* **18**, 5 (2007).
252. A. Saywell, G. Magnano, C. J. Satterley, L. M. A. Perdigao, N. R. Champness, P. H. Beton, J. N. O'Shea, *J. Phys. Chem. C* **112**, 7706 (2008).
253. H. J. Rader, A. Rouhanipour, A. M. Talarico, V. Palermo, P. Samori, K. Mullen, *Nat. Mater.* **5**, 276 (2006).
254. L. Vitali, S. Fabris, A. M. Conte, S. Brink, M. Ruben, S. Baroni, K. Kern, *Nano Lett.*, (2008).
255. P. M. Albrecht, J. W. Lyding, *Appl. Phys. Lett.* **83**, 5029 (2003).
256. K. S. Novoselov, A. K. Geim, S. V. Morozov, D. Jiang, Y. Zhang, S. V. Dubonos, I. V. Grigorieva, A. A. Firsov, *Science* **306**, 666 (2004).
257. A. K. Geim, K. S. Novoselov, *Nat. Mater.* **6**, 183 (2007).
258. E. J. H. Lee, K. Balasubramanian, R. T. Weitz, M. Burghard, K. Kern, *Nat. Nanotechnol.* **3**, 486 (2008).
259. T. Wassmann, A. P. Seitsonen, A. M. Saitta, M. Lazzeri, F. Mauri, *Phys. Rev. Lett.* **101**, 096402 (2008).
260. K. Weiss, G. Beernink, F. Dotz, A. Birkner, K. Mullen, C. H. Woll, *Angew. Chem.-Int. Edit.* **38**, 3748 (1999).
261. G. Beernink, M. Gunia, F. Dotz, H. Ostrom, K. Weiss, K. Mullen, C. Woll, *ChemPhysChem* **2**, 317 (2001).
262. R. Rieger, K. Mullen. (unpublished).
263. R. Scholl, C. Seer, *Justus Liebig's Annalen der Chemie* **394**, 111 (1912).
264. X. Xue, L. T. Scott, *Org. Lett.* **9**, 3937 (2007).
265. T. Laino, C. Pignedoli. (unpublished).
266. X. L. Feng, J. S. Wu, M. Ai, W. Pisula, L. J. Zhi, J. P. Rabe, K. Mullen, *Angew. Chem.-Int. Edit.* **46**, 3033 (2007).
267. L. Dunsch, S. F. Yang, *Phys. Chem. Chem. Phys.* **9**, 3067 (2007).
268. H. Shinohara, *Rep. Prog. Phys.* **63**, 843 (2000).
269. S. Stevenson, G. Rice, T. Glass, K. Harich, F. Cromer, M. R. Jordan, J. Craft, E. Hadju, R. Bible, M. M. Olmstead, K. Maitra, A. J. Fisher, A. L. Balch, H. C. Dorn, *Nature* **401**, 55 (1999).
270. L. Dunsch, S. Yang, *Small* **3**, 1298 (2007).
271. T. Inoue, T. Tomiyama, T. Sugai, H. Shinohara, *Chem. Phys. Lett.* **382**, 226 (2003).

272. Z. Q. Shi, X. Wu, C. R. Wang, X. Lu, H. Shinohara, *Angew. Chem.-Int. Edit.* **45**, 2107 (2006).

273. F. Hof, S. L. Craig, C. Nuckolls, J. Rebek, *Angew. Chem.-Int. Edit.* **41**, 1488 (2002).

274. L. Alvarez, T. Pichler, P. Georgi, T. Schwieger, H. Peisert, L. Dunsch, Z. Hu, M. Knupfer, J. Fink, P. Bressler, M. Mast, M. S. Golden, *Phys. Rev. B* **66**, 035107 (2002).

275. S. F. Yang, L. Dunsch, *Chem.-Eur. J.* **12**, 413 (2005).

276. S. Stevenson, J. P. Phillips, J. E. Reid, M. M. Olmstead, S. P. Rath, A. L. Balch, *Chem. Commun.*, 2814 (2004).

277. M. Wolf, K. H. Muller, D. Eckert, Y. Skourski, P. Georgi, R. Marczak, M. Krause, L. Dunsch, *J. Magn. Magn. Mater.* **290**, 290 (2005).

278. S. F. Yang, S. I. Troyanov, A. A. Popov, M. Krause, L. Dunsch, *J. Am. Chem. Soc.* **128**, 16733 (2006).

279. M. Wolf, K. H. Muller, Y. Skourski, D. Eckert, P. Georgi, M. Krause, L. Dunsch, *Angew. Chem.-Int. Edit.* **44**, 3306 (2005).

280. D. F. Leigh, C. Norenberg, D. Cattaneo, J. H. G. Owen, K. Porfyrakis, A. L. Bassi, A. Ardavan, G. A. D. Briggs, *Surf. Sci.* **601**, 2750 (2007).

281. D. S. Deak, F. Silly, K. Porfyrakis, M. R. Castell, *J. Am. Chem. Soc.* **128**, 13976 (2006).

282. D. S. Deak, F. Silly, K. Porfyrakis, M. R. Castell, *Nanotechnology* **18**, 6 (2007).

283. C. Ton-That, A. G. Shard, S. Egger, V. R. Dhanak, A. Taninaka, H. Shinohara, M. E. Welland, *Phys. Rev. B* **68**, 045424 (2003).

284. R. A. J. Woolley, K. H. G. Schulte, L. Wang, P. J. Moriarty, B. C. C. Cowie, H. Shinohara, M. Kanai, T. J. S. Dennis, *Nano Lett.* **4**, 361 (2004).

285. M. Treier, P. Ruffieux, R. Schillinger, T. Greber, K. Mullen, R. Fasel, *Surf. Sci.* **602**, L84 (2008).

286. T. Heine, K. Vietze, G. Seifert, *Magn. Reson. Chem.* **42**, S199 (2004).

287. T. Greber, J. Osterwalder, D. Naumovic, A. Stuck, S. Hufner, L. Schlapbach, *Phys. Rev. Lett.* **69**, 1947 (1992).

288. D. Naumovic, A. Stuck, T. Greber, J. Osterwalder, L. Schlapbach, *Phys. Rev. B* **47**, 7462 (1993).

289. W. Auwarter, T. J. Kreutz, T. Greber, J. Osterwalder, *Surf. Sci.* **429**, 229 (1999).

290. F. Sedona, M. Eusebio, G. A. Rizzi, G. Granozzi, D. Ostermann, K. Schierbaum, *Phys. Chem. Chem. Phys.* **7**, 697 (2005).

291. T. Orzali, S. Agnoli, M. Sambi, G. Granozzi, *Surf. Sci.* **569**, 105 (2004).

292. A. Tamai, W. Auwarter, C. Cepek, F. Baumberger, T. Greber, J. Osterwalder, *Surf. Sci.* **566**, 633 (2004).

293. M. Abel, A. Dmitriev, R. Fasel, N. Lin, J. V. Barth, K. Kern, *Phys. Rev. B* **67**, 245407 (2003).

294. J. Weckesser, C. Cepek, R. Fasel, J. V. Barth, F. Baumberger, T. Greber, K. Kern, *J. Chem. Phys.* **115**, 9001 (2001).

295. D. P. Woodruff, *Surf. Sci.* **602**, 2963 (2008).

296. H. Glowatzki, G. N. Gavrila, S. Seifert, R. L. Johnson, J. Rader, K. Mullen, D. R. T. Zahn, J. P. Rabe, N. Koch, *J. Phys. Chem. C* **112**, 1570 (2008).

297. M. E. Canas-Ventura, F. Klappenberger, S. Clair, S. Pons, K. Kern, H. Brune, T. Strunskus, C. Woll, R. Fasel, J. V. Barth, *J. Chem. Phys.* **125**, 8 (2006).

298. M. Bohringer, K. Morgenstern, W. D. Schneider, M. Wuhn, C. Woll, R. Berndt, *Surf. Sci.* **444**, 199 (2000).

299. S. M. Driver, D. P. Woodruff, *Langmuir* **16**, 6693 (2000).

300. K. Glockler, C. Seidel, A. Soukopp, M. Sokolowski, E. Umbach, M. Bohringer, R. Berndt, W. D. Schneider, *Surf. Sci.* **405**, 1 (1998).

301. T. Y. B. Leung, M. C. Gerstenberg, D. J. Lavrich, G. Scoles, F. Schreiber, G. E. Poirier, *Langmuir* **16**, 549 (2000).
302. R. Schwedhelm, J. P. Schlomka, S. Woedtke, R. Adelung, L. Kipp, M. Tolan, W. Press, M. Skibowski, *Phys. Rev. B* **59**, 13394 (1999).
303. T. E. Jones, C. J. Baddeley, *Surf. Sci.* **519**, 237 (2002).
304. C. B. France, P. G. Schroeder, J. C. Forsythe, B. A. Parkinson, *Langmuir* **19**, 1274 (2003).
305. C. Seidel, A. Soukopp, R. Li, P. Bauerle, E. Umbach, *Surf. Sci.* **374**, 17 (1997).
306. L. Scudiero, D. E. Barlow, K. W. Hipps, *J. Phys. Chem. B* **106**, 996 (2002).
307. L. M. A. Perdigao, A. Saywell, G. N. Fontes, P. A. Staniec, G. Goretzki, A. G. Phillips, N. R. Champness, P. H. Beton, *Chem.-Eur. J.* **14**, 7600 (2008).
308. M. Altman, O. Zenkina, G. Evmenenko, P. Dutta, M. E. van der Boom, *J. Am. Chem. Soc.* **130**, 5040 (2008).
309. W. Xiao, D. Passerone, P. Ruffieux, K. Ait-Mansour, O. Groning, E. Tosatti, J. S. Siegel, R. Fasel, *J. Am. Chem. Soc.* **130**, 4767 (2008).
310. P. Ruffieux, O. Groning, M. Bielmann, C. Simpson, K. Mullen, L. Schlapbach, P. Groning, *Phys. Rev. B* **66**, 073409 (2002).

Curriculum vitae

Matthias Treier
born 11.09.1980 in Leuggern AG

1987-1996	Basic education in Würenlingen / Endingen AG
1996-2000	Kantonsschule Baden, Scientific matura
2000-2002	Physics undergraduate studies at Ecole polytechnique fédérale de Lausanne (EPFL)
2002-2003	Physics undergraduate studies at University of Nottingham UK
2003-2005	Physics undergraduate studies at EPFL
2005	Master of science in physics at EPFL
since May 2005	PhD student in the nanotech@surfaces group at the Swiss Federal Laboratories for Materials Testing and Research (EMPA)

List of publications

M. Treier, P. Ruffieux, R. Schillinger, T. Greber, K. Müllen, R. Fasel, *Living on the edge: A nanographene molecule adsorbed across gold step edges*, Surf. Sci. 602, L84 (2008)

M. Treier, P. Ruffieux, P. Gröning, S. Xiao, C. Nuckolls, R. Fasel, *An aromatic coupling motif fort two-dimensional supramolecular architectures*, Chem. Commun. 4555 (2008)

M. Treier, N.V. Richardson, R. Fasel, *Fabrication of surface-supported low-dimensional polyimide networks*, J. Am. Chem. Soc. 130, 14054 (2008)

M. Treier, R. Fasel, N.R. Champness, S. Argent, N.V. Richardson, *Molecular imaging of polyimide formation*, Phys. Chem. Chem. Phys. 11, 1209 (2009)

M. Treier, M.-T. Nguyen, N.V. Richardson, C. Pignedoli, D. Passerone, R. Fasel, *Tailoring low-dimensional organic semiconductor nanostructures*, Nano letters 9, 126 (2009)

M. Treier, R. Fasel, *Surface science approaches to molecular nanostructures*, Chimia 63, 122 (2009)

A. Lehnert, P. Buluschek, N. Weiss, J. Giesecke, M. Treier, S. Rusponi, H. Brune, *High resolution in situ magneto-optic Kerr effect and scanning tunneling microscopy setup with all optical components in UHV*, Rev. Sci. Instr. 80, 023902 (2009)

K. Ait-Mansour, M. Treier, P. Ruffieux, M. Bieri, R. Jaafar, P. Gröning, R. Fasel, O. Gröning, *Template-directed molecular nanostructures on the Ag/Pt(111) dislocation network*, J. Phys. Chem. C. 113, 8407 (2009)

M. Treier, P. Ruffieux, L. Dunsch, T. Greber, R. Fasel, *Inter- and intramolecular ordering of* $Dy_3N@C_{80}$ *on Cu(111)*, to be submitted

M. Treier, P. Ruffieux, R. Rieger, K. Müllen, S. Neppl, P. Feulner, C. Pignedoli, R. Fasel, *Surface-supported cyclodehydrogenation of a nanographene molecule*, in preparation

M. Treier, R. Fasel, *A refined method for background subtraction in X-ray photoelectron diffraction*, in preparation

Acknowledgements

I would like to thank Prof. Jürg Osterwalder for agreeing to be the director of this thesis. While our interactions may have been less frequent than with other PhD-students he has always shown a lot of genuine interest in this work during our discussion meetings which I found very reassuring and encouraging.

Special thanks go to Dr. Roman Fasel who was a great supervisor during the whole time. I have profited a lot from his motivating approach to science and his neverending source of ideas. Thanks a lot also for giving me the opportunity “to do what I want” during the past few years.

Prof. Thomas Greber and Prof. Neville V. Richardson have agreed to act as experts for this thesis for which I am very grateful. The collaboration with both of them during projects that are part of this thesis has been a great pleasure. Thomas’ enthusiasm during (one of) the endofullerene beamtimes was truly inspiring. I wouldn’t have been able to complete the work on the polyimides in such a short time without Neville’s help in both preparing the manuscripts and sharing his extensive knowledge on polymer chemistry.

During the first two synchrotron beamtimes I profited a lot from the help of Richard Schillinger. The (mostly) successful beamtimes would not have been possible without an always impeccably working beamline. I would like to thank Frithjof Nolting and his team at the SIM beamline for assuring that we always had perfect external conditions for our work.

I would also like to thank the chemists who provided the molecules for the various projects. Ralph Rieger and Xinliang Feng from Klaus Müllen’s group in Mainz provided several substances, which were in some cases even synthesized on request. Shengxiong Xiao and Colin Nuckolls made the studies on the nonplanar PAHs possible by providing two molecules of astonishing purity. Stephen Argent and Neil R. Champness have synthesized substances which brought us closer to an ordered polyimide network.

The support of detailed theoretical calculations was needed for the successful completion of several projects. Kriztian Palotas and Werner Hofer run DFT calculations on the step adsorption of HBC which helped in the understanding of the STM data. Manh-Thuong Nguyen did an excellent job in running numerous calculations for the hydrogen bonded PTCDA systems. Thanks also go to Daniele Passerone and Carlo Pignedoli for various computational work.

I would like to thank all the people in the nanotech@surfaces group in Thun for the great working environment. Thanks go to Pierangelo Gröning for sharing some of his vast knowledge on photoelectron spectroscopy, Pascal Ruffieux for numerous helpful discussions and for teaching me how to properly do STM of molecules. If a quick recapitulation of a solid state physics topic was needed, Oliver Gröning was always very helpful. My time in Thun would have been much more boring without my office colleague Ruben. Thanks for showing a lot of interest in all kind of non-science-related activities and for not killing me over the numerous jokes about chemists I made. I would also like to thank the other members of the group Ana, Roland, Kamel, Wende, Marco and Gilles for various discussions (be it on science or completely different subjects) and help here and there in the lab over all these years.

A huge ‘thank you’ goes to my parents who have been a great support during all my years of studies and who have been an enormous help in their role as grandparents during the final stages of my thesis.

The biggest thank you goes to Kristina. Thanks a lot for being there all these years and understanding (most of the time) that I spent so much time in the lab and an even bigger ‘thank you’ for giving me David (the greatest gift ever) and for taking almost all the ‘night-shifts’ while I was writing up my thesis.